ABSTRACT

DUBOSE, FRANKLIN H. Development of Two Components for the Neutron Electric Dipole Moment Experiment. (Under the direction of Dr. P. Huffman).

A new search for the electric dipole moment of the neutron has been proposed that will be housed at the Spallation Neutron Source at Oak Ridge National Laboratory [1]. The nEDM experiment is part of a class of new experiments aimed at searching for physics beyond the Standard Model, particularly in the CP and T violating sectors. Several proposed extensions to the Standard Model predict values for the electric dipole moment of the neutron. Thus, the discovery of a nonzero electric dipole moment for the neutron (nEDM) would have a fundamental impact upon the current understanding of the weak and strong nuclear interactions.

The nEDM measurement takes place in liquid helium, doped with trace amounts of polarized ^{3}He that functions as both a detector of neutron spin alignment and as a comagnetometer. When a neutron captures on ^{3}He, the decay products ionize the surrounding ^{4}He atoms, resulting in the production of excited singlet and triplet helium states along the ion path. When these excited states relax, light is produced in the extreme ultraviolet, which is then detected. The character of this scintillation light depends on the mass and energy of the ionizing particle. We are therefore characterizing this scintillation light for use as a method of discriminating neutron capture from backgrounds.

After the ^{3}He depolarizes, it is necessary to remove it before adding more polarized ^{3}He. It has been proposed that the depolarized atoms be removed using differential evaporation. We have developed a test evaporative purification apparatus that can facilitate this removal, therby lowering the concentration of ^{3}He in ^{4}He from approximately 10^{-10} to 10^{-12}. The operating temperature for the experiment, 350 mK to 500 mK, places a constraint upon the effectiveness of this technique. It is therefore necessary to design and optimize an apparatus capable of performing the above mentioned purfication in a time much less than the nEDM measurement time of approximately 22 minutes. Additional experimental concerns involve minimizing the introduction of heat to the system, effectively removing the evaporated gas from the testing area, and testing of evaporator performance.

Development of Two Components for the Neutron Electric Dipole Moment Experiment

by
Franklin H. DuBose

A dissertation submitted to the Graduate Faculty of
North Carolina State University
in partial fullfillment of the
requirements for the Degree of
Doctor of Philosophy

Physics

Raleigh, North Carolina

2009

APPROVED BY:

Dr. J. Rowe	Dr. W. Alexander
Dr. C. Gould	Dr. D. Haase

Dr. P. Huffman
Chair of Advisory Committee

DEDICATION

For those who always believed...

BIOGRAPHY

Franklin Henderson DuBose was born in Atlanta, Georgia. He attended Morehouse College in Atlanta, Georgia, where he graduated with a Bachelor of Science in Mathematics. He also earned a Master of Science degree in Physics from Clark Atlanta University. Franklin entered the Physics Ph.D. program at North Carolina State University in 2002.

During his early college career, Franklin met his best friend, then Eboni Fennell. She became his wife in August 2005.

ACKNOWLEDGMENTS

I would like to thank my advisor, Dr. Paul Huffman, and Dr. David Haase, whom I consider a co-advisor, for providing direction and inspiration for my research. I would also like to thank them for the patience and understanding they have granted me during my research. I would also like to give thanks to Dr. Jack Rowe, Dr. Chris Gould, and Dr. Winser Alexander, for agreeing to be part of my dissertation committee, and for their continued support and knowledge that they have given to me along the way. Thank you Tim Harvell, Chris Hewett, Frank Milkowski, and Robert Lynn Smith of the Instrumentation Shop for all the work you do and for never hesitating to lend a hand. Thanks also go to the numerous friends and colleagues I have met during my entire collegiate experience.

Last but not least, I would like to thank those individuals who have supported and influenced me along the way, namely my wife, Eboni DuBose. I would like to thank her especially for her patience. I would also like to thank my mother, Margie DuBose, for her support and belief. Finally, I would like to thank my daughter, Jacquelyn DuBose, who gives me a new reason to smile every day.

TABLE OF CONTENTS

LIST OF TABLES ..... **vi**

LIST OF FIGURES ..... **vii**

1 Introduction **1**
1.1 Motivation for the nEDM Search 1
1.2 Previous Experiments 5

2 Two Components for the nEDM Experiment **9**

3 Temperature dependence of n–^{3}He induced scintillations in ^{4}He **18**
3.1 Physics of Liquid Helium Scintillation 20
3.2 Overview of the HMI Particle Identification Experiment 24
3.3 Experimental Setup 24
3.4 Data Collection and Analysis 28
3.5 Results and Discussion 29
3.6 Conclusions 44

4 Evaporative Purification of Liquid ^{4}He for the nEDM Experiment **46**
4.1 Properties of ^{3}He/^{4}He Solutions 48
4.2 Removal of ^{3}He from ^{4}He through Differential Evaporation 52
4.3 Adsorption/Desorption Kinetics of Gas on Charcoal 65
4.4 Analysis of ^{3}He/^{4}He Ratios 68
4.5 Setup of the cryostat for the testing of evaporative purification 79
4.6 Gas Handling System 90
4.7 Heat Loads 92
4.8 Discussion 99

5 Summary of Results **100**
5.1 Particle Identification 100
5.2 Evaporative Purification 101

Bibliography **103**

LIST OF TABLES

Table 3.1 Temperature dependent background count rates 33

Table 3.2 Coincidence neutron capture count rates at each neutron fluence..... 36

Table 3.3 2-dimensional Gaussian fit parameters for the neutron capture peaks 37

Table 3.4 3-dimensional Gaussian fit parameters for neutron capture contour plots.... 42

Table 4.1 Mass 3 and 4 contaminants..... 69

Table 4.2 ^{4}He leak rates for the four tested ^{4}He calibrated leaks 70

Table 4.3 Mass 2, 3, and 4 leak rates for the four ^{4}He calibrated leaks 71

Table 4.4 Stainless steel thermal conductivity fit coefficients 77

Table 4.5 Conductance for each dilution refrigerator mounted thermometer 90

LIST OF FIGURES

Figure 1.1 Improvements in nEDM measurement sensitivity 6

Figure 2.1 Producion of ultracoldcold neutrons in liquid helium 12

Figure 2.2 Superfluid/Normal fluid composition of helium below the λ point 14

Figure 2.3 Detection of neutron capture on ^{3}He 16

Figure 3.1 Energy deposition in liquid helium by ionizing radiation 19

Figure 3.2 Temperature dependence of α–particle induced scintillations in ^{4}He 20

Figure 3.3 Layout of the neutron beamline at HMI 25

Figure 3.4 Light collection setup at HMI 26

Figure 3.5 Sample oscilloscope trace, resulting from neutron capture on ^{3}He 27

Figure 3.6 Comparison of signal backgrounds with neutron capture at 1.5 K 27

Figure 3.7 Empty cell background counts 31

Figure 3.8 Full beam background counts at 92 mK 32

Figure 3.9 Temperature dependent background pulse height spectra 32

Figure 3.10 Scaling of neutron capture peak height with beam flux 34

Figure 3.11 Isolation of the neutron capture peak using voltage discrimination 35

Figure 3.12 Neutron capture and background pulse height spectra 37

Figure 3.13 Sample full and small beam traces 39

Figure 3.14 Correlation of afterpulsing with pulse area (natural helium) 40

Figure 3.15 Correlation of afterpulsing with pulse area (blocked beam) 41

Figure 3.16 Contour plot correlating singlet pulse area with triplet decay pulses 41

Figure 3.17 Afterpulsing temperature dependence 43

Figure 3.18 Full and small beam afterpulse counts at $\sim$ 300 mK 44

Figure 4.1 Layout of the nEDM ^{3}He injection and removal system 47

Figure 4.2 ^{3}He and ^{4}He phase diagrams 48

Figure 4.3 The latent heat of vaporization of ^{4}He as a function of temperature 50

Figure 4.4 Temperature dependence of the ^{4}He vapor pressure below 1.25 K 51

Figure 4.5 ^{3}He vapor pressure as a function of temperature 53

Figure 4.6 ^{3}He/^{4}He evaporative purifier schematic 55

Figure 4.7 Plot of ^{3}He and ^{4}He vapor pressures below 600 mK 56

Figure 4.8 Ratio of the vapor pressures ^{3}He:^{4}He 57

Figure 4.9 Background pressure during evaporator operation 58

Figure 4.10 Molar removal rate of ^{3}He during a purification run cycle 59

Figure 4.11 Moles of ^{4}He removed during one purification cycle 60

Figure 4.12 Time required for one purification cycle 61

Figure 4.13 Number of purification cycles between charcoal regenerations 61

Figure 4.14 Critical velocity of superfluid ^{4}He film flow as a function of film thickness . 63

Figure 4.15 Activated charcoal ^{4}He capacity vs. ambient pressure 64

Figure 4.16 Temperature dependent adsorption of ^{3}He and ^{4}He on activated charcoal . 66

Figure 4.17 Leak rate, calculated for four ^{4}He calibrated leaks 71

Figure 4.18 Leybold L200 leak detector mass sweeps of four ^{4}He calibrated leaks 72

Figure 4.19 Gas handling system for real time analysis of desorbing gas composition .. 74

Figure 4.20 RGA100 ^{3}He pressure response with $P_{^4He} \sim 10^{-5}$Torr 76

Figure 4.21 Change in effective liquid helium trap volume due to boiloff 78

Figure 4.22 Partial pressure of ^{3}He as a function of input moles 79

Figure 4.23 Schematic of the SHE DRI–430 ^{3}He–^{4}He dilution refrigerator 81

Figure 4.24 SHE DRI-400 ^{3}He molar flow rate vs. pump inlet pressure 82

Figure 4.25 Gas handling system for the SHE Model DRI–430 dilution refrigerator 83

Figure 4.26 Cooling power curves for the SHE Model DRI–430 dilution refrigerator ... 84

Figure 4.27 Loss rate of liquid helium during refrigerator operation 87

Figure 4.28 Platinum resistor temperature calibration curve..... 88

Figure 4.29 Lakeshore model 16557 Ge resistor temperature calibration curve..... 88

Figure 4.30 GE RC model 7441 Ge resistor temperature calibration curve..... 89

Figure 4.31 Dale thermometer temperature vs. resistance curves 89

Figure 4.32 Gas handling system for the evaporator fill..... 91

Figure 4.33 Diagram of the evaporator supports..... 93

Figure 4.34 Heat loads from the evaporator to the dilution refrigerator 95

Chapter 1

Introduction

A new search for the electric dipole moment of the neutron has been proposed that will be housed at the Spallation Neutron Source at Oak Ridge National Laboratory [1]. The nEDM experiment is part of a class of new experiments aimed at searching for physics beyond the Standard Model, particularly in the CP and T violating sectors. Several proposed extensions to the Standard Model predict values for the electric dipole moment of the neutron. From the results of the nEDM experiment, several of these theories could either be confirmed, or ruled out [2, 3].

The proposed sensitivity of this experiment is $\sim 10^{-28}$e·cm. To achieve this, numerous stages of research and development, from calculations and tests which guide material selection, to the design and testing of cryogenic systems are required. Much of this research and development is dedicated to control signal backgrounds to the level necessary to perform such a sensitive measurement. Central to the nEDM experiment is ^{3}He, which serves the dual function of co-magnetometer, reflecting any magnetic field inconsistencies, and as an indicator of neutron spin alignment. This work provides an overview of the nEDM experiment and details the progress of two components of the research and development: signal processing for background reduction and the handling and removal of ^{3}He.

1.1 Motivation for the nEDM Search

The Standard Model provides a framework for the properties and interactions of the fundamental particles [4]. These fundamental particles can be grouped as quarks or

leptons, and interact through the strong, weak and electromagnetic forces.

Quarks can be grouped into one of six categories, termed flavors: up, down, top, bottom, strange, and charm. These particles, which make up the neutron as well as the other hadrons, have the properties of color charge, electric charge, mass, and spin. Of the fundamental particles, only quarks experience the strong force. Interactions via the strong force are mediated by gluons.

Leptons, which do not experience the strong force, also have six flavors, comprised of three particles and their respective neutrinos. These are the electron (e^-), electron neutrino (ν_e), muon (μ^-), muon neutrino (ν_μ), tauon (τ^-), and tauon neutrino (ν_τ). Lepton interactions involving the weak force are mediated by $W^\pm$ and Z^0 bosons. Both quarks and leptons experience the electromagnetic force. Interactions of particles via the electromagnetic force are mediated by photons.

Central to the development of the Standard Model is symmetry, as it relates to the transformations of charge conjugation (C), parity (P), and time reversal (T). Charge conjugation effectively changes a particle to its own antiparticle. Under a parity transformation, the spatial coordinates of a system are reversed. Thus, when the parity operator $\mathbf{P}$ acts on a system,

$$\mathbf{P}\Psi(\vec{r}) = \Psi(-\vec{r}) \tag{1.1}$$

where Ψ is the wave function for the system. The time reversal transformation acts similarly on the time coordinate. These transformations can also define symmetries when used together, as in CP and CPT. Our use of the Standard Model in understanding the nature of the universe is derived from both the conservation, and breaking, of these fundamental symmetries.

Parity violation has been measured in several systems. The earliest observation was in the β decay of polarized ^{60}Co, which showed an asymmetric spatial distribution of decay products with respect to the direction of the nuclear spin [5]. This violation is well represented in the Standard Model through the chiral coupling of fermions to gauge bosons [4]. CP violation was later observed in the decay of the neutral kaon system [6].

CP violation in the Standard Model can be seen in the quark – quark interaction via the weak force [7]. In this reaction, a quark can change flavor, resulting in a net change in its electrical charge. Thus, an up quark, for instance, with charge $\frac{2}{3}e$ can become a down quark, with electrical charge -$\frac{1}{3}e$, where e is the fundamental electric charge. The charge

current resulting from this e^- change is defined as

$$J^\mu = (\bar{u}\ \bar{c}\ \bar{t})\frac{\gamma_\mu(1-\gamma^5)}{2}U\begin{pmatrix} d \\ s \\ b \end{pmatrix}$$

with the matrix U given by

$$U = \begin{pmatrix} V_{ud} & V_{us} & V_{ub} \\ V_{cd} & V_{cs} & V_{cb} \\ V_{td} & V_{ts} & V_{tb} \end{pmatrix}$$

where $\gamma_\mu = \{\gamma^0, -\gamma^1, -\gamma^2, -\gamma^3\}$ are the gamma matrices and $\gamma^5 = i\gamma^0\gamma^1\gamma^2\gamma^3$ [8]. The 3×3 matrix U is known as the Cabibbo–Kobayashi–Maskawa matrix (CKM) [9]. The CKM matrix defines the probability that an up, top, or charm quarks will become a down, bottom, or strange quark through the weak interaction.

In the Standard Model, the CKM matrix contains four independent parameters. These are the three mixing angles in the quark field space and a complex phase $mboxe^{i\delta_{CKM}}$. It is this complex phase that can account for CP violation in the weak interaction [10].

CP violation in the Standard Model also appears in the effective Quantum Chromodynamics (QCD) Lagrangian, written as

$$L_{\text{eff}} = L_{QCD} + L_\theta$$

with

$$L_{QCD} = -\frac{1}{4}G^\alpha_{\mu\nu}G^{\alpha\mu\nu} - \Sigma_n\Psi_n\left[\delta - igA^\alpha t^\alpha + m_n\right] \tag{1.2}$$

$$L_\theta = \theta\frac{g^2}{32\pi^2}G^{\alpha\mu\nu}\tilde{G}^\alpha_{\mu\nu} \tag{1.3}$$

where $G^\alpha_{\mu\nu}$ is the color gauge-covariant gluonic field strength tensor, g is the strong coupling constant, A^α is the color gauge vector potential, and t^α is the set of generators of color [11, 12, 13]. The terms G and $\tilde{G}$ are related by $\tilde{G}^\alpha_{\mu\nu} = \frac{1}{2}\epsilon_{\mu\nu\rho\sigma}G^{\alpha\rho\sigma}$ where $\epsilon_{\mu\nu\rho\sigma} = -\epsilon^{\mu\nu\rho\sigma}$ is the total asymmetric tensor. Thus, for a nonvanishing θ, the QCD Lagrangian contains an explicit violation of CP.

The existence of possible further CP violation motivates the search for nonzero electric dipole moments. Asymmetry in CP can be observed in the case of spin 1/2 particles

subject to an electric field. The energy of such a particle is given by

$$E_p = d_p \vec{\sigma} \cdot \vec{E}$$

where d_p is the particle dipole moment, $\vec{\sigma}$ is its Pauli spin matrix, and $\vec{E}$ is the electric field. This relationship is odd under a CP transformation. The CPT theorem states that field theories with local, Lorentz invariant, hermitian Langrangians must be invariant under a combined C, P, and T transformation [14, 15]. Thus, an observed CP asymmetry also implies T violation.

The QCD model does not contain any predictions for the value of θ. It must therefore be determined experimentally by measuring certain physical quantities, such as particle dipole moments, which can then be applied to models that predict values of θ. Calculations have shown that $d_n \sim O(10^{-16})\theta$ where the current experimental limit on the neutron is $d_n \leq 2.9\times10^{-26}$ e·cm [16, 7, 17]. This corresponds to a value of $\theta < 10^{-9\pm1}$ [18]. The so-called "Strong CP problem" refers to the small experimental limits imposed on θ, as compared with $\theta \sim O(1)$, implied by equation 1.2.

Measurement of an electric dipole moment for the neutron in particular can provide direct insight into the θ term in the QCD Lagrangian. This stems from the G and $\tilde{G}$ terms, which couple to quarks, but do not induce flavor change [13]. Thus, the θ term is more sensitive to d_n than δ_{CKM}. This sensitivity does not exist for kaons and electrons. Therefore, measurement of a dipole moment for the neutron can be used to determine the value of a fundamental parameter of the Standard Model.

Another motivation to search for electric dipole moments is the desire to understand the source of CP violation beyond the scope of the Standard Model. Evidence of this unexplained violation can be found in the existence of the universe itself. In its beginnings, the universe was made of equal parts of both matter and antimatter. Mutual annihilation should have left a universe filled with only photons. Since this is not the case, there must be some mechanism, such as CP violation, that led to a matter dominated universe.

The number of photons in the cosmic background is evidence of matter–antimatter annihilation in the past. Measurements of the cosmic background are used to quantify this observed asymmetry, written as

$$\frac{n_B - n_{\bar{B}}}{n_B + n_{\bar{B}}}$$

where n_B and $n_{\bar{B}}$ are the number of baryons and antibaryons respectively. A comparison of estimates of the present number of baryons with the cosmic background gives a few baryons for every 10^{10} photons [19, 20]. This observation calls into question how physical processes could have caused an asymmetry to develop.

A possible explanation for the baryon asymmetry of the universe (BAU) was given in the work of Sakharov, where he outlined conditions necessary for an inequality in baryon/antibaryon number to develop. He stated that reactions which lead to the preferential population of baryons must 1) change the number of baryons (B-violating) 2) violate CP, and 3) occur in non-equilibrium processes [21]. B-violating processes have not been observed experimentally, though they are no longer considered forbidden in the Standard Model [22]. While CP violation has been observed, the CP violation seen in the Standard Model is many orders of magnitude less than what would be required to explain the observed baryon asymmetry [23].

The purpose of the nEDM experiment is to either search for a new source of CP violation or set tigther constraints on CP violation within the Standard Model.

1.2 Previous Experiments

Many theories exist, both within and outside the framework of the Standard Model, that attempt to explain the experimentally observed CP violation. Using these theories, one also predicts a range of values for the electric dipole moment of the neutron. With improving experimental methods, many of these models have been successfully ruled out. The progress of these experiments is shown in Figure 1.1, alongside some representative theoretical models.

Until roughly 1950, parity conservation was assumed to be a fundamental symmetry. However, this assumption was not backed up by experiment, which led Purcell and Ramsey [24] to develop an experimental test. Their aim was to measure the dipole moment of a neutron, as a neutron dipole moment is forbidden under parity symmetry. Neutrons were chosen because they are electrically neutral and could therefore traverse a large electric field without being accelerated out of the measurement region [25].

In their experiment, a beam of neutrons passed through an electric field region between two oscillatory magnetic fields. Any change in the magnetic resonance frequency

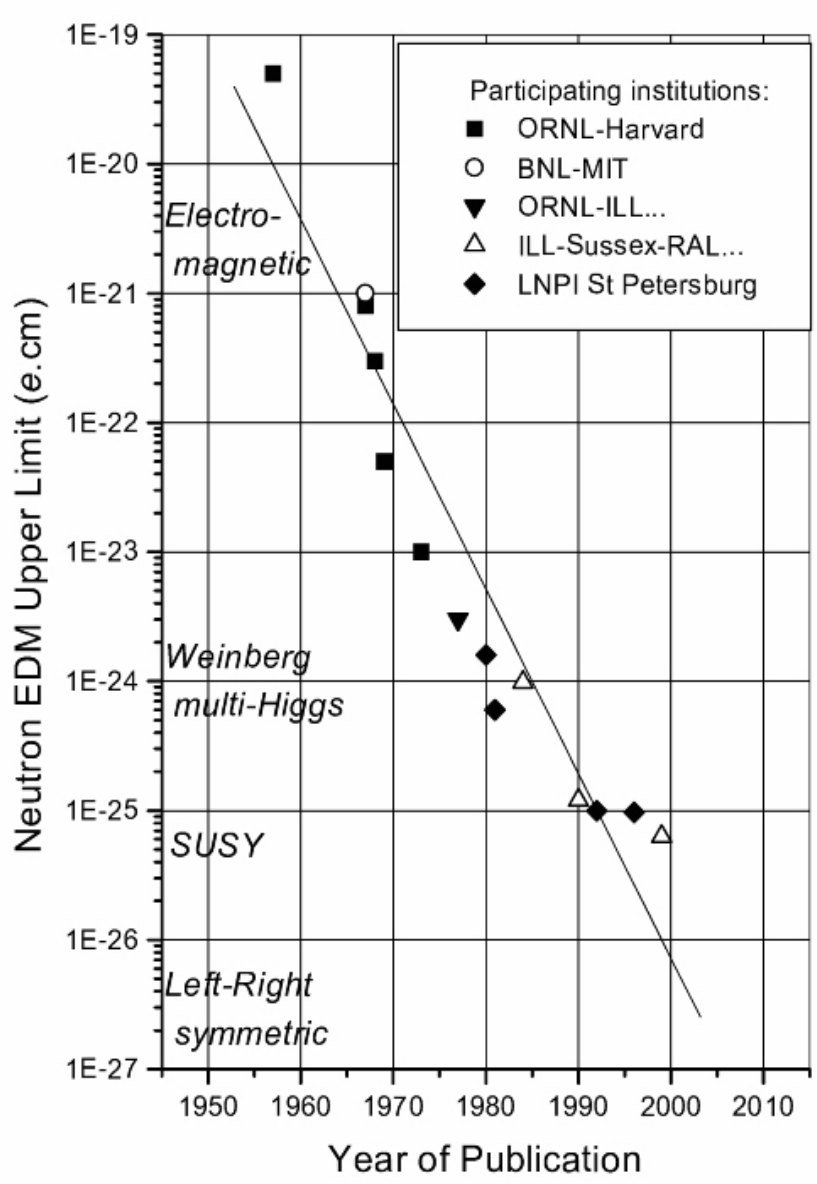

Figure 1.1: Improvement in the experimental upper limit on the neutron Electric Dipole Moment as a function of time [1]. Given on the y–axis are a few of the models that are being tested or have been ruled out by neutron electric dipole moment experiments. The proposed 10^{-28}e·cm sensitivity of the nEDM experiment will allow testing of the limits on d_n proposed by the Supersymmetry and Left–Right Symmetric models.

of the neutrons could be attributed to a neutron electric dipole moment. The experiment detected no neutron electric dipole moment, to a level of 5×10^{-20} e·cm.

Because parity violation had not been observed in any system up to this point, the assumption of parity conservation was seen as a sufficient argument against the existence of an electric dipole moment for the neutron. However, near the time of the Purcell and Ramsey experiment, parity violation in the weak interaction was proposed to explain anomalies in the decay of the K meson, and measured in the β decay of ^{60}Co [5, 26]. This observation was sufficient to eliminate parity conservation as an argument against the existence of a neutron electric dipole moment.

Under a symmetric CP or T tranformation, dipole moments of the fundamental particles are forbidden [27, 28]. Thus, the final symmetry argument against the existence of a neutron electric dipole moment was disproved with the observation of CP violation in the decay of the K^0_L meson.

Several models were developed to explain the observed CP violation in the K^0_L meson. These theories also predicted values for the neutron electric dipole moment. This renewed interest in the search for violations in the CP sector. As a result, several experiments using the beam resonance technique were developed to measure the neutron electric dipole moment.

The most sensitive of these experiments was performed by Dress *et al.* [29]. In this beam experiment, neutrons were passed through a 17 G magnetic field region, also containing a 100 kV/cm electric field. The neutrons were polarized and analyzed by magnetized iron mirrors, also located within the field region. Once polarized, oscillatory fields were used to change the orientation of the neutron spins [30]. The effects of changing the electric field orientation with respect to the magnetic field could then be measured as a change in the neutron resonance frequency. The results of this experiment served to lower the experimental upper limit to $(4\pm15)\times10^{-20}$ e·cm.

In these beam-type experiments, the neutron velocities averaged between 80 and 180 m/s. Inherent in beam magnetic resonance experiments is uncertainty about the effective magnetic field due to the neutron velocity. The shift caused by this effective field:

$$\Delta B = \vec{v} \times \frac{\vec{E}}{c^2}$$

set an upper limit on the uncertainty of beam experiments. Experiments to measure the neu-

tron electric dipole moment therefore shifted to the use of slower neutrons. In these experiments, electric dipole measurements were made using ultracold neutrons ($v < 8$ m/s) that were stored in bottles via total internal reflection from the walls due to the Fermi potential.

The next generation of experiments were all stored ultracold neutron (UCN) experiments. In addition to reducing the velocity effects seen in beam studies, magnetic resonance experiments using stored neutrons gave a much narrower resonance peak ($\sim$0.01 Hz) than the approximately 80 Hz width peak seen in beam experiments [28, 31, 32, 33, 34, 35]. In the early bottle experiments, neutrons were stored in an electric/magnetic field region for 5 – 80 s [28, 36, 37]. Using adiabatic fast passage nuclear magnetic resonance, the neutron resonance was measured, subject to an electric field applied parallel or antiparallel to the magnetic field. The lowest measurement limit published from these early experiments is $(0.3\pm4.8)\times10^{-25}$ e·cm [37].

These early experiments were limited by ultracold neutron density and an inability to assess magnetic field inconsistencies. The problem of uncertainty due to low ultracold neutron density was addressed through improvements in moderator technology, as well as the introduction of neutron reflecting turbines, which remove one component of the neutron's velocity [38]. The larger uncertainty arises from changes in the magnetic field when the electric field is reversed. Concerns over the limits imposed by variations in the constant magnetic field led to the introduction of a co-magnetometer, present in the neutron experimental volume, to directly measure the field.

Baker *et al.* published the most recent experimental limit of the neutron electric dipole moment in 2006, using an atomic mercury co-magnetometer [39]. A direct measurement of the magnetic moments of the mercury atoms as they precessed in the magnetic field region, was used to sample the magnetic field experienced by the neutrons. This sampling had to be scaled due to the different gyromagnetic ratios of neutrons and mercury, where $\gamma_n/\gamma_{Hg} = -3.842$. This group set an experimental upper limit of $d_n \leq 2.9\times10^{-26}$ e·cm. The principal uncertainty in this experiment is the geometric phase effect. This shift in the Larmor precession frequency due to the random motion of spins in an applied electric field can mimic a dipole moment. An extensive discussion of this effect as it relates to trapped neutrons is given in Pendlebury's 2004 paper [40] and by Golub and Lamoreaux [41]. Current neutron electric dipole moment experiments have reached sensitivities where this effect must be accounted for and/or minimized.

Chapter 2

Two Components of the nEDM Experiment

This chapter provides an overview of two components of the research and development for the nEDM experiment. The first is an identification of neutron capture events and the second is the removal of depolarized ^{3}He from the target cell.

In the nEDM experiment, magnetic resonance will be used to make an electric dipole moment measurement of stored, polarized ultracold neutrons. Ultracold neutrons, which have a known magnetic moment $\vec{\mu_n}$, are placed in a uniform magnetic field $\vec{B_0}$. The spins of these neutrons are then rotated into the plane perpendicular to the magnetic field, generating a torque on the neutrons defined by $\tau = \vec{\mu} \times \vec{B}$. This torque causes the particles to precess in the plane perpendicular to the magnetic field. For the neutron, a spin 1/2 particle, the frequency of the precession is $\nu_n = -2\mu_n B_0/\hbar$. A similar precession frequency exists for a spin 1/2 particle possessing an electric dipole moment $\vec{d}$ subject to a static electric field E_0, given by $\nu = -2dE_0/\hbar$. Thus, the Hamiltonian of a neutron in an external parallel magnetic and electric field region is given by

$$H = -(\vec{\mu_n} \cdot \vec{B_0} + \vec{d_n} \cdot \vec{E_0})$$

giving a precession frequency of

$$\nu = -(2\mu_n B_0 + 2d_n E_0)/\hbar$$

where d_n is the neutron electric dipole moment.

A deviation from the magnetic field induced neutron precession frequency can be attributed to d_n–E_0 interactions. This is quantified by applying the electric field both parallel and antiparallel to the magnetic field. In the antiparallel configuration, the neutron precession frequency is given by

$$\nu = -(2\mu_n B_0 - 2d_n E_0)/\hbar$$

giving a net difference in precession frequency of $\Delta\nu = 4d_n E_0/\hbar$. For the neutron, this frequency shift is potentially on the order of μHz. For a known electric field E_0, this frequency shift corresponds to an electric dipole moment uncertainty of

$$\delta d_n = \hbar \frac{\delta \Delta \nu_n}{4E_0} \tag{2.1}$$

where $\delta\Delta\nu_n$ is the uncertainty in precession frequency shift. For a $d_n \approx 10^{-27}$e·cm, $\delta\Delta\nu_n$ should be $\sim \mu$Hz. In order to achieve this precision, the magnetic field should be measured with a co-magnetometer, which samples the same volume as the neutrons. The nEDM experiment collaboration has chosen to use polarized ^{3}He as this co-magnetometer, since it disolves in liquid ^{4}He and has a magnetic resonance frequency near that of the neutron. The ^{3}He atoms in the measurement cells precess subject only to the external magnetic field. This is due to Schiff shielding, in which the two ^{3}He electrons effectively cancel any electric field effects [42]. Because the EDM is thus several orders of magnitude smaller for ^{3}He, as well as its large diffusion coefficient($\sim$730 cm^2/s), the ^{3}He atoms can be used to uniformly sample the magnetic field. At sufficient densities, the magnetic moments of these atoms can be detected using superconducting quantum interference devices (SQUID), allowing an in situ measurement of the magnetic field. The use of co-magnetometers has been a common feature of stored neutron EDM experiments, beginning with the work of Ramsey, who introduced the use of mercury of this purpose [25].

The applied electric field has a design strength of 50 kV/cm, with a 1% uniformity over the cell volume and a $< 1\%$ shift over the measurement cycle. The magnetic field strength will be $\sim$10 mG.

The nEDM experiment will use neutrons produced by bombarding liquid mercury with a high energy ($\sim$1 GeV) proton beam [43, 44]. H_2 and H_2O are used as moderators, creating a source of cold and thermal neutrons respectively. Since 8.9 Å neutrons are the primary component needed for the superthermal production of ultracold neutrons (see

Figure 2.1), these neutrons are Bragg reflected out of the beam and directed into the apparatus using alkali-intercalated graphite monochromators. A polarizing supermirror is then used to select for a particular spin state. Experimentally, this supermirror technique has been shown to produce greater than 95 % polarization [18].

In order to maximize the counting statistics, ultracold neutrons will be produced directly in the measurement cells. This is done using a momentum transfer process known as the superthermal process, first proposed by Golub and Pendlebury [45, 46]. In this method, 8.9 Å neutrons enter the liquid within the acrylic cells with momentum $\omega = \hbar^2 k^2/2m$. This momentum expression defines the dispersion curve for the neutron in the liquid, shown as the parabolic curve in Figure 2.1. When plotted against the dispersion curve for excitations in He–II, the curves cross in the linear region of the superfluid curve, at $2\pi/\mathrm{k}^* = 8.9$Å, corresponding to an energy $\mathrm{E}^* = (\hbar k^*)^2/2m \sim 12$ K. Neutrons with wavelengths at or near 8.9Å and momentum $\hbar k_i$, upon crossing the acrylic cell boundary and encountering the superfluid region, lose nearly all momentum and downscatter into the ultracold regime, with energies of <100 neV.

Conservation of energy and momentum, i.e.

$$\hbar Q = \hbar k_i - \hbar k_f \tag{2.2}$$

$$\frac{\hbar^2 k_i^2}{2m} = \frac{\hbar^2 k_f^2}{2m} + E(Q) \tag{2.3}$$

dictates that these now ultracold neutrons can only absorb phonons with energy $\mathrm{E}^* = 11$ K. The probability of the reverse process of neutron upscattering by phonon absorption is minimized by the 350 – 400 mK temperature of the superfluid. This is due to the low temperature suppression of the phonon density, which scales with the Boltzmann factor $e^{-\hbar\omega/T}$. Neutron production thus proceeds at a rate

$$P = 7.2 \frac{d^2\Phi}{d\lambda d\Omega \lambda_u^3} \delta\Omega \frac{\mathrm{n}}{\mathrm{cm}^3 \cdot \mathrm{s}} \tag{2.4}$$

where $\mathrm{d}\Phi/\mathrm{d}\lambda$ defines the neutron spectral density at 8.9 Å and λ_u^3 is the maximum neutron wavelength that the cell can trap. The tightly bound ^{4}He nucleus has a neutron absorption cross section of zero, resulting in no UCN loss to absorption on ^{4}He. Several experiments have been conducted to measure this production rate, with varying levels of agreement with theoretical UCN production rates [49, 50, 51, 52, 53, 54].

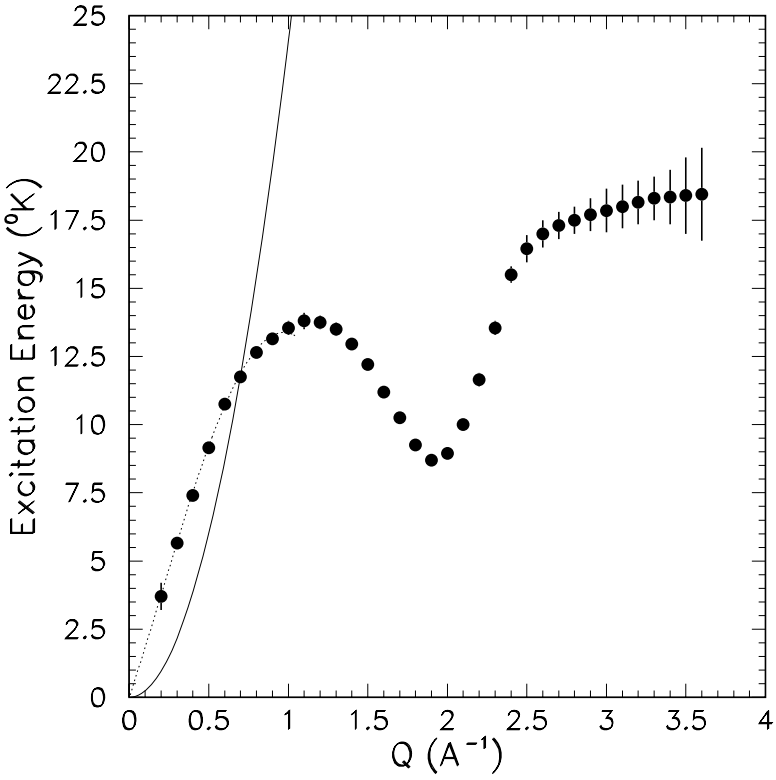

Figure 2.1: Single–phonon excitation energy (K^0) vs. momentum tranfer($\hbar Q$) for superfluid ^{4}He [47]. The solid curve is the energy vs momentum curve for neutrons. The dotted curve is a parametrization by Maris [48]

.

Once in the low energy state, the ultracold neutrons are trapped within the experimental cells, since they no longer have sufficient kinetic energy to overcome the material wall potentials. While the neutron beam is on, an ultracold neutron population then builds up within the liquid helium volume, subject to the loss constraints of the experiment. In the two nEDM measurement cells, these constraints are dominated by wall losses, neutron β decay, and neutron capture on ^{3}He. The UCN loss rate is thus defined as

$$\tau^{-1} = \tau_{wall}^{-1} + \tau_{\beta}^{-1} + \tau_{^3\mathrm{He}}^{-1} + \ldots \tag{2.5}$$

which limits the maximum UCN density.

The expected UCN production rate is $\sim$0.4 UCN/cm^3·s. Thus, given the 134 neV, defined by the deuterated polystyrene doped with deuterated tetraphenyl butadiene, the expected 500 s storage time should yield neutron densities of roughly 150 UCN/cm^3.

Once a sufficient population of UCN has been achieved in each of the cells, the neutron beam is turned off and polarized ^{3}He from an atomic beam source is introduced into the cells. These polarized atoms from the beam are incident upon a free liquid ^{4}He surface in the ^{3}He injection storage volume, and are transported into each of the measurement cells through either diffusion or the use of heat currents.

One of the central challenges of the nEDM experiment is the controlled movement of ^{3}He. After injecting polarized ^{3}He into the injection volume, it must be moved, in a polarity conserving process, into the measurement cells. This can be accomplished either through the passive diffusion process, or through an active heat flush. A primary restriction on using diffusion for transport in the nEDM experiment is the dependence of the diffusion rate on temperature. The planned operating temperature for the experiment is roughly 400 mK. Diffusion of ^{3}He in ^{4}He limits this technique to a maximum temperature of 300 mK. Secondly, while the diffusion process can proceed fairly quickly below 300 mK, there is some concern over the amount of depolarized ^{3}He atoms remaining in the injection volume that could diffuse into the cells in the next measurement cycle. For these reasons, it has been proposed that an active heat flush process be used to transport ^{3}He.

The heat flush method is an established technique for removing ^{3}He from ^{4}He, though at temperatures closer to 1.5 K. Developed by McClintock, the heat flush relies upon the dual nature of liquid helium below the lambda point [55]. Whereas liquid helium is termed a *superfluid* below the lambda point, it is actually composed of a mixture of

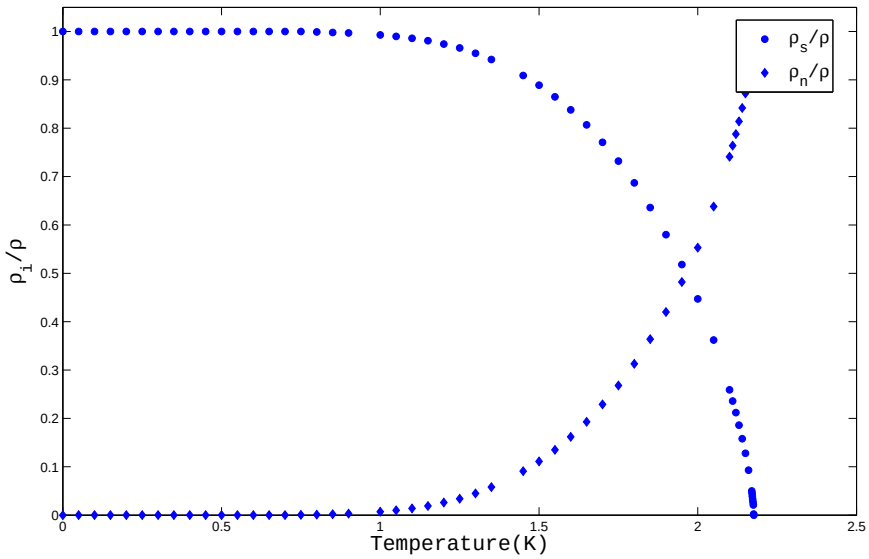

Figure 2.2: Relative normal fluid and superfluid composition of pure ^{4}He below the λ point (2.18 K). ρ_s and ρ_n indicate the superfluid and normal fluid densities respectively [56].

superfluid and normal fluid. The relative concentrations are temperature dependent, and are shown graphically in Figure 2.2. In the presence of localized heating, the superfluid moves toward the source, while the normal fluid component moves away from the source. Because in a solution the ^{3}He atoms interact with the normal fluid, a localized heat source can be used to drive these atoms toward colder areas [55]. This method has been very well characterized at temperatures $\sim$1.5 K, and it has been shown that diffusion of ^{3}He atoms against the direction of normal fluid movement is negligible. An extensive theoretical treatment has been given to extending the heat flush to operatate at temperatures below 0.5 K [57].

The viscosity of the normal fluid η_p is defined as the product of the normal fluid phonon density and the diffusion constant of the phonon gas. When a heat source is introduced, the ^{3}He atoms travel subject to the velocity, viscosity, and density of the surrounding normal fluid, while undergoing convection and diffusion. A model has been developed to describe this convective/diffusive motion and has determined the heat flush to be a viable mechanism for ^{3}He transport. Theoretically, this can be done while still maintaining over

90 % polarization [57].

The polarized ^{3}He atoms are flushed into the cells with their spins aligned with the neutrons. The spin vectors of both species are then rotated into the plane perpendicular to the magnetic field and electric field using a magnetic field pulse, applied at 3.165 Hz for 1.58 s. In order to conserve angular momentum, the neutrons and the ^{3}He atoms start to precess about B_0 at their respective Larmor precession frequencies. The ^{3}He Larmor precession frequency differs from the neutron precession frequency due to the difference in magnetic moments of the two species ($\mu_n/\mu_{^3He} \approx 0.9$).

When both species are polarized and brought into the field region, neutron capture proceeds as

$$\mathrm{n} + ^3\mathrm{He} \rightarrow \mathrm{p} + \mathrm{H}_3^+ + 784 \text{ keV}$$

which will occur when their spins are antiparallel. The recoil proton and triton from neutron capture on ^{3}He ionize the helium which produces extreme ultraviolet light ($\lambda_{EUV} \sim 80$ nm). The EUV light propagates undisturbed through the liquid [58], until it encounters the wavelength shifting coating on the inner walls of the acrylic cell, where it is converted to visible light ($\lambda \sim 430$ nm). The blue light is transported down a series of waveguides to photomultiplier tubes and detected. A diagram of the detection mechanism is shown in Figure 2.3.

The spin alignment requirement, coupled with the different precession frequencies of the two species, implies a periodicity to the neutron capture rate. In order to accurately measure electric field effects on the neutron precession frequency, it is necessary to accurately determine the rate of neutron capture. This is complicated by backgrounds arising as a result of the use of ^{4}He scintillation as an indicator of neutron capture.

Any ion with sufficient energy can produce scintillation in ^{4}He. This includes the products of neutron β decay

$$n \rightarrow p + e + \bar{\nu}_e + 782.6 \text{ keV}$$

which can potentially be a large source of backgrounds. In Chapter 3, I discuss my work in developing a method of distinguishing n–^{3}He capture light from scintillations induced by other radiation sources. The method was applied to data collected in an experiment in which neutrons were passed through a cell containing a mixture of ^{3}He and ^{4}He. The resulting scintillation light data contained background signals comparable to and greater

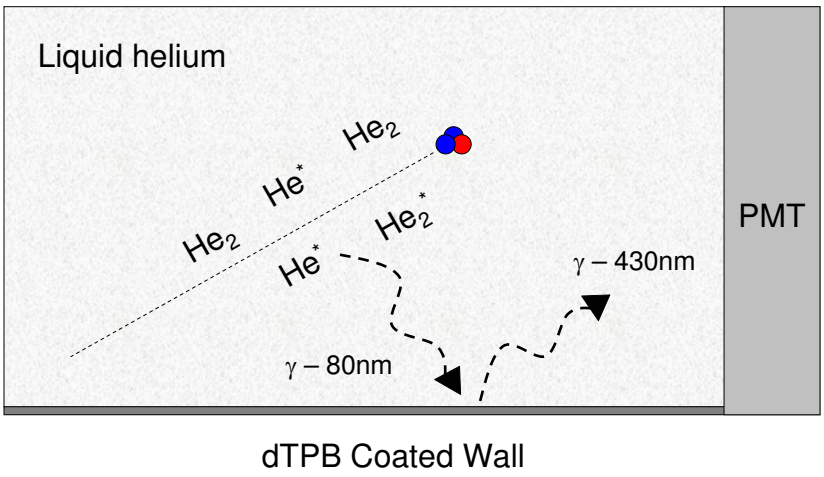

Figure 2.3: Detection of neutron capture on ^{3}He through liquid ^{4}He scintillation. The recoil triton and proton deposit energy in the surrounding ^{4}He atoms, producing excited states. When these excited states relax, they emit photons in the extreme ultraviolet. An organic fluor converts these EUV photons to blue light for detection.

than the neutron capture signal. The character of this light differs when the radiation source is a heavy ion, as compared with β or γ sources. This difference can be exploited to isolate light originating from neutron capture. Successfully categorizing the source of induced scintillations in such an experiment represents a crucial step towards a precision nEDM measurement.

Polarized ^{3}He depolarizes after some finite time, depending upon experimental conditions. Once the atoms depolarize, they can no longer be used for the electric dipole moment measurement or magnetic field assessment. Therefore, the depolarized atoms must be removed from the measurement cells. Removal requires a second heat flush to drive the depolarized atoms to an isolated volume. Once the measurement cell has been emptied of ^{3}He atoms, the removal of these atoms can proceed in parallel to data collection.

In the nEDM experiment, it has been proposed that an evaporative purifier be used to remove depolarized ^{3}He from the system [59]. Chapter 4 therefore covers progress towards the development of an apparatus to remove ^{3}He atoms from ^{4}He. To test the viability of evaporative purification, I have worked in the development of a prototype apparatus which

will be used to remove ^{3}He impurities from ^{4}He. The purification process is a distillation, using the differing vapor pressures of ^{3}He and ^{4}He to preferentially remove ^{3}He atoms. Discussed are specifics of apparatus design, performance, and testing. Also discussed are the issues involved in using this system in a sub–1 K experiment.

The goal of the nEDM experiment is to achieve at least a factor of 200 improvement in the sensitivity to a neutron EDM over previous experiments. The application of these two components will have a direct impact upon this desired result.

Chapter 3

Temperature dependence of n–^{3}He induced scintillations in ^{4}He

In the nEDM experiment, polarized ultracold neutrons (UCN) will be trapped in a volume containing superfluid ^{4}He, with a 10^{-10} concentration of polarized ^{3}He. The neutrons and ^{3}He atoms are subject to an applied magnetic field. The interaction of their magnetic moments with this field causes the species to precess about the field axis with slightly different frequencies in the liquid, due to the 10% difference in their gyromagnetic ratios.

Neutron capture on ^{3}He depends strongly on the relative spin alignment of the two species. When the spins are anti-parallel, the ^{3}He adsorption cross section σ_{abs} for ultracold neutrons is 2.4×10^6 barns, whereas $\sigma_{abs} \approx 0$ when the spins are aligned parallel [60, 61]. Thus, one obtains a time dependent capture rate as the species precess. This capture rate is the signal of interest in the nEDM experiment.

When a neutron captures on a ^{3}He atom in the reaction given by

$$\mathrm{n} + ^3\mathrm{He} \rightarrow \mathrm{p}^+ + \mathrm{H}_3^+ + 765 \text{ keV}$$

energy is deposited in the surrounding ^{4}He atoms by the recoil products, creating excited states in the helium. These excited states relax by emitting ultraviolet light. The time dependent rate of neutron capture on ^{3}He is measured by detecting this scintillation light.

A major source of background events are the products of neutron β-decay, given

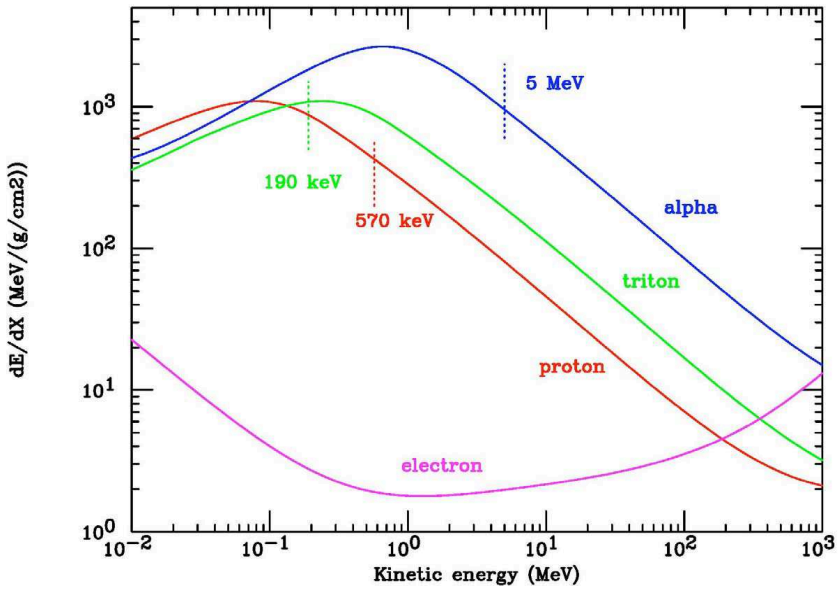

Figure 3.1: Energy deposited in liquid helium by ionizing radiation. The triton and proton are decay products of neutron capture on ^{3}He. Neutron β - decay yields a proton and electron. For completeness, α - particles are included, as they exhibit a known time dependence for scintillations induced in ^{4}He.

by

$$\mathrm{n} \rightarrow \mathrm{p}^+ + e^- + \bar{\nu_e} + 782 \text{ keV}$$

since the energy from the recoil electrons can also excite ^{4}He atoms. The scintillation light produced as a result of this decay is comparable in both size and rate to the neutron capture signal. Thus a means of discriminating neutron capture from β-decay events is desirable.

The energy deposited in ^{4}He from the decay products of neutron capture, neutron decay, and α–decay is shown in Figure 3.1. The energy loss per unit length of β-decay events is considerably longer than that for neutron capture. For a typical β-decay, the electron travels almost 1 cm, whereas for a neutron capture event, the heavier particles travel less than 1 mm. One would expect that the dynamics of the scintillation process will be different for the two types of events. I have therefore investigated a particle identification method to correlate scintillation light with the type of ionizing radiation.

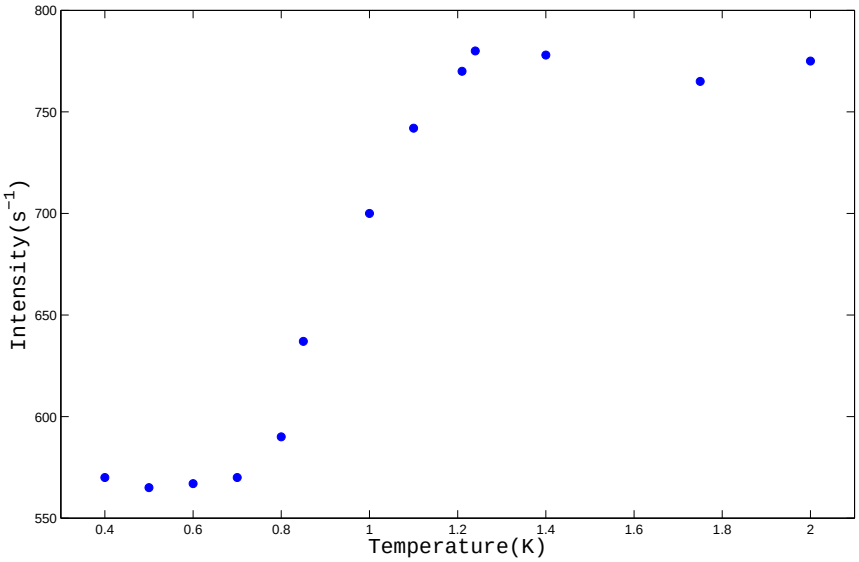

Figure 3.2: Temperature dependence of α–particle induced scintillations in ^{4}He. The scintillation intensity decreases sharply as the temperature is lowered from 1.2 K to 0.6 K, and becomes nearly constant at lower temperatures. This effect has been attributed to a the decrease in roton density that accompanies decreasing temperature [62].

The temperature dependence of scintillation induced by α–particles has been previously measured by Roberts and Hereford [62]. The results of that experiment are shown in Figure 3.2. From Figure 3.2, it is clear that the scintillation intensity when using an α-source decreases by roughly 25 % as the temperature is lowered from 1.2 K to 0.6 K. I am also quantifying the temperature dependence of the scintillations produced through neutron capture.

3.1 Physics of Liquid Helium Scintillation

When ionizing particles pass through liquid helium, they lose energy to the surrounding atoms. If the ionizing particles are of sufficient energy ($E > 42.3$ eV), they can singly ionize atoms in the liquid [63]. This leads to the production of excited atomic and molecular helium states along the ion path. The population rate and density of these excited states depends strongly upon the charge and mass of the ionizing particle. Thus, the energy

deposited per unit length, $\mathrm{d}E/\mathrm{d}x$, for an electron is different from that of an α particle, producing different excited state populations. The energy deposited per unit length for β particles is 50 eV/μm [64]. Therefore, the electron's journey through the liquid produces ionization events every 846 nm. On average, the 2.5×10^4 eV/μm energy deposition of α particles, however, produces ionization events roughly every 1.6 nm.

The ionized He^+ and e^- pairs have a separation of approximately 10 nm. Within 600 ps of ionization, the He^+ ions interact with the surrounding liquid, eventually forming He_3^+. It is believed that these charged molecules attract surrounding helium atoms, forming what is termed a *snowball*, with an effective mass of 40 times the mass of a ^{4}He atom, m_4 [65]. The free electrons repel the surrounding helium atoms, forming what is termed a *bubble*, with an effective mass of $\sim$240 m_4. Though the bubble forms within 4 ps, it moves slowly through the liquid due its large effective mass [66]. Thus, the He_3^+ snowball–e^- bubble recombination

$$He_3^+ + e^- \rightarrow He_2 + He$$

takes roughly 3 ns. The He_2 molecules are formed in both $He_2(A\,^1\Sigma_u^+)$ singlet and $He_2^*(a\,^3\Sigma_u^+)$ triplet states.

The population of singlet and triplet state molecules depends upon the type of ionizing radiation [67]. Because the ion–pair spacing arising from β particles is roughly 846 nm, compared to the 10 nm He^+-e^- spacing, there is a high probability that the ionized atom will recombine with its freed electron. This results in the singlet states being preferentially populated. The 1.6 nm ion–pair spacing produced by α sources, however, increases the likelihood of mixing among the He^+ ions and freed electrons, producing a relatively higher number of triplet state molecules; the observed triplet:singlet state ratio has been measured as 3:1 when using an α source.

Secondary contributors are singlet $He(2^1S)$ and triplet $He^*(2^3S)$ state metastable atoms, produced as helium atoms absorb energy from the ionizing radiation. The singlet:triplet state ratio of these is roughly 5:1 [68]. The singlet atoms interact with the liquid to form singlet molecules, though the lifetime of this reaction is not well understood. Triplet state atoms interact with atoms in the liquid to form triplet helium molecules. This reaction occurs with a lifetime of approximately 15 μs [69, 68, 70]. The decay of singlet state molecules occurs on a nanosecond timescale and is characterized by a large pulse of EUV light.

After the decay of the singlet state molecules, some singlet and triplet state atoms and triplet molecules remain. These molecules are responsible for smaller light pulses which we refer to as "afterpulses". This light emission can stem from either the decays or interactions of these excited states. The degree of interaction is driven by the density of excited states. Thus, different types of ionizing particle reactions can produce different afterpulsing characteristics.

Light emission from the afterpulses occurs with both α and β sources. Using a β source in 250 mK liquid helium, the afterpulsing rate has been show to decay exponentially with a 2 μs time constant [71, 70]. It is speculated that the source of this exponential decay rate is the interaction of helium singlet atoms with the surrounding liquid to form singlet state molecules, i.e.

$$\mathrm{He}(2^1S) + \mathrm{He} \rightarrow \mathrm{He}_2(A^1\Sigma_u^+)$$

which decay within a few nanoseconds[72]. Triplet state atoms can similarly interact with the surrounding atoms to form triplet molecules[73].

In addition to the exponentially decaying afterpulse rate, α sources have a longer lived component that varies inversely with time and also decreases in intensity with decreasing temperature. Possible sources of this component are the singlet atoms, triplet atoms, triplet molecules, helium ions, or electrons that remain after the fast singlet molecule decays. Given the ion density produced by α sources, as compared with that of β sources, it is most likely that the source of this tail is the interaction of metastable states. The high excitation densities produced by α particles make Penning ionization the most likely mechanism for tripet state destruction.

Penning ionization, i.e.

$$\mathrm{He}_2^* + \mathrm{He}_2^* \rightarrow 3\mathrm{He} + \mathrm{He}^+ + e^-$$

$$\mathrm{He}_2^* + \mathrm{He}_2^* \rightarrow 2\mathrm{He} + \mathrm{He}_2^+ + e^-$$

occurs with near unity probability when molecular collisions occur. Because this reaction requires no activation energy and occurs with a very high probability when molecular collisions occur, Penning ionization can greatly erode the number of triplet state molecules in experiments with high excitation energies. As the triplet molecules destructively interact, they produce singlet state atoms and molecules which can then radiatively decay, contributing to the afterpulsing rate.

The afterpulsing rate resulting from Penning ionization depends on the density of excited triplet state molecules. Initially, this distribution is defined by the path traced by the ionizing particles through the liquid. As an ionizing particle travels through the liquid, one can assume that it produces excitations that form a cylindrically symmetric Gaussian shape. As the excited singlet and triplet atoms and molecules interact and expand outward, they maintain the Gaussian shape. Because the resulting second generation singlet state atoms and molecules have a Gaussian distribution, the light produced can be modeled as

$$I'(t) = \frac{k_f k_{tt} T_s N_T(0)}{2\chi_{tt} t_{tt} \left[1 + \frac{t_d}{2t_{tt}} ln\left(1 + \frac{t}{t_d}\right)^2\right]^2 \left(1 + \frac{t}{t_d}\right)}$$

where k_{tt} is the triplet–triplet destruction lifetime, τ_s is the singlet decay lifetime, and t_d is the time constant for the decrease in triplet state density at the center of the ionization track, defined as $t_d = r_0/4D_T$; r_0 is the initial track radius [62]. The outward expansion of triplet state molecules away from the ionization track decreases the triplet state density, reducing the probability of Penning ionization occuring.

The rate of expansion along the ionization path depends on diffusion, which is itself temperature dependent. Because ionizing radiation can considerably raise the temperature of the liquid along the ionization track, the rate of diffusion depends more on the ion energy deposition than on the temperature of the surrounding liquid. As the temperature is increased, excitons along the ionization track diffuse more rapidly. Therefore, when helium is irradiated with α's, for example, the resulting excitons can be expected to expand away from the ionization track more rapidly than for electrons. This increased diffusion rate can decrease the probability of singlet production after the initial prompt pulse. This mechanism was initially proposed by Hereford and Roberts to explain the observed temperature dependence of the prompt pulse produced using α sources [62].

After the expansion immediately following ionization, the excitons thermalize with the surrounding liquid. The decrease in scintillation intensity with decreasing temperature observed when helium is ionized by α's can be explained using this rapid expansion model [70].

As the unreacted triplet molecules diffuse through the liquid, they exert a repulsive force on the surrounding helium atoms. One can therefore assume that the excited molecules behave in the liquid as they would in a vacuum. The radiative lifetime of $He_2^*(a^3\Sigma_u^+)$ in

vacuum has been calculated to be ∼18 s [74, 75]. The molecules are relatively stable in vacuum because a radiative decay to the ground state, i.e. two singlet state atoms, is a forbidden transition, requiring a spin flip. Therefore, if the molecules do not lose energy due to interaction with other excited species, or by colliding with the container walls, they can have a radiative lifetime of several seconds. Because Penning ionization occurs with such a high probability, this long lifetime decay has not been observed in a vacuum.

3.2 Overview of the HMI Particle Identification Experiment

To quantify the scintillation temperature dependence, and the effectiveness of the scintillation character as a means of background discrimination, an experiment was conducted whereby a cold neutron beam was passed through a cell containing a dilute ^{3}He/^{4}He solution. Two different ^{3}He concentrations were used to focus on either n–^{3}He capture or backgrounds. The neutron beam was also blocked in order to measure scintillations induced by Compton scattered γ's, originating from neutron interactions with collimators, filters, etc., along the beam path. The experiment was conducted over a range of temperatures below the λ point of ^{4}He. This was done to measure the effect of temperature on the intensity of triplet decays resulting from neutron capture, as well as to assess any temperature dependence in the measured backgrounds.

3.3 Experimental Setup

The experiment was performed at the 10 MW Berlin Experimental Reactor (BER–II) at the Hahn-Meitner Institut (HMI) in Berlin, Germany. Neutrons from the reactor core are moderated by water and an approximately 10 cm thick layer of cold hydrogen to yield a Maxwellian temperature distribution of ∼30 K. The cold neutrons leaving the source first travel through a series of neutron guides before entering a polarizer, which preferentially selects for one spin state, although polarization is not necessary for this experiment. The beam of polarized neutrons is then collimated using a lithium–loaded aperture. This emerging beam is nearly uniform in intensity across the diameter of the beam at the image plane downstream.

Although the source produces mostly cold neutrons, there can still be a signifi-

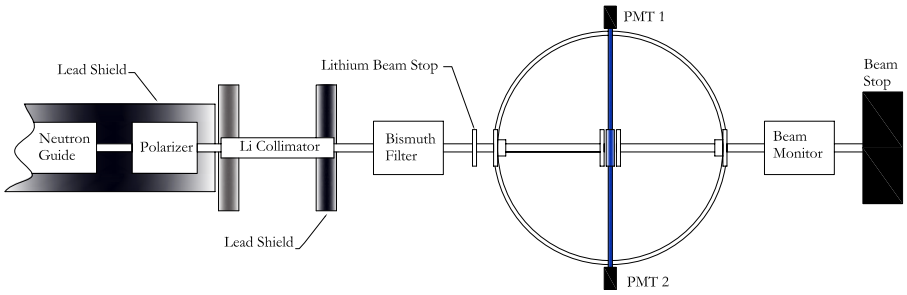

Figure 3.3: Layout of the neutron beam line for the pulse discrimination experiment at the Hahn-Meitner Institute. The ∼30 K neutrons were produced in the H_2 moderated cold source at the BER–II reactor. The neutron beam has a flux after the lithium collimator of 10^{-6}n/cm^2·s, and loses roughly 20% on transmission through the bismuth filter.

cant number of high energy neutrons and gamma rays created as a byproduct of fission in the reactor and neutron capture along the beamline. Thus, the beam line contains a bismuth filter, placed directly downstream of the collimator, to filter high energy neutrons and gamma rays. The initial neutron beam flux was approximately 10^6 n/cm^2·s, with a cross section of 1 cm^2 before the bismuth filter (see Figure 3.3). We estimated the flux of neutrons entering the cell based on a calculated 80% transmission for cold neutrons with wavelengths > 6.5 Å through a 77 K bismuth filter [76]. To vary the neutron flux to the measurement cell, the lithium–loaded beam stop was partially or completely removed. With the lithium–loaded beam stop removed, the flux to the cell was $\sim 0.8 \times 10^6$n/cm^2·s. A second beam stop, placed beyond the measurement cell, absorbed neutrons that were not captured.

The measurement cell was an acrylic cylinder with a total liquid capacity of 334.5 cm^3. The inner walls of the cell were coated with a layer of deuterated polystyrene doped with deuterated tetraphenyl butadiene (dTPB-dPS). Before coating, the cylinder barrel and one flat end surface were glued together using Stycast 1266. The liquid dTPB-dTS mixture was then brought into the partial assembly, then allowed to run out, creating a transparent coating on the inner surfaces. After similarly coating the remaining disk, all of the components were annealed. The cylinder assembly was completed using Stycast 1266. This coating served to convert the ultraviolet scintillation light to blue light for transmission down the light guides.

The neutron beam passed through the cell perpendicular to the cylinder axis. Scintillation light was measured using two photomultiplier tubes (PMT), positioned 180° apart and perpendicular to the beam direction, as shown in Figure 3.4. The photomultiplier tubes were at room temperature, and each was located approximately 30 cm from the end of the cell, and 40 cm from the neutron beam. These PMTs were operated in pulse counting

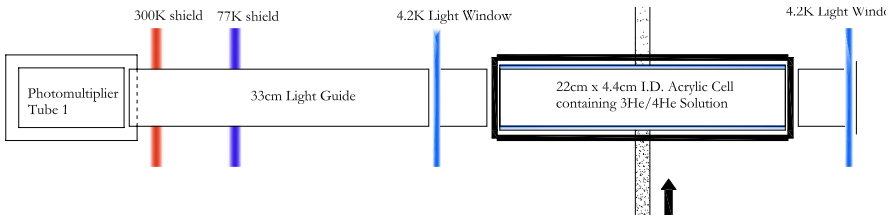

Figure 3.4: Acrylic cell and light collection layout for the pulse discrimination experiment at the Hahn-Meitner Institute. Measurements were made primarily with the cell containing a dilute solution of ^{3}He/^{4}He, with varying ^{3}He concentrations. Two photomultiplier tubes (one shown), facing the ends of the cylindrical cell, allowed both coincidence and non-concidence measurements.

mode at a voltage of between 1.75 kV and 1.9 kV. The operating voltage was varied in order to account for any gain differences in the two PMTs. An additional gain factor, determined from the PMT outputs, was introduced as needed in the data analysis software.

The PMT output was read using a LeCroy oscilloscope, with a maximum time resolution of 125 ps/point. For the data collection runs used to determine the neutron capture count rate, data was recorded without coincidence in 10 ms intervals, with a time scale resolution of 1 or 10 ns/point. Data used for triplet pulse counting was taken in coincidence, with an afterpulse counting window of 20 μs, at a timescale resolution of 1 ns/point. After each run, the oscilloscope trace was saved to disk, with each trace file containing information about the hardware settings. A typical trace contained large voltage spikes, indicative of singlet decay, followed by a series of smaller after pulses. There are also pulses, with a height comparable to the after pulses, that follow a singlet trigger. These pulses are attributed to ringing in the photomultiplier tube signal. A sample trace is shown in Figure 3.5.

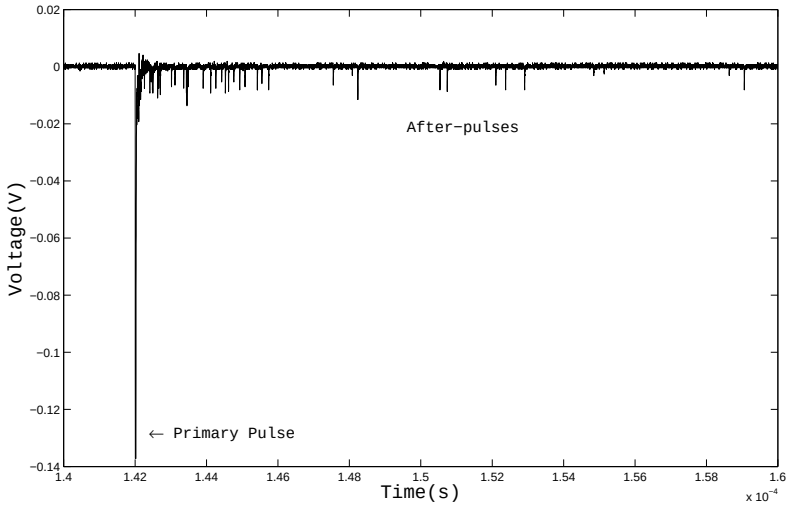

Figure 3.5: Sample photomultiplier tube output, resulting from the neutron beam incident on a 90 mK ^{3}He/^{4}He solution with a ^{3}He concentration $\sim 10^{-5}$. The large "Primary Pulse" is indicative of singlet decays, with the triplet decay "Afterpulses" shown following the roughly 1.5 μs of PMT ringing.

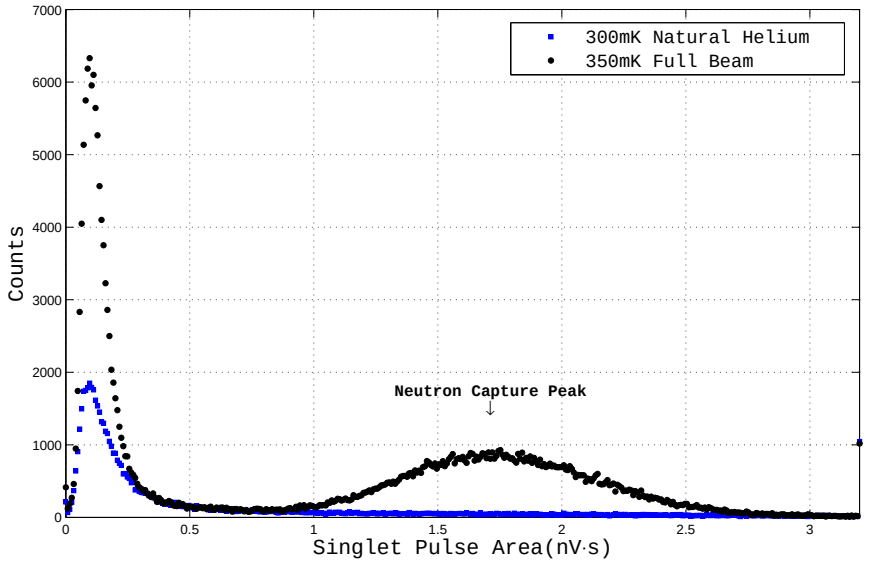

Figure 3.6: Comparison of signal backgrounds with neutron capture at $\sim$ 300 mK. The backgound curve results from neutrons incident on a cell containing natural helium ($x_3 \sim 10^{-7}$). After increasing the ^{3}He concentration to $\sim 10^{-5}$, neutron capture occurs

3.4 Data Collection and Analysis

Data was taken without neutron capture in two ways. The first was through the use of liquefied natural helium with a ^{3}He concentration $\approx 10^{-7}$. With natural helium in the cell, the neutron capture rate was low enough that this could serve to quantify the background rates. By increasing the ^{3}He concentration to 1.5×10^{-5}, one can begin to see neutron capture. From the comparison of data collected at the two ^{3}He concentrations shown in Figure 3.6, it is apparent that the additional ^{3}He allows one to see the neutron capture events, producing a clearly defined peak, centered $\sim$1.6 nV·s.

Data was taken in both non-coincidence and coincidence modes. For measurements taken without coincidence, the PMT's were read independently and all data was recorded. Events from the resulting traces could then be examined for each individual PMT, or combined using a coincidence algorithm in the processing software. From the non-coincidence data, we were able to compile information on event counts, pulse heights, and integrated pulse areas. Analysis of non-coincidence traces was used to 1) quantify neutron flux at the various beam sizes, 2) determine individual PMT backgrounds, 3) observe any temperature dependence in the pulse area distribution, 4) observe any temperature dependence in the pulse height distribution, and 5) quantify the neutron capture count rates.

The aim of using coincidence is to filter out background events not originating in the cell and single photoelectron events in the cell. Single photonelectrons can often result from luminescence, induced as neutrons interact with the materials surrounding the helium [77]. For a double PMT setup, the rate of single (non-coincident) photons can be estimated by

$$R_s = 2\tau R_1 R_2 \tag{3.1}$$

where R_s is the rate of single photons detected, R_1 and R_2 are the trigger rates of each PMT, and τ is the discrimination binwidth, set by the electronics of the data acquisition system [68].

For coincidence analysis, a 15 mV lower discrimination level and a 20 ns coincidence window were set in the software. After an event trigger, identified as the primary singlet pulse, afterpulsing events were recorded for 8 μs. Counting was started 1.5 μs after the initial trigger to account for any PMT ringing effects from the primary pulse. This separation of measured pulses into two event classes allowed for a direct correlation of after-pulsing with

temperature and beam flux. With these software settings, we were able to 1) characterize the time and temperature dependence of after-pulsing for neutron capture on ^{3}He, 2) quantify after-pulsing for background events, 3) correlate the number of afterpulses with the primary pulse area, and 4) distinguish neutron capture scintillations from those induced by Compton scattered γ's.

Data was taken with the measurement cell empty, containing natural abundance helium (natural helium runs), and containing ^{4}He with a ^{3}He concentration of 1.5×10^{-5} (doped ^{3}He runs). In each case, exclusive of the empty cell, data was collected with and without (blocked beam runs) neutrons passing through the cell. The beam intensity was varied using collimators with three different geometries, denoted as full beam, small beam, and ultra small beam, corresponding to respective decreases in beam intensity. Data was collected over a range of temperatures from 90 mK to 1.9 K. A summary of the 16 days of collected data is given below.

1. Empty cell
2. Natural helium filled cell,
   - Full Beam: 90 mK, 300 mK, 700 mK, and 1400 mK
   - Blocked Beam: 90 mK, 300 mK, 700 mK, and 1400 mK
3. ^{3}He added, bringing the concentration to 1.5×10^{-5}
   - Blocked beam: 90 mK, 300 mK, 500 mK, 630 mK, and 1500 mK
   - Full Beam: 90 mK, 300 mK, 500 mK, 630 mK, and 1500 mK
   - Small beam: 90 mK, 122 mK, 300 mK, 500 mK, 1500 mK, 1900 mK
   - Ultra small beam: 90 mK, 1500 mK, 1900 mK

3.5 Results and Discussion

The data sets listed above were analyzed offline. Each digitized pulse was recorded using identical voltage thresholds. The result of this procedure was a set of data files for each run that contained triggered voltages with the corresponding event times. These data

files were then read into the software package Igor Pro 6.0.3.1 which was used for further analysis.

The events in each data files were binned to construct histograms of pulse height and area, given in volts and V·s respectively. The measured voltages and areas are proportional to the energy deposited in the liquid. Data analysis was performed on the summed, binned data. This method of producing pulse area spectra can allow clear discrimination of the one, two and sometimes higher photoelectron peaks. The energy deposition sensitivity of the experiment was equally sensitive with respect to pulse height and pulse area. This analysis focuses on pulse area distributions.

Characterization of Background Counts

It is important to first understand what backgrounds are present. Specifically, one must determine how the backgrounds vary with temperature and thresholds, and what means can be taken to suppress them. The purpose of the background analysis was to quantify any temperature dependence in the background count rates.

Background events are observed to contain a time dependent component, arising from short lived activation of materials for neutron capture and neutron induced luminescence of materials, and a time-independent component, for long lived activation from either the neutrons or naturally occuring and prompt gammas from the reactor and neighboring experiments. These time dependent sources can be grouped as 1) radiation originating from the source, along the beam path, and from the materials making up the apparatus, 2) neutron–acrylic cell interactions, and 3) neutron–^{4}He induced luminescence. The constant background can originate either in the experimental apparatus or from outside due to shielding imperfections.

In the processing of non-coincidence background data, the analyzed events were limited to areas within a given area range by setting low and high voltage discrimination limits. By varying the voltage discrimination levels, we can separate the largely single photoelectron background events from the neutron capture signal.

Backgrounds were first studied by passing the neutron beam through an empty cell with a low discrimination level of less than 2 mV. The resulting data was used to produce a histogram of pulse areas, shown in Figure 3.7. The single photon peak was found to occur

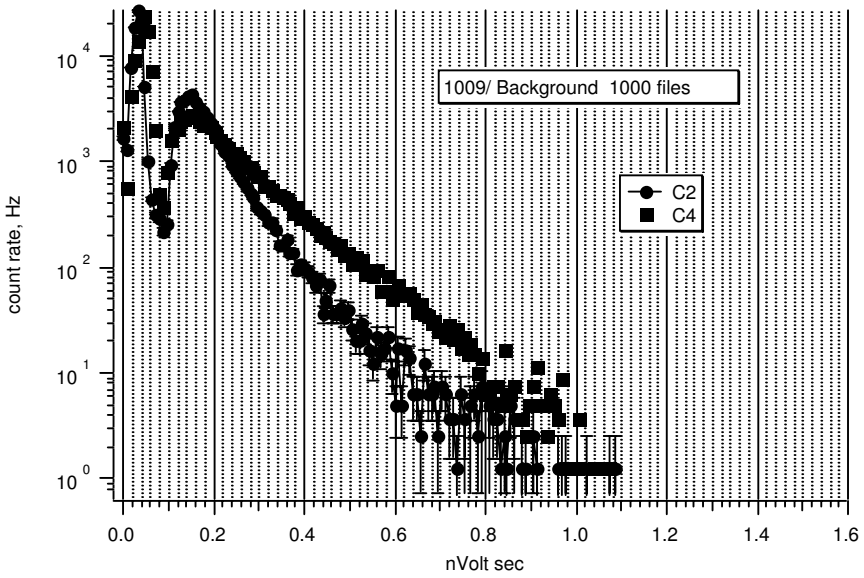

Figure 3.7: First experimental run using neutrons incident on an empty cell. The PMT voltage was set at 2 kV and a timescale resolution of 1 ns/point was used. The single photoelectron peak (SP) can be seen corresponding to an area of approximately ∼0.15 nV·s.

at ~ 0.15 nV·s.

The counts shown in Figure 3.7 are raw data, taken without collimation and with no bismuth filter in place. In order to distinguish scintillation photons from radiation resulting from the acrylic cell and light guides, a series of changes were made to optimize data collection. This optimization involved the improvements in collimation, the addition of a bismuth filter, and additional shielding on the apparatus.

We next analyzed the background count rates with natural helium in the cell. Here, the neutron capture rate on ^{3}He is small enough that it does not contribute to the overall signal. Data was collected with the incident beam both blocked by the lithium–loaded beam stop and with the neutron beam passing through the measurement cell. Data was taken at 90, 300, and 1400 mK.

Data for each PMT was first analyzed individually. From the comparison of data from each PMT at 92 mK, and with the cell containing natural helium, shown in 3.8a it

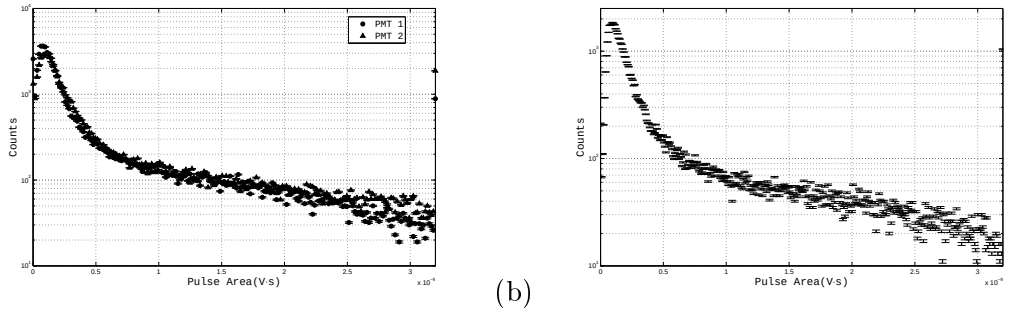

(a) (b)

Figure 3.8: Histogram of pulse areas, in V·s, resulting from a neutron beam traversing a 92 mK cell containing natural helium a) without coincidence b) with software coincidence. The PMT counts give a measure of backgrounds arising from neutron induced ^{4}He luminescence, neutron–cell interactions and γ's produced along the beam path.

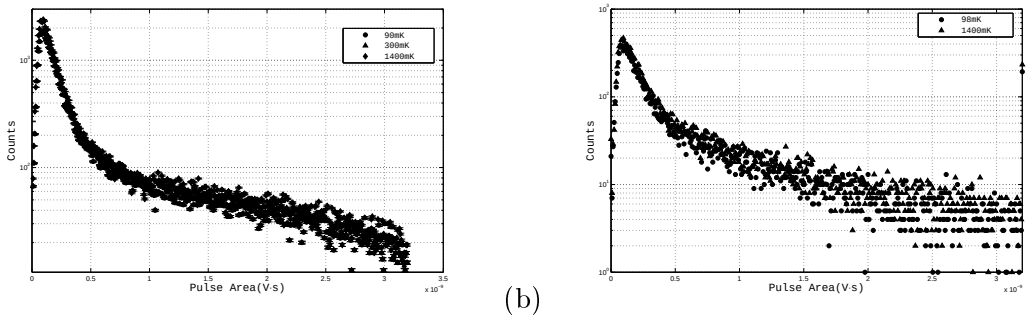

(a) (b)

Figure 3.9: Temperature dependent pulse height spectra for a) collimated beam on cell containing natural helium b) blocked beam, cell containing natural helium

can be concluded that both PMT's are recording nearly the same number of counts. This is confirmed in 3.8b, which shows the same data, analyzed with coincidence using a 20 ns software coincidence window.[1] One can see that the majority of counts are coincidence events, with backgrounds dominated by events having a pulse area of less than 0.4 nV·s.

A second set of background data was collected with the lithium-loaded beam stop in place. In this way, the neutrons were blocked, but gammas were not. This was done both with the cell containing natural helium and with the ^{3}He concentration increased to 1.5×10^{-5}. A comparison of the pulse height spectra with and without neutrons is shown

[1]Based upon the geometry of the light collection system, a 15 ns delay is introduced before checking for a coincidence peak.

^{3}He concentration	Temperature (mK)	Full (counts/s)	Blocked (counts/s)
Natural Helium	92	7352 ± 30.32	1667.3 ± 14.45
	300	7350.2 ± 30.31	–
	1400	8761.7 ± 33.09	1991.3 ± 15.78
Doped Natural Helium	90	–	1955±22.11
	300	–	1923 ± 21.93
	500	–	1874 ± 21.64
	650	–	1833 ± 21.41
	1500	–	1721 ± 20.74

Table 3.1: Background count rates, in counts/second. The resulting count rates were calculated after a software introduced coincidence.

in Figure 3.9. With neutrons, the overall counts are roughly 4 times higher than without. The count rates were determined by integrating over the range of pulse areas and dividing by the total data collection time.

The resulting count rates with x_3 $\sim 10^{-7}$ and x_3 $\sim 10^{-5}$ are summarized in Table 3.1. It is clear from Table 3.1 that the full beam background count rates with the cell containing natural helium are roughly four times higher than the natural helium count rates measured with only gammas entering the cell. In addition, at 1400 mK the count rates were roughly 20 % higher than at 98 mK. This was true for both the full and blocked beam natural helium data. With x_3 $\sim 10^{-5}$, the opposite was true, with the count rates decreasing with increasing temperature.

It is concluded that, both with the beam blocked, and with neutrons passing through natural helium, the pulse height spectra exhibit a temperature dependence. The initial aim was to verify constant background levels over the temperature range under study. The observed temperature dependence requires one to group each neutron capture data set with a corresponding background run taken at the same temperature. Because there was not a one–to–one correspondence, certain background rates were estimated, based upon observed trends.

Neutron Capture

By raising the ^{3}He concentration to 1.5×10^{-5}, the ratio of neutron capture events

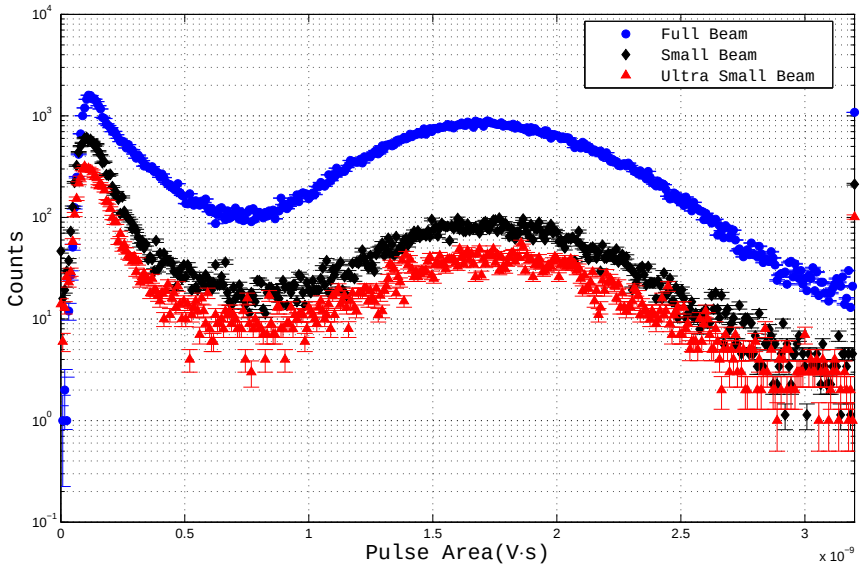

Figure 3.10: Histogram of pulse areas for full, small, and ultra small neutron beams incident on cell containing ^{4}He with a 1.5×10^{-5} ^{3}He concentration. Run times are normalized to 4 seconds

to background events is increased. With the measurement cell containing 15 ppm ^{3}He, data was collected between 90 and 1900 mK, at full, small, and ultra small beam intensities, corresponding to a particular neutron flux. Pulse height spectra taken under these conditions at 90 mK are shown in Figure 3.10. One can easily see the reduction in neutron flux from these figures. One can also see a distinct difference in these data as compared to the data shown in Figure 3.8. The peak centered around 1.6 nV·s corresponds to neutron capture on ^{3}He. From Figure 3.10, it is also clear that this peak does not change in position with decreasing beam current.

In each of the background plots shown so far, what appears as a peak is an effect of the voltage discrimination level, introduced in the software. A lower discrimination level of 2 mV removes events with an area less than ~ 0.1 nV·s. Thus, the neutron capture peak was first isolated by raising the lower discrimination level in the analysis software. The initial hardware limit was set to 2 mV. By raising the software limit to ∼12 mV, corresponding to a pulse area of ∼0.5 nV·s, one can eliminate most of these events. The cuts were applied to both the neutron capture and background data, as shown in Figure 3.11.

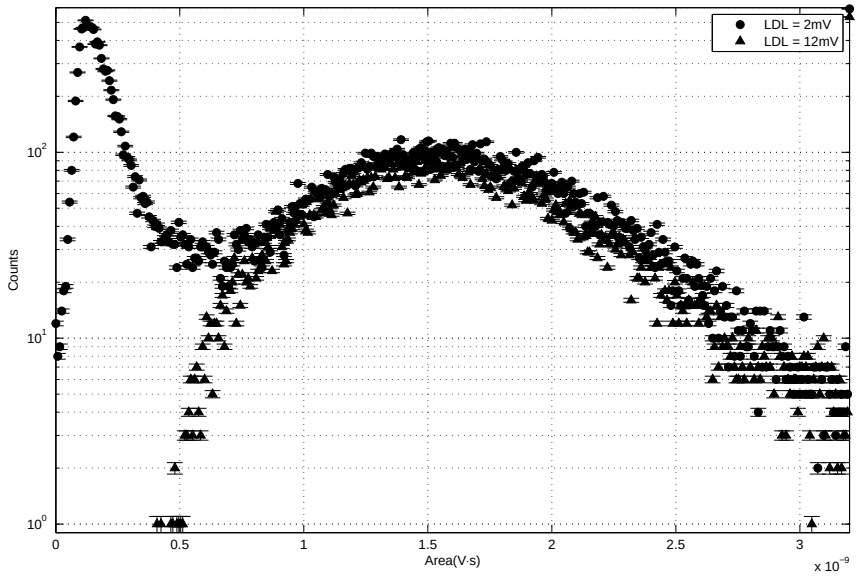

Figure 3.11: Removal of events from the neutron capture and background pulse height spectra by increasing the lower discrimination level (LDL). By raising the LDL to 12 mV, events with an area of less than 0.5 nV·s are removed.

Temperature (mK)	Full Beam	Small Beam	Ultra Small Beam
85	–	2815.72±18.67	–
90	$1.52\times10^4\pm61.64$	–	2926±27.05
350	$1.38\times10^4\pm58.74$	3043.5±39.01	–
500	$1.31\times10^4\pm57.23$	1311.2±11.45	–
630	$9.95\times10^3\pm49.87$	–	–
1500	$9.28\times10^3\pm48.17$	3490±132.1	1396±7.47
1900	–	3440±131.15	1463±8.55

Table 3.2: Coincidence neutron capture count rates, in counts/second, in the full, small, and ultra small beam configurations. For each run, the count rates were calculated by integrating the voltage isolated neutron capture peak over the total data collection time.

The neutron capture rate was first determined without background subtraction. This was done by integrating the histogram of pulse areas from 0.8 to 3.2 nV·s and dividing by the total data collection time. Results of this integration at the maximum neutron flux are shown in Table 3.2. The configuration used for collection of natural helium data is designated as Setup 1. Setup 2 was used for all neutron capture data collection. The full beam counts without background subtraction show a consistent decrease in neutron capture with increasing temperature. The small beam count rates differ from the full beam counts by a factor of ~ 4. In general, the count rates are consistent at 90 and 300 mK, increasing for T$\geq$1500 mK. The exceptions are at 122 and 500 mK. Data was taken at these temperatures after a change in the experimental setup. Therefore, the lower observed count rates can be attributed to the apparatus. The ultra small beam count rates were roughly 1/10 of those observed at with the largest collimator.

Next, the normalized natural helium data is subtracted from the neutron capture data. The resulting peak is shown in Figure 3.12. One can see that, even without background subtraction, the ^{3}He capture events can be identified with greater than 90 % probability just by using cuts on the pulse area between 1.0 and 3.0 nV·s.

Each subtracted data set is fit to a gaussian of the form $y = y_0 + A\exp(x - x_0/\sigma)^2$. The resulting fit parameters at the full neutron intensity are given in Table 3.3. The full beam peak pulse area shows agreement to within 99 % for all temperatures. Roughly 90 % agreement is seen at the smaller beam fluxes. The variation in the small and ultra small beam fit data is likely due to a higher uncertainty in their respective background counts,

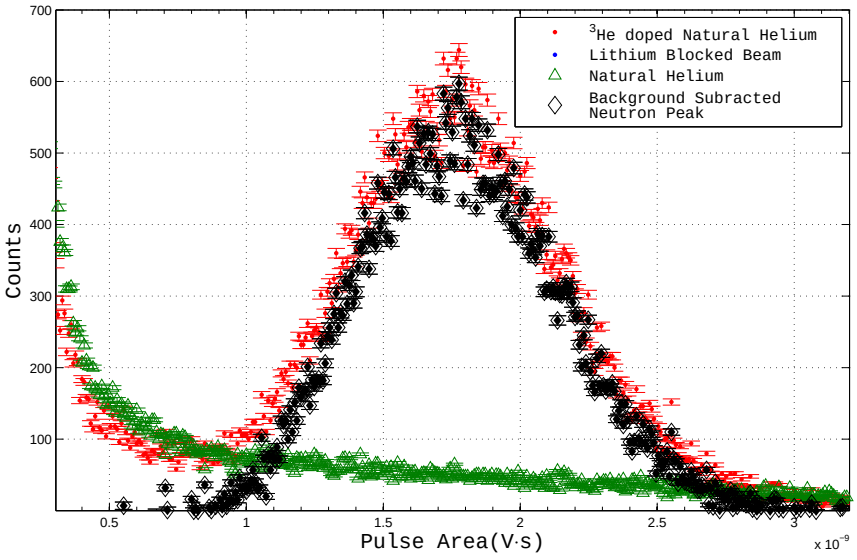

Figure 3.12: Comparison of counts for the full beam on a cell containing natural helium and 15 ppm ^{3}He/^{4}He. The background subtracted neutron peak is fit to a gaussian function.

Beam size	Temperature (mK)	y_0	A	$x_0(\times 10^{-9})$	$\sigma(\times 10^{-10})$
Full Beam	90 Setup 1	-22.78±2.57	822.96±4.48	1.74±0.002	5.47±0.04
	90 Setup 2	-23.66±3.39	937.78±5.86	1.78±0.003	5.51±0.05
	350	3.63±2.47	838.65±4.45	1.7608±0.002	5.30±0.04
	500	3.20±2.36	787.71±4.28	1.757±.002	5.27±0.04
	630	-26.99±2.93	600.73±5.13	1.7723±0.004	5.44±0.06
	500	-28.42±.15	561.01±5.53	1.7806±0.004	5.44±0.07
Small Beam	85	4.8341±0.41	73.22±0.775	1.73±.004	5.067±0.07
	90	-0.381±0.538	79.595±0.963	1.76±0.05	5.33±0.08
	300	-1.0±0.67	80.18±1.13	1.757±.006	5.61±0.11
	500	-8.9449±.069	30.43±1.15	1.62±0.02	5.65±0.29
	1500	-17.14±2.94	117.22±6.96	1.56±0.02	4.01±0.3
	1900	-16.68±2.70	120.3±6.73	1.54±0.02	3.76±0.26
USB	90	4.8341±0.41	73.22±0.775	1.73±0.004	5.067±0.07
	1500	-30.46±3.42	36.07±4.07	2.0±0.06	8.11±1.25
	1900	-30.85±3.21	39.04±3.89	1.99±0.005	7.93±1.08

Table 3.3: 2-dimensional Gaussian fit parameters for the neutron capture peaks. Data was taken without coincidence.

which were estimated based on a scaling of the full beam background counts.

Triplet State Decay Analysis

Up to this point, I have focused on the prompt singlet pulse. The main difference in scintillation light produced by neutron capture on ^{3}He and that produced by background events is the triplet afterpulse signature. Due to the dynamics of ionization, β-decay or Compton scattered electrons will have a different ratio of the number of triplet state afterpulses relative to the area of the prompt singlet pulse. We therefore investigated the scintillation light produced in liquid helium that is ionized by both protons and tritons from neutron capture and electrons. The afterpulsing is known to have a time dependence, with different components decreasing with different functional forms.

In general, the analysis program triggers when the voltage from the singlet pulse rises above the lower discrimination threshold. If this event does not exceed the high discrimination threshold, the program searches for a corresponding signal in the second PMT within the coincidence window. Finding a coincident event triggers both an integration of each singlet pulse, and a counting of triplet state afterpulses, which have significantly lower amplitudes than the singlet pulse. After compiling some initial histograms of the afterpulse time dependence, the digitization window was set to 8 μs to maximize the sensitivity. The 1.5 μs prior to a singlet pulse trigger and last 3 μs following the 8 μs afterpulse counting window, were used to assess the beginning and ending background counts respectively.

As shown in Figure 3.13a, in the full beam mode, a significant number of afterpulses follow each singlet pulse trigger. By comparison, the number of afterpulses in the small beam trace data is noticeably lower, as seen in Figure 3.13b. We suspect that the increased afterpulse counts will have an effect on the particle identification technique.

As in the non-coincidence data, the coincidence data runs were taken with the cell containing natural helium, and doped natural helium, both with and without neutrons. A series of contour plots, correlating the area under each trigger pulse with its corresponding number of afterpulses were generated for each data set.

The difference in area distributions and after pulses can be seen clearly in Figure 3.14 – Figure 3.16. With no neutrons, the singlet decay pulses are followed by, on average, 3 afterpulses. Analysis of natural helium data showed a wider pulse area distribu-

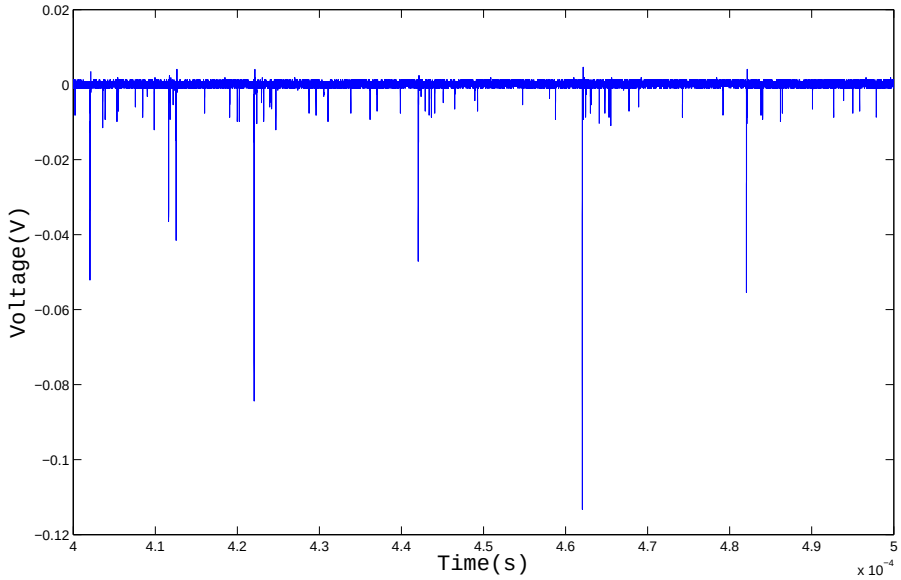

(a)

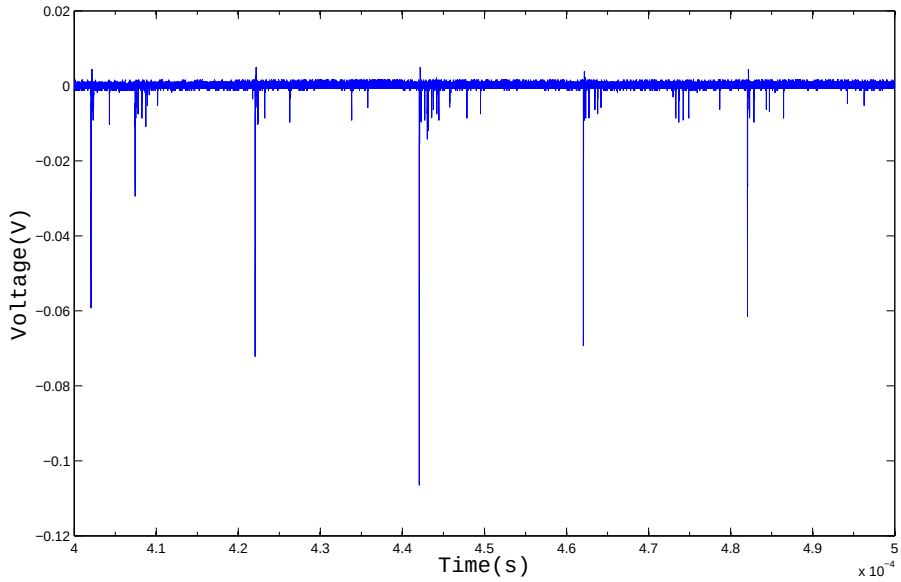

(b)

Figure 3.13: Sample oscilloscope traces at the high (full) and intermediate (small) beam fluxes at 90 mK. The singlet pulses in the full beam trace (a) are on average followed by a high density of triplet pulse decays. The small beam trace (b) shows fewer triplet pulse decays. The difference in the observed afterpulsing rates is attributed to frame overlap at the higher neutron fluence.

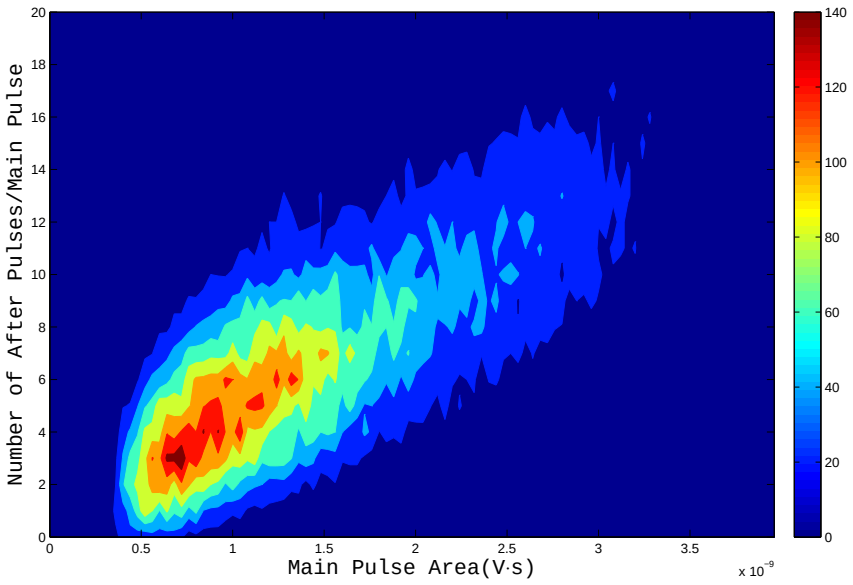

Figure 3.14: Contour plot correlating singlet pulse area with the number of triplet decay pulses with the cell containing natural helium at 300 mK.

tion, though still averaged 2 – 3 afterpulses following each singlet decay pulse.

As shown in Figure 3.16, the neutron capture peak is highly separated from the events shown in the background plots, in both pulse area distribution and after-pulsing. To determine, or rule out, any temperature dependence, a Gaussian fit of the form

$$\text{Fit} = z_0 + A \exp\left[-\frac{1}{2(1-\text{cor}^2)}\right]\left\{\left[\frac{(x-x_0)}{x_{width}}\right]^2 + \left[\frac{(y-y_0)}{y_{width}}\right]^2 - 2\cdot\text{cor}\left[\frac{(y-y_0)(x-x_0)}{x_0 y_0}\right]\right\}$$

was generated for each contour plot.[2] The resulting fit parameters are given in Table 3.4. The x_0 and y_0 terms correspond to the peak singlet pulse area and number of afterpulses respectively.

As expected, the fits show little variation in the main pulse area. This is a similar result to that seen in the two dimensional count rate analysis discussed earlier, with an average singlet pulse area of 1.5×10^{-9}V·s. The average number of afterpulses is also nearly constant for the small and ultra small beams, at 6 – 7 afterpulses/main pulse. The small

[2]All fits were made using the two dimensional gaussian fitting routine supplied in Wavemetrics Igor Pro 6.0. The resulting fit parameters had greater than 95% confidence.

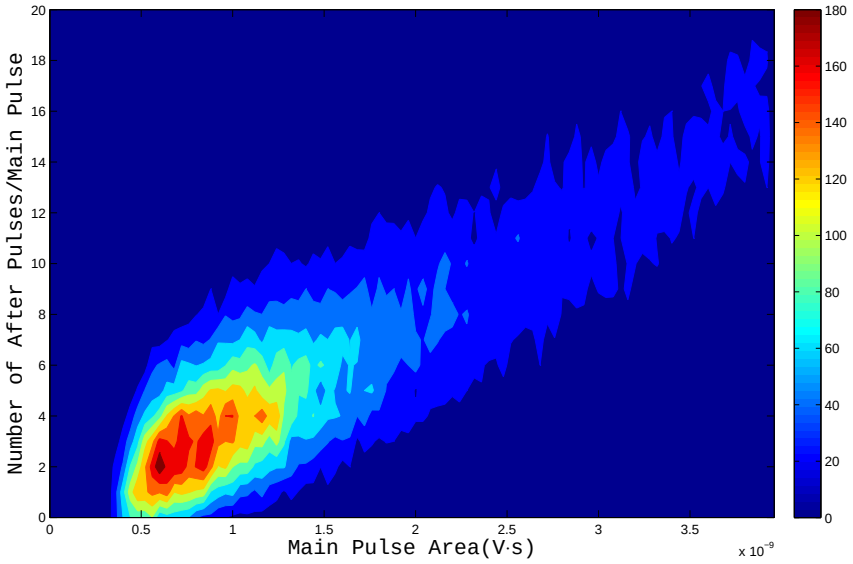

Figure 3.15: Contour plot correlating singlet pulse area with the number of triplet decay pulses with the beam blocked. The cell temperature is 300 mK.

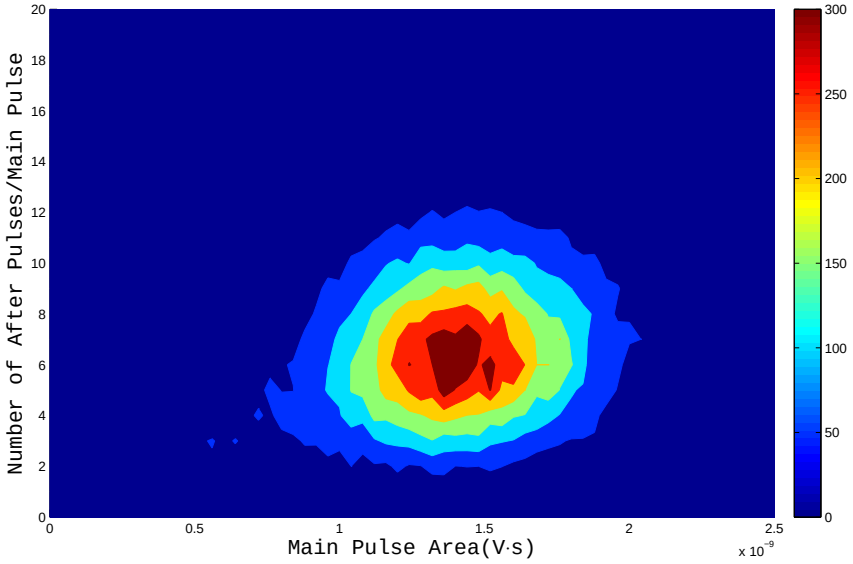

Figure 3.16: Contour plot correlating singlet pulse area with the number of triplet decay pulses for neutron capture at 90 mK at 20% of the maximum neutron flux

Beam size	T (mK)	z_0	A	x_0 (10^{-9})	$x_{width}(10^{-10})$	y_0	y_{width}
Full Beam	90 S1	0.57896	256.68	1.41	2.94	9.8969	3.1822
	90 S2	0.71808	250.43	1.43	2.90	10.189	3.1813
	350	0.65247	264.3	1.42	2.88	9.6659	3.1605
	500	0.71768	274.25	1.42	2.88	9.2399	3.0624
	630	0.7708	292.9	1.43	2.92	8.4749	2.9269
	1500	0.84513	248.38	1.44	2.90	11.207	3.3981
Small Beam	90	1.1045	273.2	1.41	3.08	6.4595	2.6221
	122	1.3442	320.95	1.41	3.04	6.4354	2.5861
	300	1.2533	323.23	1.41	3.04	6.4672	2.6002
	500	1.2561	327.7	1.40	3.03	6.4282	2.5913
	1500	1.3587	267.88	1.42	2.99	8.5178	3.0794
	1900	1.2582	186.38	1.43	2.99	10.362	3.5058
USB	90	1.2968	318.57	1.42	3.05	6.4637	2.6063
	90 No coin.	1.2248	264.61	1.41	3.18	6.4031	2.6269
	303	1.3122	331.6	1.41	3.04	6.4621	2.6241
USB2	1800	1.7515	164.37	1.38	3.70	9.1751	4.1131
	1900	1.9063	168.98	1.39	3.45	9.7562	4.089

Table 3.4: 3-dimensional Gaussian fit parameters for the neutron capture contour plots. $S1$ and $S2$ indicate Setup 1 and Setup 2, used for natural helium and doped natural helium runs respectively. The x_0 and y_0 terms correspond to the singlet decay pulse area and number of afterpulses respectively.

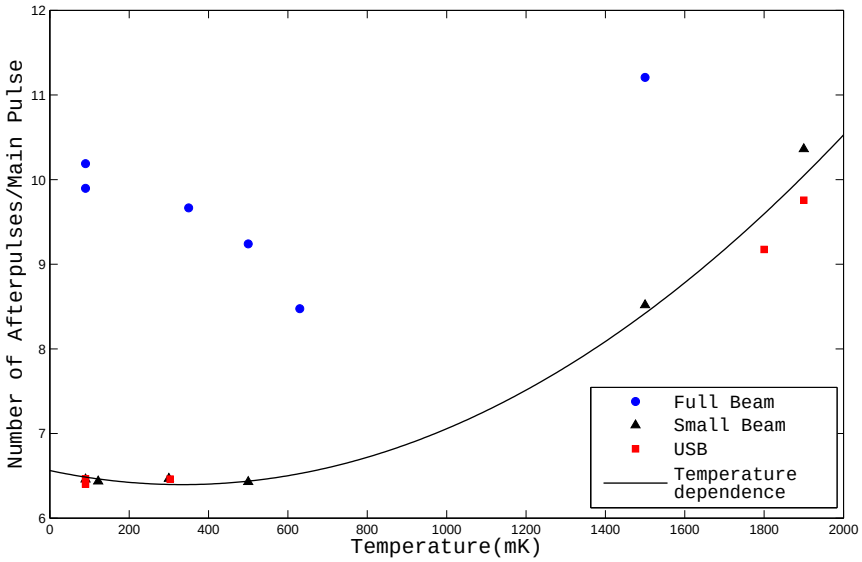

Figure 3.17: Average number of afterpulses following each singlet pulse trigger. The small and ultra small beam data show similar behavior, remaining nearly constant below 500 mK and increasing at temperatures near 2 K. The trendline is an estimate of the temperature response in the region where no data was collected. Fluctuations in the full beam data are attributed to frame overlap, contributing a large number of afterpulses to the overall signal background.

and ultra small beam afterpulsing is consistent below 500 mK and began to increase as the temperature approaced 1900 mK, similar to the temperature dependence previously seen using alphas, shown in Figure 3.2. The number of afterpulses for the full beam data, however, was considerably larger and had large fluctuations. This behavior is shown in Figure 3.17. The afterpulsing intensity is roughly 30 % higher at 1500 mK than at 90 mK.

To identify the source of the full beam afterpulse fluctuations, we performed an analysis of the individual PMT outputs. We considered the after-pulse train for each of the full beam data sets, as well as the background pulses. A contrast of the measured backgrounds and afterpulsing decay rate in the full and small beam configuration at $\sim$ 300 mK is shown in Figure 3.18. It was determined that in the full beam data, the count rates were large enough that there were a significant number of afterpulses from previous triggers contributing to the afterpulsing rate. On average, this translates to background counts that

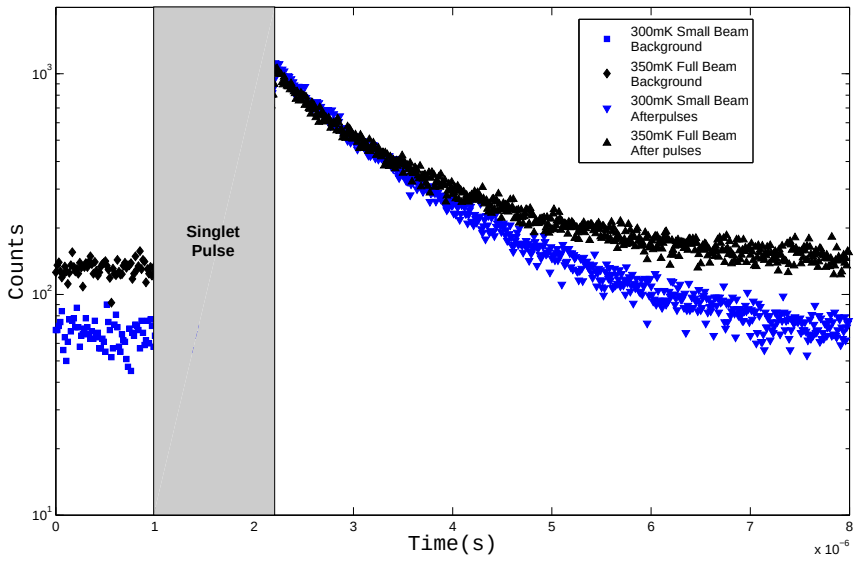

Figure 3.18: Comparison of afterpulse counts for the 300 mK small beam and 350 mK full beam. Shown at the beginning are the small beam and full beam background counts, which can be assumed to propogate through the afterpulse window.

were 3 times higher in the full beam data than for any of the smaller beam fluxes. The effect of the higher afterpulse backgrounds can be seen in the decay behavior of the full beam afterpulses, which clearly have a larger offset than the data taken with the reduced neutron fluences. Due to this significantly larger background term, the full beam data was not used in the analysis.

3.6 Conclusions

An analysis was performed of data collected at the Hahn-Meitner Institute to determine the feasibililty of using triplet decay counting as a means of particle identification. It has been demonstrated that the triplet decay counts resulting from neutron capture on ^{3}He in a liquid ^{4}He environment differs greatly from the electron afterpulse signature. Further, the behavior of these afterpulses is similar to the observed behavior of pulses resulting from α's in ^{4}He, decreasing with decreasing temperature. The behavior is constant below 500 mK. Because the neutron electric dipole moment experiment will be conducted

between 300 – 400 mK, the above described method shows promise as viable approach to background discrimination.

Chapter 4

Evaporative Purification of Liquid ^{4}He for the nEDM Experiment

The apparatus for the measurement of the neutron electric dipole moment will be constructed at the Spallation Neutron Source at Oak Ridge National Laboratory and will store ultracold neutrons in two measurement cells containing superfluid liquid helium. Polarized ^{3}He dissolved in the liquid will serve as a co-magnetometer. Because of the large spin dependent n-^{3}He capture cross section, and the expected neutron number density of $\sim 10^2/\mathrm{cm}^3$, the polarized ^{3}He concentration in ^{4}He must be $\sim 10^{-10}$. Once the ^{3}He atoms depolarize, they must be removed from the measurement cells, which are then replenished with polarized ^{3}He for the next measurement cycle. In the final step the depolarized ^{3}He atoms are removed from the liquid ^{4}He. This chapter will focus on the ^{3}He removal.

The total volume of liquid ^{4}He within the measurement cells and associated plumbing is 15 l. This includes the two acrylic cells, the ^{3}He injection volume, and the evaporator volume shown schematically in Figure 4.1. In each roughly 2000 s experiment cycle, an atomic beam of ^{3}He is spin – state selected using quadrupole permanent magnets. This polarized beam is directed upon the free ^{4}He liquid surface, where the atoms dissolve, forming a dilute ^{3}He/^{4}He solution. After a sufficient population of polarized atoms has been achieved, the ^{3}He is flushed into the two measurement cells by a thermal flux produced by a heater. The initial population of ^{3}He atoms in the injection volume is chosen so as to produce a polarized ^{3}He concentration x_3 of 10^{-10} in each of the measurement cells.

Recent experiments have placed the expected depolarization time of ^{3}He in the

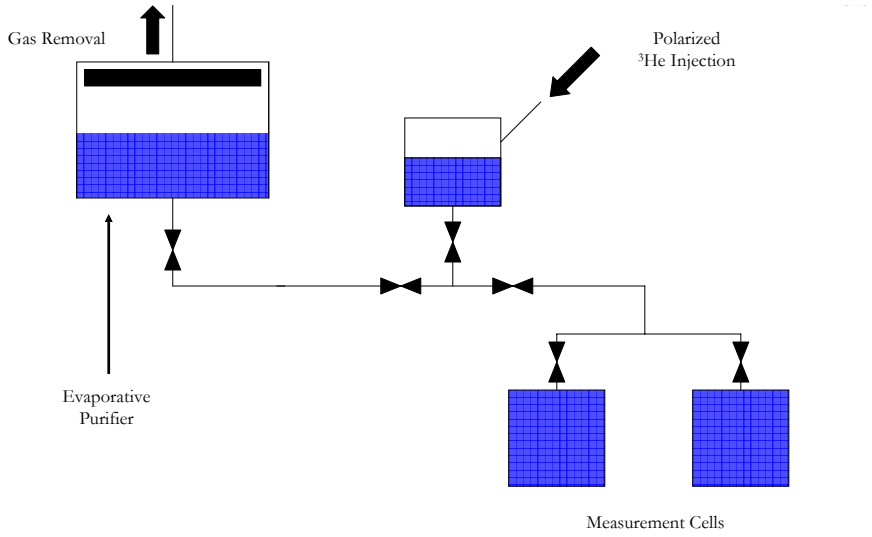

Figure 4.1: Layout of the ^{3}He injection and removal system for the nEDM experiment. At the beginning of a measurement cycle, polarized ^{3}He is introduced, via an atomic beam source, at the free ^{4}He liquid surface in the ^{3}He injection volume, where it dissolves. The polarized atoms are then flushed into the two measurement cells. After the atoms depolarize, they are flushed into the evaporator volume, where they are removed from the system.

geometry of the nEDM experiment at ~5000 s at 400 mK [78, 79]. The depolarized ^{3}He atoms can contribute to the signal background of the neutron capture measurement. The depolarized atoms are removed from the measurement cells using the same phonon transport process used to move atoms into the cells from the injection volume. The flush drives the depolarized atoms from the measurement cells to the ~25 cm^3 evaporator volume. The evaporator volume is then isolated from the measurement cells by closing a valve. The heat currents are removed and a new measurement cycle proceeds. The helium in the 25 cm^3 volume has a ^{3}He concentration of $\sim 10^{-8}$ or higher. These atoms are then removed.

It has been proposed to separate ^{3}He from ^{4}He using differential evaporation [59]. The following sections 1) describe the relevant properties of ^{3}He/^{4}He solutions, 2) outline a strategy for carrying out differential evaporation, 3) describe efforts to analyze x_3 in gaseous samples using a residual gas analyzer and, 4) describe the configuration of a dilution refrigeration cryostat for evaporator testing.

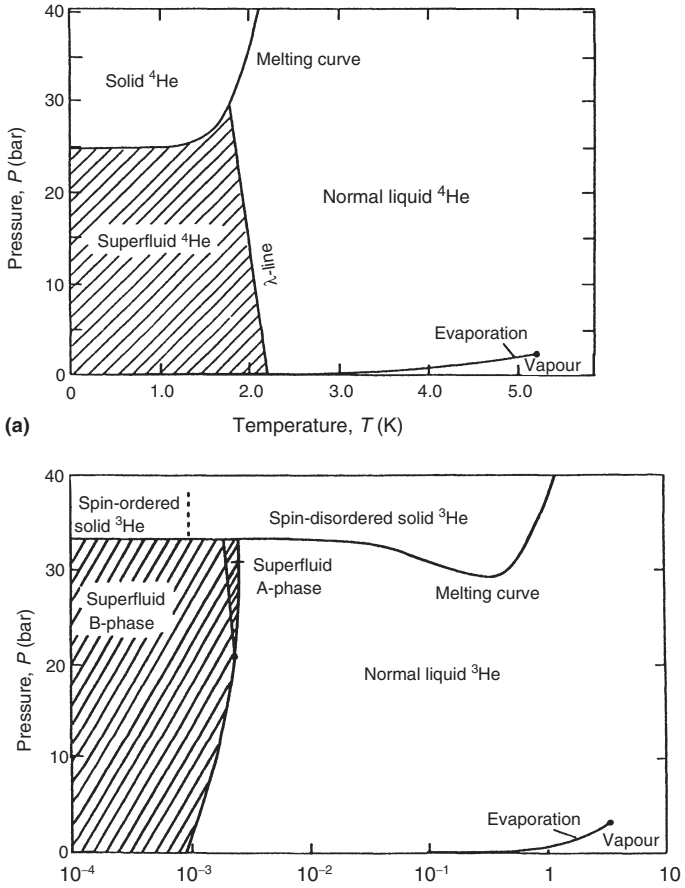

Figure 4.2: Phase diagrams of a) ^{4}He and b) ^{3}He from reference [80]. ^{4}He undergoes a superfluid transition at 2.17 K, while ^{3}He remains a normal fluid down to 2 mK.

4.1 Properties of ^{3}He/^{4}He Solutions

At temperatures below the superfluid transition of ^{4}He, the thermal and transport properties of dilute ^{3}He/^{4}He solutions depend upon excitations (rotons and phonons) in the superfluid, as well as ^{3}He - ^{3}He couplings. At temperatures below 2.17 K, ^{3}He and ^{4}He have very different properties. As an isotope with nuclear spin 1, ^{4}He obeys Bose statistics. Below the lambda point (T = 2.17 K), ^{4}He becomes a superfluid, exhibiting no viscosity and no entropy. As spin 1/2 particles, ^{3}He atoms obey Fermi statistics. The phase diagrams shown in Figure 4.2 illustrate this difference. Below 2 mK, ^{3}He atoms couple and behave like bosons, allowing a superfluid transition. At temperatures below the ^{4}He lambda point,

but above 2 mK, ^{3}He/^{4}He solutions behave as a Fermi liquid of ^{3}He quasiparticles moving within a ^{4}He vacuum.

For the ^{3}He concentration of $x_3 = 10^{-10}$ present in the neutron EDM experiment, we can expect the ^{3}He atoms to behave as an impurity in pure ^{4}He. The volume occupied by one ^{4}He atom in pure ^{4}He is $\approx 45.8\text{Å}^3$. The volume occupied by a ^{3}He atom in ^{4}He is 30 % larger, due to the smaller mass and larger zero point energy of the ^{3}He atom, is given by

$$E_0 = \frac{\hbar^2}{2ma^2}$$

where $a = (V_3/N_A)^{1/3}$ is the radius of the sphere defined by the ^{3}He atom [81]. The effective ^{3}He mass in the fluid is estimated from the classical behavior of a sphere in fluid,

$$m_{cl} = m_3 + \frac{1}{2} m_4 n_4 v_3 \tag{4.1}$$

where v_3 is the volume of fluid displaced by the sphere and $m_4 n_4$ defines the mass density of the fluid, and m_{cl} is the classically determined effective ^{3}He mass. From equation (4.1), we calculate a classical effective ^{3}He mass of $m_{cl} = 1.85\ m_3$. This effective mass of ^{3}He in ^{4}He is pressure dependent. This pressure dependence is given by

$$\frac{m_{cl}}{m_3} = \left(1 - .57\frac{n_4}{n_4^0}\right)^{-1} \tag{4.2}$$

where n_4^0 the ^{4}He density as temperature and pressure approach zero [82]. At a temperature of 350 mK, the effective ^{3}He mass has been measured between 2.3 m_3 and 2.7 m_3 [83, 84, 85].

We model the respective vapor pressures of ^{3}He and ^{4}He using the method followed by Wheatley *et al.* in designing the still of a dilution refrigerator [86]. The vapor pressure of each species is treated independently. For ^{4}He, the vapor pressure curve follows the Clausius-Clapeyron equation

$$P = A\ \exp\left(-\frac{L}{RT}\right) \tag{4.3}$$

where L is the latent heat of vaporization, R is the gas constant, T is the temperature, and A is a constant [87]. The latent heat is itself temperature dependent [56]. The measured latent heat for ^{4}He in the temperature range of 0.05 K to 3.0 K is shown in Figure 4.3. Below 1 K, the latent heat varies linearly as $L = L_0 + \frac{5}{2}RT$, where $L_0 = 59.83$ J/mol is the latent heat of vaporization at absolute zero. Below 1.25 K, one can express the ^{4}He vapor pressure as

$$P = \exp\left[i_0 - \frac{L_0}{RT} + \frac{5}{2}\ln(T)\right] \tag{4.4}$$

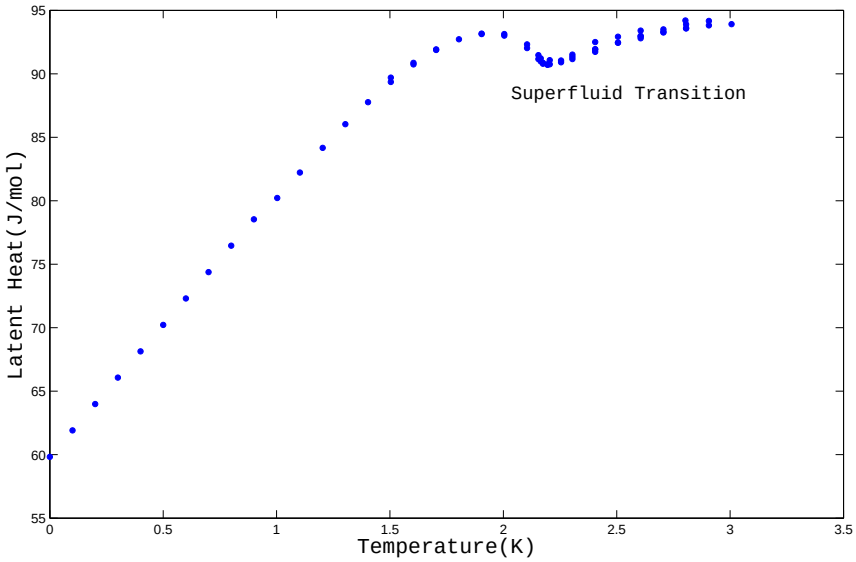

Figure 4.3: The latent heat of vaporization of ^{4}He as a function of temperature. This plot is a compilation of experimental results down to 1 K. Below 1 K, the latent heat has a linear dependence with temperature given by $L = L_0 + (5/2)RT$, with $L_0 = 59.83$ [88, 89, 90, 91].

where $i_0 = \ln[(2\pi m)^{3/2} k^{5/2} h^{-3}]$ [56]. Figure 4.4 shows the ^{4}He vapor pressure over the temperature range of interest.

The presence of ^{3}He has little effect upon the vapor pressure of the liquid ^{4}He. This is because the total vapor pressure of a system at equilibrium is defined as

$$P = \sum_{i=1}^{n} p_i x_i$$

with p_i the vapor pressure of each constituent and x_i its respective mole fraction or concentration. This expression is the equational form of Raoult's Law[92]. By rewriting this expression to describe the effects of ^{3}He on ^{4}He,

$$P = P_0 \left(1 - \frac{n_3}{n_4}\right) \tag{4.5}$$

where P_0 is the vapor pressure of the pure liquid, it is clear that, for the nEDM experimental ^{3}He concentrations, $\mathrm{P} \approx \mathrm{P}_0$.

Calculating the vapor pressure for ^{3}He begins from the Clausius–Clapeyron relation at the liquid–vapor transition, where the liquid and vapor chemical potentials are equal.

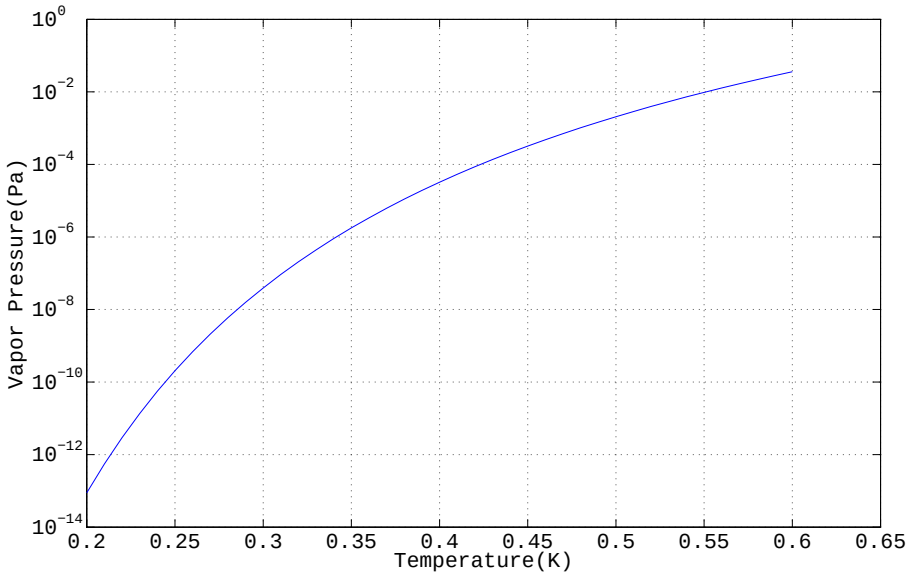

Figure 4.4: Temperature dependence of the ^{4}He vapor pressure below 1.25 K, defined as P = exp(i_0−L_0/RT+(5/2)ln(T)), where i_0 = ln $[(2\pi m)^{3/2}k^{5/2}/h^{-3}]$.

To define the chemical potential of the vapor state μ_v, we first describe the properties of the system in terms of the grand canonical partition function

$$\mathcal{Z} = \prod_i \left[\sum_{n_i} e^{\frac{(\mu-\epsilon_i)n_i}{k_B T}} \right]$$

for a system of noninteracting identical particles. The index i denotes the exact states that the system can occupy, with ϵ_i the energy of that particular state and μ the chemical potential. The different allowed states n_k for fermions and bosons give the result

$$\mathcal{Z}_i = \sum_{n_i} e^{\frac{(\mu-\epsilon_i)n_i}{k_B T}} = \begin{cases} 1 + \lambda e^{-\beta\epsilon_k} & \text{fermions} \\ \left(1 - \lambda e^{-\beta\epsilon_k}\right)^{-1} & \text{bosons} \end{cases}$$

where $\beta = 1/k_B T$ and λ is the fugacity of the system, defined as $e^{-\beta\mu}$. For a ^{3}He system, which behaves as a Fermi liquid, we can consider only the fermion case. It is from this expression that we define the grand canonical potential

$$\Omega = -PV = -k_B T \ln \mathcal{Z}$$

where ln $\mathcal{Z} = \lambda \sum_i e^{\beta\epsilon_i}$.

In the ideal quantum gas regime, the partition function $\mathcal{Z}$ can be rewritten as

$$\mathcal{Z} = e^{V\lambda\left(\frac{mk_BT}{2\pi\hbar}\right)^{\frac{3}{2}}}.$$

By defining the mean number of particles in the system as

$$\langle N \rangle = -\left(\frac{\delta\Omega}{\delta\mu}\right)_{T,V}$$

we arrive at the expression for the chemical potential of an ideal ^{3}He vapor as

$$\mu_{3_{vapor}} = k_BT\left\{\ln\left(\frac{P_3}{k_BT}\right) + \ln\left[\left(\frac{1}{2}\right)\left(\frac{2\pi\hbar^2}{m_3k_BT}\right)^{\frac{3}{2}}\right]\right\} \tag{4.6}$$

which follows from the ideal gas requirement $PV = nk_BT$. Because the liquid helium environment is not a true vacuum, the chemical potential of the liquid uses the effective ^{3}He volume and mass, meaning N/V is defined in terms of a concentration and effective volume, as well as the binding energy between ^{3}He and ^{4}He, resulting in the expression for the chemical potential given in equation 4.7 [93].

$$\mu_{3_{liquid}} = k_BT\left\{\ln\frac{x_3}{w_{0,4}} + \ln\left[\left(\frac{1}{2}\right)\left(\frac{2\pi\hbar^2}{m_3^*k_BT}\right)^{\frac{3}{2}}\right] - E_{0,3}\right\} \tag{4.7}$$

At the phase transition, equations 4.6 and 4.7 are equal, giving the temperature and concentration response for ^{3}He vapor pressure shown in equation 4.8.

$$P_3 = \frac{k_BTx_3}{w_{0,4}}\left(\frac{m_3}{m_3^*}\right)^{\frac{3}{2}}\exp\left(\frac{-E_{0,3}}{kT}\right) \tag{4.8}$$

The constants in equation 4.8 are $w_{0,4} = 27.5 \times 10^{-6}$ m^3/N$_A$ and $E_{0,3}/k_B = 2.7$ K. We assume the value of m^*/m to be within the range of 2.3 to 2.7. Over the measured range of the ^{3}He effective mass, at 350 mK, the ^{3}He vapor pressure can vary by as much as 20 % (Figure 4.5). Shown in Figure 4.7 are vapor pressure curves for ^{3}He ($m_{eff} = 2.5\ m_3$) and ^{4}He at a concentration of 10^{-8}, 10^{-10}, and 10^{-12}. The vapor pressures P_3 and P_4 will be used to calculate the differential evaporation rate of dilute ^{3}He/^{4}He solutions.

4.2 Removal of ^{3}He from ^{4}He through Differential Evaporation

The proposed method to remove depolarized ^{3}He from ^{4}He for the nEDM experiment is to evaporate the atoms from the liquid and adsorb them on a charcoal adsorber.

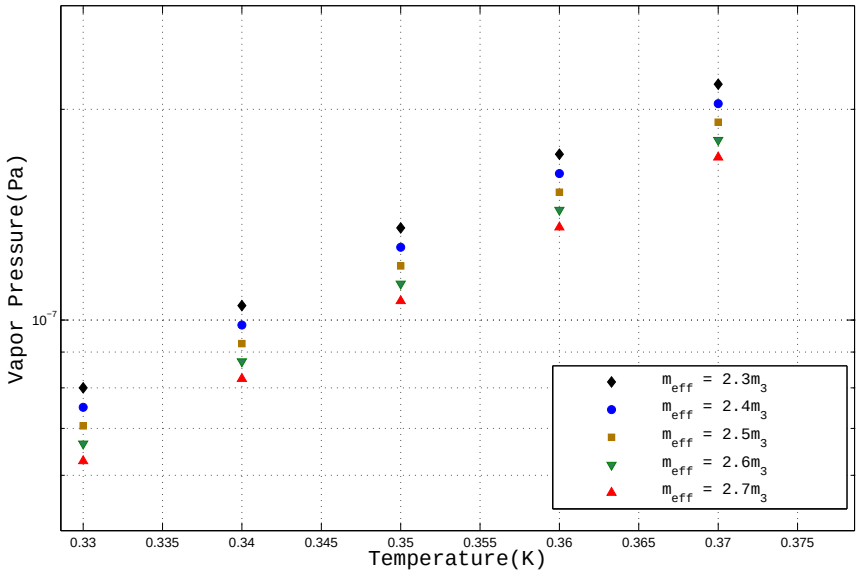

Figure 4.5: ^{3}He vapor pressure as a function of temperature. For a dilute ^{3}He/^{4}He solution ($x_3 = 10^{-8}$), the ^{3}He effective mass is $m^* = 2.3m_3 \leq m_{eff} \leq 2.7m_3$, resulting in up to a 20% variation in ^{3}He vapor pressure.

The adsorber has a limited gas capacity, which requires that it be regenerated in regular intervals. The efficiency of this process depends upon the relative vapor pressures of ^{3}He and ^{4}He. This process is limited by superfluid ^{4}He, which can climb up the inner walls of the evaporator where it can vaporize, increasing the pressure in the evaporator volume, thereby decreasing the evaporation rate.

The evaporative purifier is designed with a large pumping surface, a method to regulate superfluid film flow, and a pump to maintain low pressure in the evaporator volume. In this way, the evaporator functions much like the still of a dilution refrigerator, which removes ^{3}He from a ^{3}He/^{4}He solution. The cylindrical evaporator body has an inner diameter of 0.28 m, giving a free liquid surface area of 0.06 m^2. The liquid depth can be varied up to a maximum operational liquid depth of 0.05 m. A disk containing roughly 50 g of activated charcoal suspended above the liquid surface serves to capture the escaping gas. This plate can be anchored either at the cold plate, held at 1.5 K, or the 4.2 K inner vacuum chamber flange. The molar capacity of this adsorber sets an upper limit on the continuous operation time of the evaporator. At 4.2 K, the adsorptive capacity of activated charcoal for helium is approximately 4 mol/kg [94]. Thus, the charcoal used in the evaporator should capture roughly 0.2 mol of helium.

A diagram of the evaporative purifier is shown in Figure 4.6. Liquid is brought into and out of the evaporator volume via the bottom valve through a 0.16 cm (1/16") line connected to a second adjoining volume (lifter) that can be raised and lowered to displace the liquid. Once the desired liquid level is reached, as measured using a capacitance level detector, the evaporator volume is mechanically isolated using a low temperature VCR valve. For adsorber regeneration, the liquid is removed and isolated from the evaporator, which is then evacuated via a 1.27 cm (0.5") pumping line. As the purifier is pumped out, the charcoal is heated to a temperature of approximately 15 – 20 K.

The purification efficiency is determined by the respective vapor pressures of ^{3}He and ^{4}He and maintenance of a low pressure environment during purification. The evaporation rate from the free surface of a dilute ^{3}He/^{4}He solution is

$$\left(\frac{dn}{dt}\right) = 2.48A\left(\frac{dn_3}{dt} + \frac{dn_4}{dt} - P_0\right)T^{-\frac{1}{2}} \tag{4.9}$$

derived from the Langmuir formula [95, 96]. The linear dependence of the rate equation on surface area means that the process prefers a large free surface to maximize purification

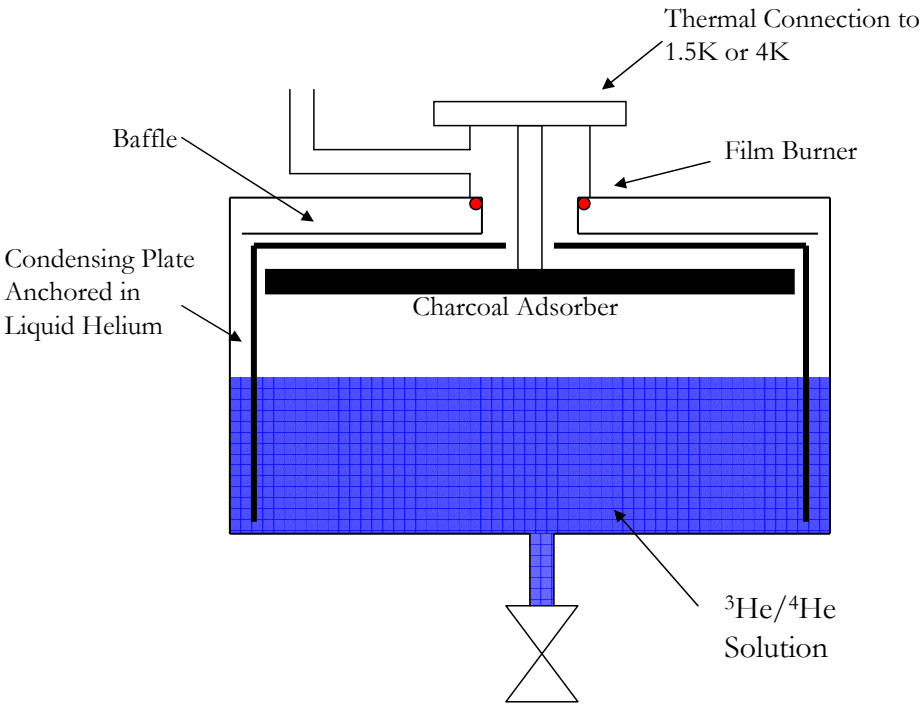

Figure 4.6: ^{3}He/^{4}He evaporative purifier, designed to remove ^{3}He impurities from superfluid ^{4}He. The 50 g of activated charcoal can be kept at 1.5 K or 4.2 K to improved gas adsorption. The film burner eliminates superfluid film flow by vaporizing the the atoms in the film, which are then redirected to the liquid below by the baffle and condensing plate.

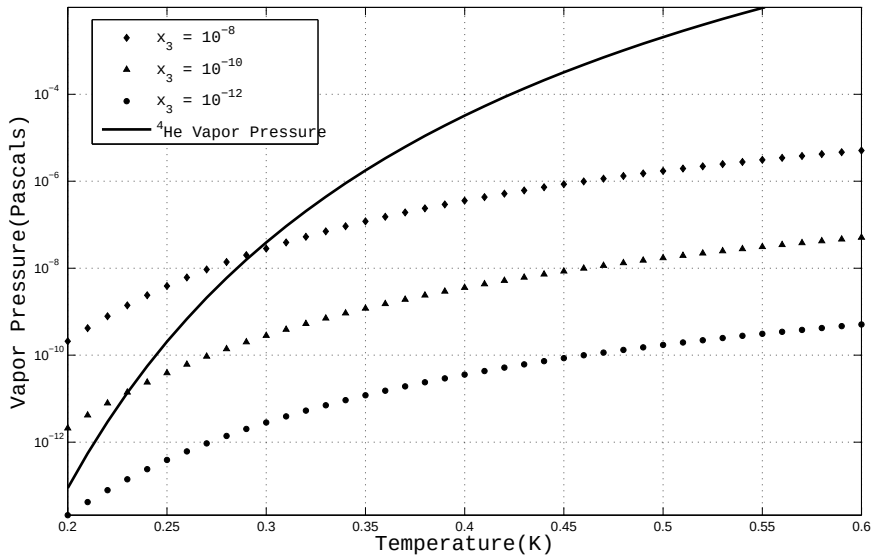

Figure 4.7: Comparison of ^{3}He vapor pressures for $x_3 = 10^{-8}$, 10^{-10}, and 10^{-12} with the ^{4}He vapor pressure. Values of P_3 were calculated using an effective ^{3}He mass m* =2.25m$_3$

efficiency. Tying the maximum evaporation rate to vapor pressure is the assumption that during operation,

$$\frac{dn_3}{dt}/\frac{dn_4}{dt} = P_3/P_4. \tag{4.10}$$

From the graph of the vapor pressures of ^{3}He and ^{4}He shown in Figure 4.7, for several ^{3}He concentrations, it is clear that at lower temperatures, the vapor pressure of ^{3}He is enhanced relative to ^{4}He. The ratio of vapor pressures as a function of temperature, P_3/P_4 for a ^{3}He concentration of $x_3 = 10^{-8}$ is shown in Figure 4.8.

At a given temperature, depending upon the ^{3}He concentration, the vapor pressure of ^{3}He becomes greater than that of ^{4}He. Though evaporative purification can be carried out over a wide range of temperatures, higher temperature operation leads to an increased removal of ^{4}He, which would quickly saturate an adsorption pump. A second limiting factor is the background pressure in the evaporator volume, denoted as P_0 in equation 4.11. This term is a fraction of the temperature dependent vapor pressure, written as

$$P_0 = C\,(P_3 + P_4) \tag{4.11}$$

where C is a constant dependent on the evaporator geometry.

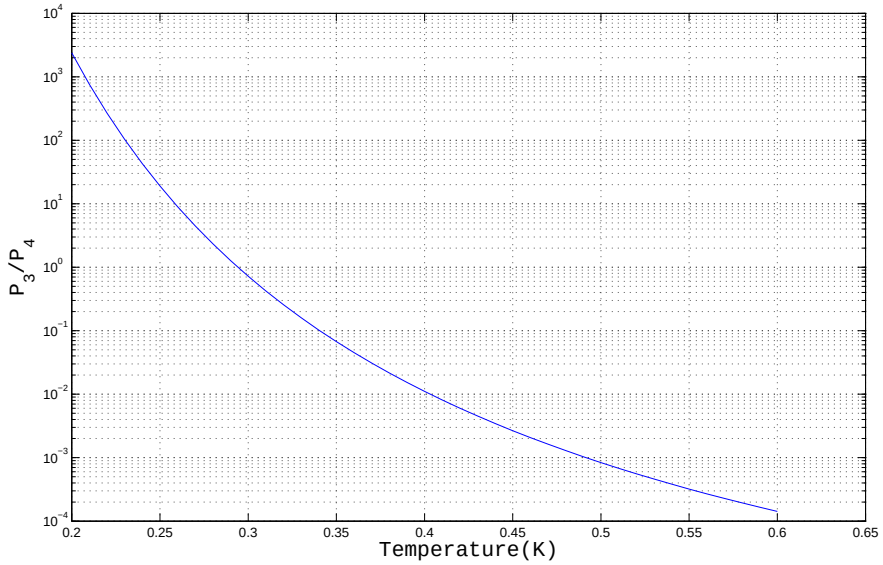

Figure 4.8: Ratio of the vapor pressures ^{3}He:^{4}He, for $x_3 = 10^{-8}$, $m^* = 2.25m_3$ from T = 0.2 − 0.6 K.

The background pressure is determined by the statistical probability of physisorption on the charcoal adsorber and the degree to which ^{4}He film flow can be controlled. The behavior of this background for values of C from 0 % to 60 % is shown in Figure 4.9. The background term sets an upper limit on the evaporation efficiency and must be kept as low as possible. Because the vapor pressure for ^{3}He is concentration dependent, as defined in equation 4.8, as x_3 decreases, the rate of ^{3}He removal decreases exponentially. A model of the effect of concentration on evaporation rate is shown in 4.10. The evaporation rate is seen to decrease by two orders of magnitude over one purification cycle.

The expected number of moles of ^{4}He removed in lowering the ^{3}He concentration by two orders of magnitude is shown in Figure 4.11. The amount of ^{3}He gas removed is constant at $\sim 10^{-5}$ mol. From Figure 4.11, it is apparent that above ∼350 mK, ^{4}He makes up the majority of the vapor and therefore sets the upper limit on the duration of continuous evaporator operation.

At an operating temperature of 400 mK, the charcoal will adsorb $\sim 10^{-3}$ mol of ^{4}He per cycle. Thus, at this temperature, a 50 g adsorber will saturate after roughly 200

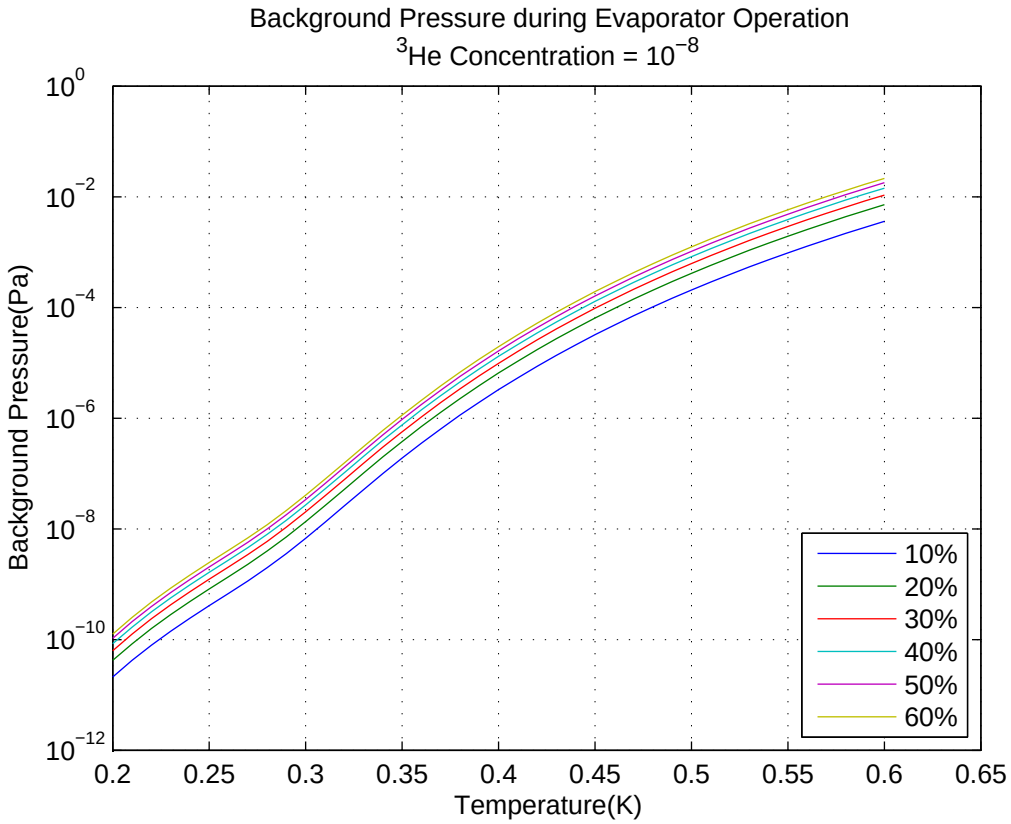

Figure 4.9: Background pressure, defined as P_0 = C(P$_3$+ P_4), during evaporator operation, where P$_3$ and P$_4$ are the vapor pressures of ^{3}He and ^{4}He respectively. Temperature dependent background curves are shown for C = 10, 20, 30, 40, 50, and 60 %.

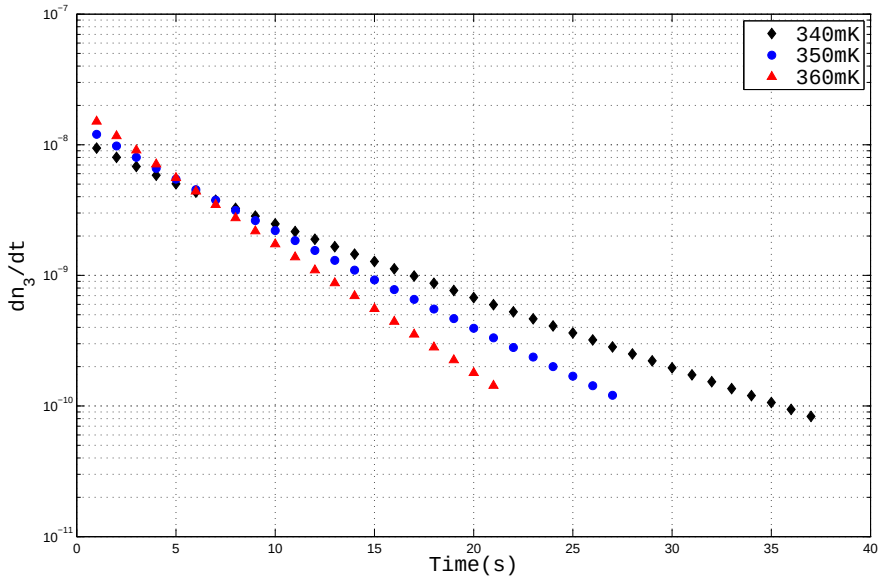

Figure 4.10: The molar removal rate of ^{3}He during a purification run cycle. The starting and ending ^{3}He concentrations are x_1=10^{-8}, and x_2=10^{-10} respectively, with a background contribution $P_0 = 30$ %.

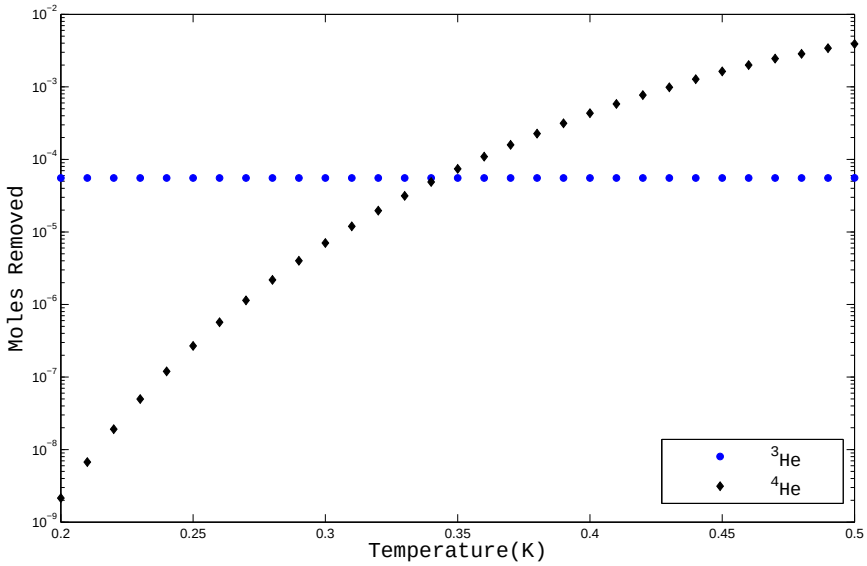

Figure 4.11: Expected number of moles of ^{4}He evaporated from the ^{3}He/^{4}He solution in lowering x_3 from 10^{-8} to 10^{-10}. This figure uses a background of $P_0 = 0$.

cycles. The length of a purification cycle varies with temperature. As shown in Figure 4.12, at a temperature of 400 mK, a purification cycle should be $\sim$ 100 s. As the temperature is lowered to 200 mK, the purification time increases by 2 to 3 orders of magnitude. The number of purification cycles between adsorber regenerations is shown in Figure 4.13.

Helium atoms leaving the liquid also adhere to the inner walls of the evaporator chamber, forming a film several nanometers thick. At temperatures above the λ–point, this film is rendered immobile, due to van der Waals interactions between the wall and ^{4}He. Below 2.17 K, this layer behaves as a superfluid, having no viscosity and therefore becoming mobile.

During evaporator operation, the main pumping line will have a temperature gradient, spanning from 350 mK to room temperature. The temperature gradient creates a gradient in the chemical potential of the film [97]. This chemical potential gradient drives the mobile film towards the warmer parts of the cryostat.

As the film climbs a surface, it has a thickness defined by the equilibrium condition

$$\mu_f = \mu_l + \mathrm{mgh}$$

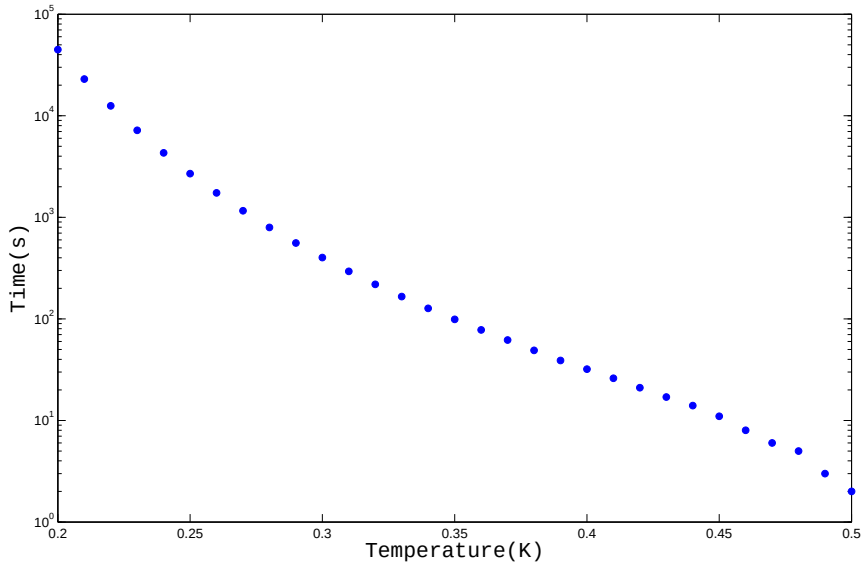

Figure 4.12: Purification time as a function of temperature with $P_0 = 0$.

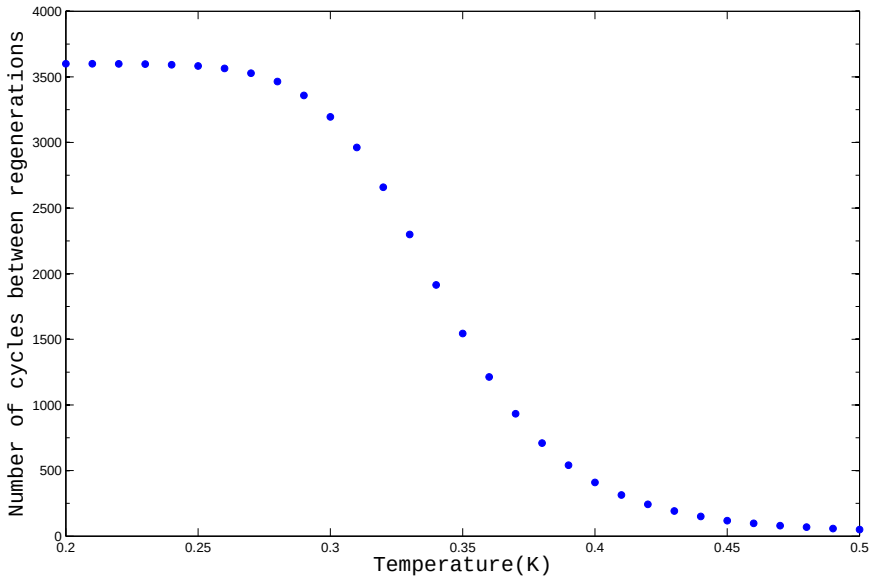

Figure 4.13: Number of purification cycles attainable before it is necessary to regenerate the charcoal adsorber. This figure uses a background of $P_0 = 0$.

where μ_f and μ_l are the chemical potentials of the film and liquid respectively, and h is the height of the film above the liquid surface [98]. At a height h above the liquid surface, the film thickness $d \simeq 30h^{-1/3}$, with h in centimeters and d in nanometers [80].

For a cylindrical pipe, the volumetric flow rate is proportional to the pipe circumference, film thickness, and the critical velocity, v_c, defined as the maximum allowable film velocity for a given geometry. Below this critical velocity, the film flow is frictionless. At pipe diameters D$\sim$1.0 cm, $v_c \propto D^{-1}$[99].

Because the evaporator, thermally connected to the dilution refrigerator mixing chamber, is at the lowest temperature in the cryostat, the superfluid film flows up the evaporator walls to the main pumping line. The rate of this flow is given by

$$Q = 2\pi R_0 C$$

where $2\pi R_0$ is the circumference of the cylindrical pumping orifice and C is inversely proportional to the temperature of the liquid. Thus, the superfluid flow rate increases with decreasing temperature [100, 101, 102, 103].

The volumetric flow rate, in cc/hr, into the evaporator orifice is defined as

$$\dot{V} = 2\pi R d v_c \tag{4.12}$$

where R is the pipe radius, d is the film thickness, and v_c is the critical velocity. For our approximately 1.27 cm (0.5") pumping line, we estimate the critical velocity, in cm/s from

$$v_c = \frac{0.75}{d} \times 10^{-4} \tag{4.13}$$

where d is the film thickness, typically less than 5 nm. We use equation 4.13 to calculate an expected range of critical velocities, shown in Figure 4.14. This flow rate is minimally affected by the low ^{3}He concentration [104].

It is reasonable to assume a film thickness of less than 5 nm [80]. For a film thickness of 2.5 nm, we calculate a volumetric flow rate of 2.75×10^{-4} cm^3/s. This expected rate is comparable to the measured flow rate per unit perimeter of $\sim10^{-4}$cm^3/s of superfluid film on copper and stainless steel [105]. Using the liquid ^{4}He molar volume of 27.5 cm^3/mol, this volumetric flow corresponds to a molar flow rate of 1.0×10^{-5} mol/s.

Superfluid film flow can potentially be the greater source of background pressure. Any superfluid film that reaches the higher temperature areas of the system vaporizes and

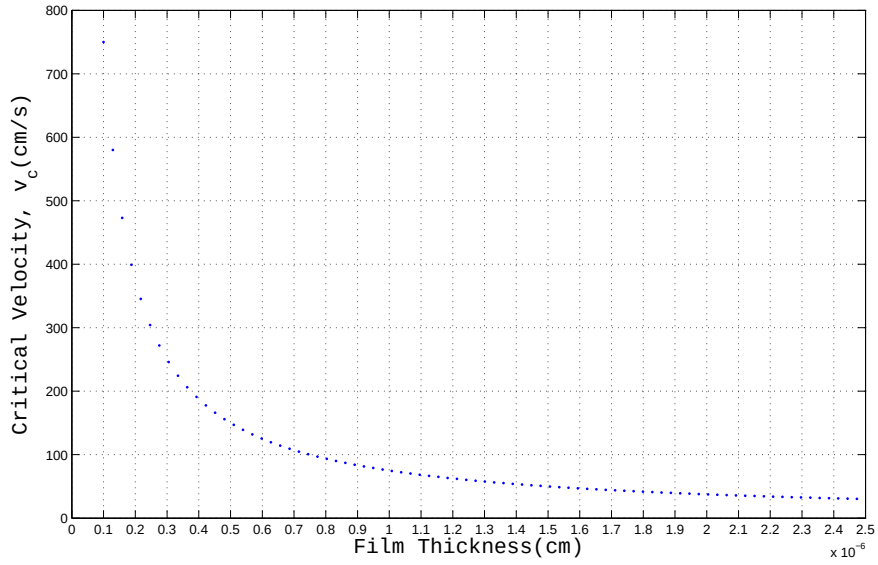

Figure 4.14: Critical velocity of superfluid ^{4}He film flow as a function of film thickness. The film thickness varies inversely with the height above the liquid.

could then be adsorbed on the pump. Therefore, the evaporator is designed to minimize the superfluid background contribution.

We prevent the film from reaching the main line through the use of a film burner. The film burner is used to raise the temperature of a portion of the 1.2 cm (0.46") evaporator pumping line. The section of pipe heated by the film burner must be sufficiently warm to immobilize the film. The design of this film burner is similar to one used in controlling film flow in the still of a dilution refrigerator [106]. If the film reaches the film burner, it is vaporized. The ^{4}He atoms are then free to move between the evaporator inner walls and baffle. The baffle is designed to minimize the probability of these atoms reaching the pumping lines by directing them back down to the liquid surface.

Once purification is complete, the charcoal must be regenerated. Before regenerating the charcoal, we first empty the evaporator volume of liquid by raising the lifter. This evacuation is monitored using the capacitance level detector, mounted in the evaporator. A low temperature mechanical valve is used to close the fill line, isolating the liquid from the chamber.

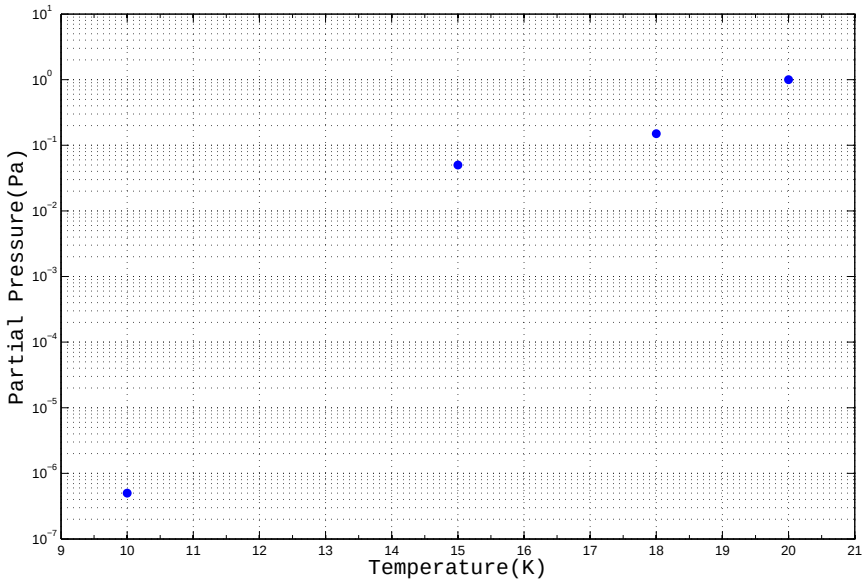

Figure 4.15: Ambient pressure in the evaporator volume required for charcoal regeneration. The points shown were measured in ^{3}He and ^{4}He gas desorption studies on activated charcoal by Salmelin *et al.* [94].

The adsorptive capacity of activated charcoal is both pressure and temperature dependent. At 4.2 K, the charcoal has a ^{4}He capacity of $\sim$4 mol/kg, at an operating pressure less than 10^{-10} Pa. To regenerate the charcoal adsorber, it is heated to 15–20 K, while the chamber is pumped through a 1.27 cm ($1/2^{"}$) stainless steel line using a Varian SD451 mechanical pump. As the temperature of the charcoal increases, its adsorptive capacity decreases, causing the atoms to desorb. The chamber pressure must be kept sufficiently low, $\sim$1 Pa. Otherwise, the ambient gas can inhibit desorption.

In the nEDM experiment, the evaporator must be regenerated at 15 – 20 K while the other components remain at 400 mK. Further, the heat loads must be kept within the limits of the cooling power of the dilution refrigerator. We apply similar constraints to our test apparatus, which has a cooling power of about 1.5 mW at 300 mK.

4.3 Adsorption/Desorption Kinetics of Gas on Charcoal

Activated carbon has a high adsorption capacity due to its large surface area to volume ratio. Adsorption should occur with near unity probability at low temperatures, meaning that the sticking coefficient for helium on charcoal approaches unity as the temperature goes to zero. This behavior is described by Henry's Law

$$\kappa = xp \tag{4.14}$$

where κ is Henry's Law coefficient, with units of pressure/concentration x is the amount adsorbed, and p is the pressure. When extended to the case of a microporous adsorber, the Henry's Law relation becomes

$$\kappa = \frac{V^P}{RT}\left(e^{-\frac{\phi}{k_B T}} - 1\right) \tag{4.15}$$

where V^P is the pore volume and ϕ is the potential energy of the surface [107]. The limit of adsorption is thus the free surface of the charcoal micropores. In the case of ^{3}He-^{4}He mixtures, the ^{3}He atoms preferentially adsorb on helium atoms, rather than on the substrate [108]. This is the case even when ^{4}He atoms only partially cover the substrate surface. Because we expect ^{3}He/^{4}He ratios of $\sim 10^{-2}$ - 10^{-3} at the adsorber, we will primarily discuss the properties of ^{4}He adsorption on activated charcoal.

At a given pressure, the extent of ^{3}He and ^{4}He adsorption depends upon the temperature and the enthalpy of adsorption. The magnitude of the enthalpy is an indication of the binding energy between the ^{3}He and ^{4}He atoms and the activated charcoal. The pressure dependent capacity and heat of adsorption for a charcoal adsorber are given in Figure 4.3. During adsorption, the charcoal will be held at 4.2 K. We measure the pressure in the evaporator volume using a thermocouple gauge read by a Terranova 934 controller down to 10^{-3} torr (.133 Pa). As the system cools, the pressure will be much less, as all gases, with the exception of helium, freeze out before one reaches 4.2 K. At the purification temperature of 350 mK, we can assume a chamber pressure of less than 10^{-5} Pa. Under these conditions, the enthalpy of adsorption is $\sim 20 \times 10^3$ J/kg from Figure 4.3.

A single purification run involves the removal of 10^{-4} moles of ^{4}He and 10^{-6} moles of ^{3}He in roughly 200 seconds. This is 0.005 % of the adsorber capacity. Thus, for a single purification run, the heat load due to helium adsorption is 0.25 mW.

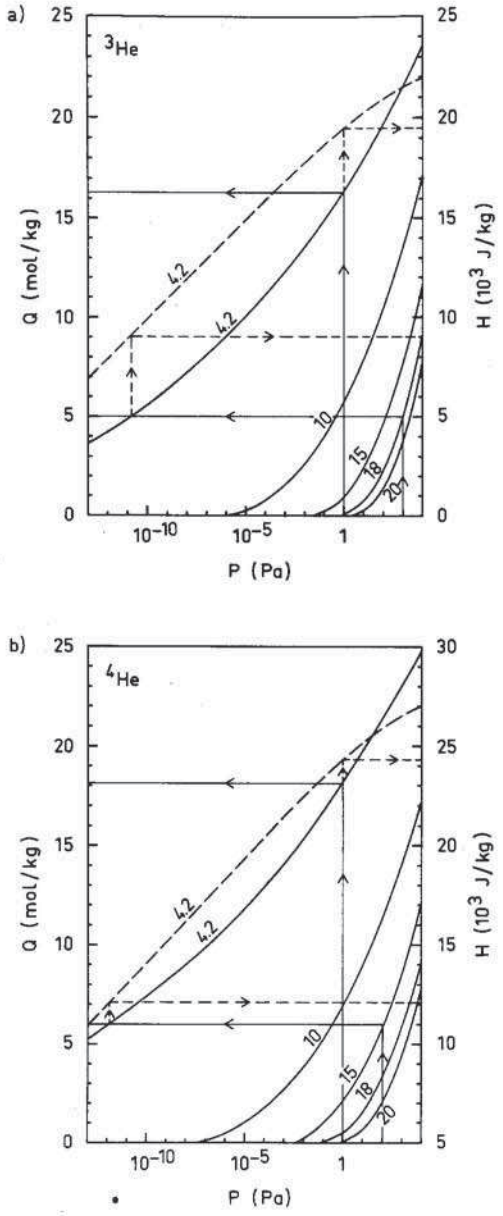

Figure 4.16: Adsorption of a)^{3}He and b)^{4}He on activated charcoal at T = 4.2, 10,15, 18, and 20 K. The dashed curve is the enthalpy H of the adsorption process at 4.2 K. Solid lines are adsorption isotherms [94].

Upon saturation, the charcoal must be thermally regenerated. Because the surface area of adsorption for activated carbon can be approximated as a graphite surface, one can assume that for a weakly bound physisorbed film, the general rate equation has the form,

$$\tau = \tau_0 \exp\left(\frac{E}{k_B T_s}\right) \tag{4.16}$$

where E is the binding energy, and T_s is the temperature of the substrate. In helium flash desorption experiments, between 5 K and 11 K, the constant τ_0 has been measured at approximately 10^{-9} s[109]. The desorption rate, in atoms/second, is the inverse of this time constant.

Under equilibrium conditions, it is also necessary to consider flux incident from the ambient vapor. In general,

$$\frac{dn}{dt} = \sigma\left(J_i - J_d\right) \tag{4.17}$$

with the J's defining the incident and desorbing fluxes respectively. These fluxes are defined as

$$J_i = \frac{P_g}{\sqrt{2\pi m k_B T_0}} \tag{4.18}$$

$$J_d = \frac{P_f}{\sqrt{2\pi m k_B T_f}} \tag{4.19}$$

P_g is the ambient pressure. In our apparatus, P_g should be less than 10^{-5} Pa, depending solely upon the vapor pressures of ^{3}He and ^{4}He. P_f is the pressure directly above the film of ^{3}He and ^{4}He atoms adsorbed on the charcoal. Because less than 0.2 mol of gas will be adsorbed in our purification process, we assume a negligible contribution from P_f during desorption.

By considering the film to behave as a thin layer of incompressible bulk liquid, P_f becomes

$$P_f(T) = P_l(T) \exp\left(\frac{\Delta V_{ext}}{k_B T}\right) \tag{4.20}$$

with P_l(T) the bulk liquid vapor pressure. The term ΔV_{ext} is the van der Waals potential of the substrate, defined as γ/δ^3; δ is the film thickness. For ^{4}He on graphite, γ is approximately 1.09Å. From 350 – 600 mK, the existing pressure dominates this rate, defined as:

$$-\frac{dn}{dt} = \frac{P_f(T_s, n)}{\sqrt{2\pi m k_B T_s}} - \frac{P_f(T_0, n_0)}{\sqrt{2\pi m k_B T_0}} \tag{4.21}$$

Under non-equilibrium conditions, i.e. with gas being removed, the rate constant is primarily a function of the chemical potential of the gas, as well as the substrate temperature, and has been defined alternatively as,

$$\tau = \frac{6 \times 10^{-12}}{T_0^{2.5}} \exp\left(-\frac{\mu_0}{k_B T_0}\right) \tag{4.22}$$

and

$$\tau = 10^{-9} \exp\left(-\frac{2\mu_0}{3k_B T_0}\right) \tag{4.23}$$

over a chemical potential range of 20 K to 94 K for ^{4}He on graphite. Thus, when the temperature is raised to 20 K, we expect the ^{3}He and ^{4}He atoms to desorb very quickly. Rapidly ramping the temperature up from 4.2 K to 20 K would likely exceed the maximum conductance of the pumping line, which may be as high as 10.3 l/s. The conductance of the line will likely be considerably lower as the 20 K desorbing atoms equilibrate with the 1 K sections of the pumping line. Therefore, it will likely be necessary to slowly increase the adsorber temperature, ending with a prolonged bakeout at 20 K.

4.4 Analysis of ^{3}He/^{4}He Ratios

To determine the effectiveness of the evaporative purifier, it is necessary to measure the relative ^{3}He and ^{4}He concentrations both before and after purification. The most common method used to determine ^{3}He/^{4}He ratios is mass spectrometry, whereby the two species are singly ionized and separated based on their respective mass to charge ratios [110]. A model of the evaporative purification process using our geometry gives a ^{3}He concentration in the desorbed gas of 10^{-2}. Thus, it may only be necessary to measure ^{3}He concentrations of 10^{-3}.

We have investigated the use of a Leybold L200 leak detector, capable of measuring masses 2, 3, and 4, and a Stanford Research Systems RGA100 residual gas analyzer with a default resolution of 0.5 amu at 10 % peak height. Each of these systems are considerably less expensive and more economical than a dedicated mass spectrometer. The success of the ^{3}He/^{4}He measurement depends on the removal of contaminants. Table 4.1 shows the mass to charge ratio of singly ionized ^{3}He and ^{4}He, as well as other species that could contaminate the measurement. In high vacuum ($P = 10^{-4} - 10^{-7}$ torr), hydrogen is produced from the dissociation of water vapor from vacuum system surfaces [111]. Given the natural

Species	M/e (amu)
$^3He^+$	3.01603
T^+	3.01605
HD^+	3.021825
H_3^+	3.023475
$^4He^+$	4.00260
HT^+	4.023875
D_2^+	4.028

Table 4.1: Mass 3 and 4 species that can affect the $^3He/^4He$ measurement. Much of the hydrogen based contamination can be removed with LN_2 and LHe traps.

abundance of deuterium in hydrogen of .015%, the HD and H_3 signals can interfere with the ^3He partial pressure signal, expected to have an amplitude of 10^{-8} to 10^{-7} torr. The natural abundances of D_2 and HT should be at least three orders of magnitude less than the expected 10^{-4} torr ^4He signal.

The difference in m/e between HD and ^3He is approximately 1/520. Determining the relative concentrations of the ^3He and HD would require a mass spectrometer with resolution greater than 1/600. Greater than 1/1200 resolution is necessary to resolve H_3. Using a mass spectrometer, accurate resolution of these like masses depends upon removing hydrogen from the test volume. This is the case even when using mass spectrometers with a m/e resolution of 600 or better [112].

We attempted to measure $^3He/^4He$ ratios using a Leybold L200 leak detector, capable of measuring masses 2, 3 and 4 with a measurement range of 0.1 mbar·L/s to 10^{-11} mbar·L/s. The maximium allowable inlet pressure of the leak detector is 3 mbar.

Four calibrated leaks were used to evaluate the performance of the L200. Based upon the manufacturer's specified loss rate of each of these leaks, as well as the initial filling conditions (1 atm, 22 °C), and an approximate volume of 9.1×10^{-5} m^3, it was possible to estimate the initial number of moles present in each. Under ideal gas conditions, i.e. $PV = nRT$, the collision rate of atoms with the walls of a given volume is defined as,

$$\text{rate} = \frac{PN_A}{\sqrt{2\pi MRT}}$$

where P is the calibrated leak pressure and $M = mN_A$. Therefore, the effusion rate can is

$$-\frac{dN}{dt} = \frac{APN_A}{\sqrt{2\pi MRT}}$$

Serial Number	Listed Leak Rate	Loss Rate	Measured Rate
Background(no leak)	$<10^{-12}$	$<10^{-12}$	$<10^{-12}$
1009	5.1×10^{-10}	$<$ .5%/year	1.8×10^{-9}
14018	5.0×10^{-8}	$<$ .5%/year	2.5×10^{-8}
7575	3.9×10^{-8}	$<$ .5%/year	6.0×10^{-10}
7355(^{3}He)	1.68×10^{-8}	$<$ 10%/10 year	3.5×10^{-8}
7355(^{4}He)	1.23×10^{-8}	$<$ 10%/10 year	1.2×10^{-8}

Table 4.2: Listed and measured leak rates for the four tested calibrated leaks(mbar·L/s). The leak rates were measured using a Leybold L200 leak detector. Before testing each calibrated leak, a background measurement was made with the leak valve closed.

where A is the area of the opening. This relationship is also used to define the pressure input to the L200 due to effusion from the calibrated leak,

$$-\frac{dP}{dt} = \frac{AP}{V}\sqrt{\frac{RT}{2\pi M}}$$

defining a logarithmic relationship between pressure and the atomic or molecular mass. Data for each of the calibrated leaks are given in Table 4.2.

Each leak also listed an estimated loss rate provided by the manufacturer. This information was used to determine the amount of gas present at the initial filling. However imprecise, it was still possible to estimate the gas charge for each calibrated leak be on the order of $2.5 - 6\times10^{-3}$ moles. Since the expected amount of gas exiting the charcoal is several orders of magnitude greater than the initial charging volume of each of the calibrated leaks, any of these leaks should function effectively as a test source for ^{3}He or ^{4}He.

The Leybold L200 leak detector can operate as a mass spectrometer, sweeping for mass to charge ratios of 2, 3, and 4 elements. Using a Labview interface, with an NI-USB 6009 data acquisition card, data from the the leak detector was used to produce a real time graphical display of each mass peak, as well as an output text file with the numerical anode and preamplifier voltages. The anode voltage sweep ran from 0 V to 1000 V, with corresponding preamp voltages from 0 V to 10 V. In this scheme, 1 V corresponds to a leak rate of 10^{-12} mbar·L/s, with each 0.5 V step corresponding to roughly a one order of magnitude increase in leak rate. The calculated pressure response for each calibrated leak using the L200 is given in Figure 4.17.

Measurements were performed with the leak detector tuned to each mass individ-

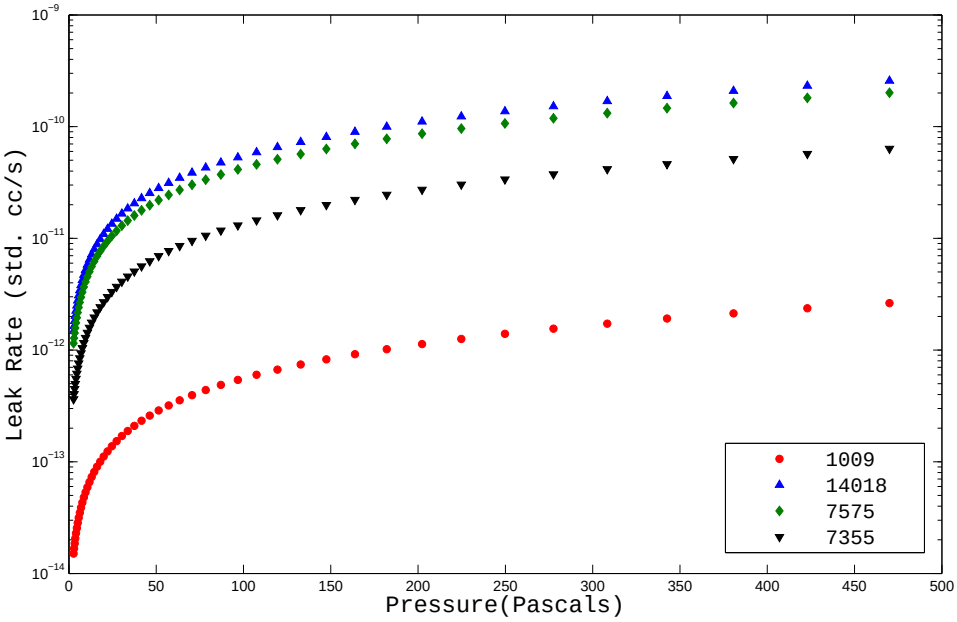

Figure 4.17: Leak rate, calculated for four ^{4}He calibrated leaks. The leak rate is determined by the pressure in each calibrated leak. A pressure > 100 Pa in calibrated leak 7355 is necessary to reach the 10^{-11} mbar·s resolution of the Leybold L200 leak detector.

Serial No.	Mass 2	Mass 3	Mass 4
Background(no leak)	$<10^{-12}$	$<10^{-12}$	$<10^{-12}$
1099	4.2×10^{-5}	1.6×10^{-8}	1.5×10^{-9}
14018	4.7×10^{-5}	1.6×10^{-8}	2.2×10^{-8}
7575	3.5×10^{-5}	1.2×10^{-8}	6.0×10^{-10}
7355	5.7×10^{-5}	9.7×10^{-8}	3.2×10^{-8}

Table 4.3: M/e ratios(mbar·L/s) of each calibrated ^{4}He leak for masses 2, 3, and 4, measured using a Leybold L200 leak detector. In addition to a mass 4 signal, each calibrated ^{4}He leak also produced relatively large mass 2 and mass 3 peaks.

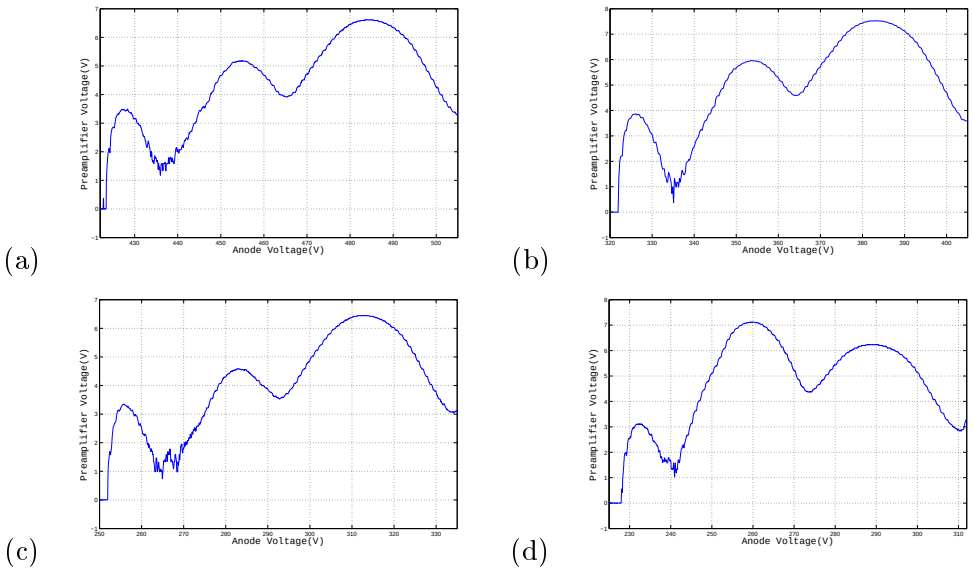

Figure 4.18: Leybold L200 leak detector mass sweeps of ^{4}He calibrated leaks a)1099 b)14018 c)7575 d)7355. Peaks 1, 2, and 3 are for masses 2, 3, and 4 respectively. The preamplifier voltage is proportional to the log of the leak rate.

ually for each of the four calibrated leaks. This data is summarized in Table 4.3. Of note is the high mass 2 peak present for each leak. The leak detector could also be operated in a sweep mode, which scans the entire mass range. The results of mass sweeps for each calibrated leak are shown in Figure 4.18 where the successive peaks represent mass 2, 3, and 4 going from low to high anode voltage. The preamplifier voltage varies inversely with partial pressure. Calibrated leaks 1099, 7575, and 14018 were all ^{4}He calibrated leaks. Only leak 7355 listed both ^{3}He and ^{4}He leak rates.

A mass 3 peak was measured in each of the mass sweeps. To eliminate backgrounds causing this peak, we first introduced a charcoal filled liquid nitrogen trap, which had no noticeable effect on the hydrogen signal. It was concluded that the contamination source was internal to the leak detector, possibly due to previous exposure to hydrocarbons. We therefore began research into making a ^{3}He/^{4}He measurement using a residual gas analyzer.

The mass differences among the individual mass 3, and likewise 4 species are too small to be resolved using our RGA. To use the RGA to measure the ^{3}He/^{4}He ratio, it is thus necessary to remove as much hydrogen as possible, and to lower the overall pressure in the measurement chamber. The primary reason for low (10^{-5} torr) pressure operation

is to maintain an ion free path. The ionized particles should reach the detector without colliding with other gaseous molecules, yielding unwanted reactions or resulting in a loss of charge from resulting wall collisions [110].

We removed gaseous impurities by baking the system at a temperature of 150° C for 24 hours and filtering the incoming gas stream. This is important because the monolayers of water vapor on surfaces can trap contaminants, including hydrocarbons from the turbo and mechanical pumps. With the exception of the 25 mm pump inlet, all gas lines are made of 0.635 cm (1/4") stainless steel tubing. All unions are either VCR seals with stainless steel gaskets, or all metal Swagelok seals. We use aluminum gaskets in place of rubber O - rings at the pump inlets.

The filtration system is partially adapted from an experiment conducted by the US Bureau of Mines to measure $^3He/^4He$ ratios [113]. This system is shown in Figure 4.19. The liquid nitrogen (LN_2) filter is U - shaped, consisting of a length of 0.635 cm (1/4") O.D. stainless steel tubing, containing granules of 6 – 14 mesh activated charcoal. The charcoal is secured by copper mesh at each end of the trap. During data collection runs, the trap is submerged in liquid nitrogen. This trap captures water vapor, backstreaming oil from the pumps, and filters incoming gas. The titanium trap consists of several lengths of pure titanium wire placed in the incoming gas stream. When hydrogen contacts the titanium surface, the atoms dissociate, with the free protons tunnelling into the bulk material. As an improvement over the Bureau of Mines method, we have added a liquid helium trap, consisting of a 0.635 cm O.D. (0.254 cm I.D.) tube within a 1.27 cm O.D. (1.143 cm I.D.) stainless steel tube. The space between the concentric tubes is partially filled with copper mesh to increase the capture surface area. When this trap is cooled to 4.2 K by insertion into a liquid helium dewar, only helium isotopes can pass through to the analysis chamber, while other atoms and molecules freeze in the trap.

The residual gas analyzer was used to test the effectiveness of the bakeout by measuring the water peak before and after a bakeout. After baking, the histogram of the gases present was dominated by carbon monoxide. The total pressure function of the RGA was used to measure the chamber pressure. Because this pressure was in good agreement with the carbon monoxide partial pressure, the magnitude of the CO peak was used as a rough estimate of the RGA chamber pressure. For optimum performance, the RGA manual only recommends operation at pressures below 10^{-4} torr; above this pressure, results can

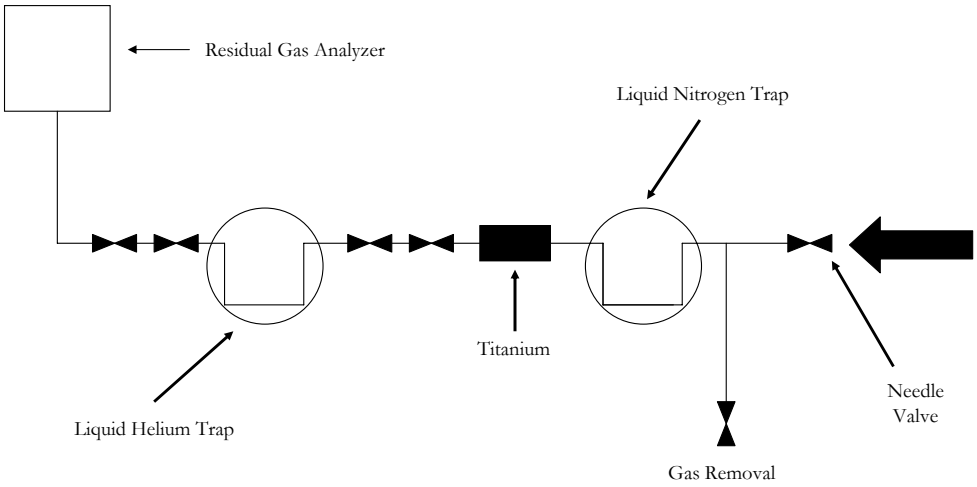

Figure 4.19: Gas handling system for real time analysis of desorbing gas composition. As the charcoal in the evaporator is baked out, a portion is siphoned off and flows through a titanium, liquid nitrogen, and liquid helium trap, before being analyzed by a Stanford Reasearch Systems SRS RGA100 residual gas analyzer. Each of the traps is in place to minimize H_2 and HD in the input gas and vacuum system .

be unreliable.

The system was tested using N_2, Ar, ^{3}He and ^{4}He. The first tests involved putting a small volume of nitrogen or argon gas into the analysis chamber through a needle valve and observing the pressure response of the RGA. From these initial tests, it was determined that the residual gas analyzer could preferentially detect the individual input gases, with little to no effect on the partial pressures of the background gases. Also, as a result of these tests, it was concluded that, for real time gas analysis, the needle valve minimum conductance of 10^{-3} mbar·l/s was too high, resulting in rapid saturation of the RGA spectrum. We therefore replaced the needle valve with a leak valve, lowering the minimum gas input rate to 10^{-10} mbar·l/s.

Once these qualitative tests were completed, we began a series of quantitative tests using pure ^{3}He and ^{4}He. To approximate the operating conditions of the evaporator gas analysis, a pressure of approximately 8×10^{-5} torr of ^{4}He was first put into the RGA analysis chamber using a calibrated ^{4}He leak. Against this background, ^{3}He was released into the RGA by filling a 0.3 cm^3 buffer volume using a 8.1×10^{-8} cc/s calibrated leak in 2.5 and 5 minute increments.

The relative rates of desorption for each species is unknown. Differential evaporation could remove more ^{4}He from the solution than ^{3}He. Because of this, it is possible that the ^{4}He signal will be detected before that of ^{3}He. We therefore tested this system by measuring the evolution of an initially weak ^{3}He signal against a 10^{-4} torr background pressure, as a test for real time analysis during desorption. Against a ^{4}He background of 10^{-4}, ^{3}He was introduced continually, at a rate of $\sim10^{-12}$ mol/s. We expected that a constant gas input rate would result in a linear pressure response.

The measured pressures ^{3}He partial pressures showed some nonlinearity below 10^{-7} torr. This non-linearity is consistent in the three runs shown in Figure 4.20. At these levels, the ratio of ^{3}He to ^{4}He in the RGA chamber is roughly 10^{-4}. As this level, it is possible that the ^{3}He atoms are deflected by the surrounding ^{4}He atoms before reaching the central analyzer. As the ^{3}He density increases, we see the expected linear response.

The numerous data collection runs also show some variation from day to day. We believe these variations are due to temperature changes in the liquid helium trap, which change its effective volume.

Because portions of the gas handling system are at temperatures well below 300 K,

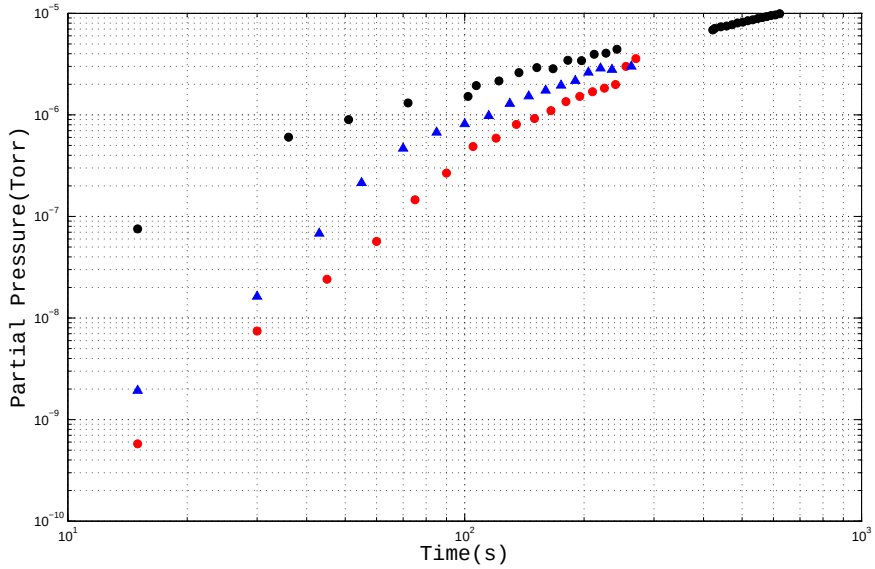

Figure 4.20: The SRS RGA100 pressure response. ^{3}He was added continually, at a rate of 8×10^{-8} cc/s, to the analysis chamber, which contained ^{4}He at a pressure of 10^{-5} torr. The data collection runs were taken over several days.

the total volume of the system is actually much greater than the 0.6 L room temperature volume of the gas handling system. The largest volume contribution comes from the liquid helium trap. At room temperature, the volume of this trap is approximately 0.08L. By considering the temperature of the trap, we can approximate the effective volume of this trap.

The liquid helium trap consists of a 0.25" O.D. (0.1" I.D.) tube within a 0.5"O.D. (0.45"I.D.) stainless steel tube. The space between the concentric tubes is partially filled with copper mesh to increase the capture surface area. Though the trap is placed into a liquid helium dewar, the temperature of the trap is not entirely at 4.2 K. Rather, because one end of the trap is at 4.2 K and the other is at 300 K, we must consider the temperature gradient across the tube. This gradient depends upon the temperature dependent thermal conductivity of the material. For types 304 and 310 stainless steel, the thermal conductivity is defined by

$$\log \lambda(T) = \sum_{n=0}^{8} a_n (\log T)^n$$

Coefficient	304SS	310SS
a_0	-1.4087	-0.8191
a_1	1.3982	-2.1967
a_2	0.2543	9.1059
a_3	-0.6260	-13.0780
a_4	0.2334	10.853
a_5	0.4256	-5.1269
a_6	-0.4658	1.2583
a_7	0.1650	-0.1240
a_8	-0.0199	0.0

Table 4.4: Coefficients for the temperature dependent thermal conductivity of Type 304 and 310 stainless steel. Material dependent expressions for $\lambda(T)$ can be found in reports from the Cryogenics Technology Group at the National Institute of Standards and Technology [114].

where $\lambda(T)$ is the thermal conductivity and coefficients for 304 and 310 stainless steel are given in Table 4.4.

We define a model for this system by assuming the portion of the trap that is below the liquid (l_{sub}) to be at 4.2 K. A temperature gradient is then defined from the liquid surface to the 300 K region. The temperature gradient in the trap depends on the stainless steel's thermal conductivity, which is itself temperature dependent. This variability in thermal conductivity can be modeled as a function of liquid helium level by using the relation

$$\dot{Q} = \lambda(T) A \frac{\delta T}{\delta t} \tag{4.24}$$

which describes heat conduction through a solid. $\dot{Q}$ is the total heat flow from 300 K to 4.2 K, $\lambda(T)$ is the temperature dependent thermal conductivity, and A is the tube cross-section.

The total heat $\dot{Q}$ is then used to calculate the incremental heat transfer in steps, leading from the high to low temperature sections of the liquid helium trap. For the 107 cm long trap, we chose a step size of 0.0254 cm. The temperature of each 0.0254 cm subsection is then related to the total heat by

$$\dot{Q} = \frac{T_f - T_i}{R_1 + R_2 + R_3 + \ldots} = \frac{T_f - T_1}{R_1} = \frac{T_1 - T_2}{R_1 + R_2} = \ldots \tag{4.25}$$

where T_n is the temperature of the nth subsection and $R_n = L_n/k(T) \cdot A_n$. The Ideal Gas Law is then used to calculate volumes for effective each subsections both above and

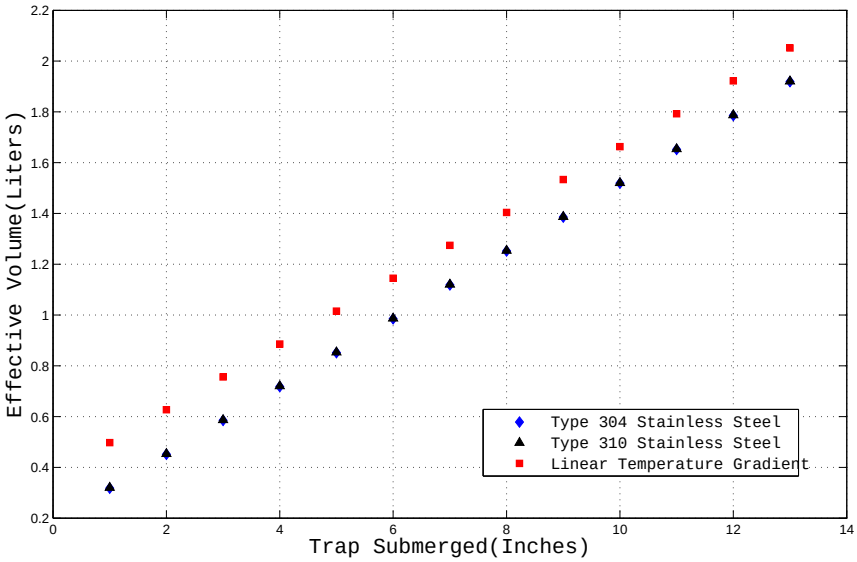

Figure 4.21: Change in effective liquid helium trap volume due to boiloff from the 30 l liquid helium dewar. The effective volumes were calculated assuming a portion of the trap to be at 4.2 K, due to submersion in liquid helium. For the exposed trap length, a temperature gradient was defined, based upon the thermal conductivity of the trap material, from 4.2 K to 295 K.

below the liquid level. The calculated volumes are then summed to give a total effective trap volume. By varying l_{sub}, we can model the effect of liquid level on the trap volume. The calculated variation in effective trap volume as the liquid helium boils off is shown in Figure 4.4. This is compared with the change in effective trap volume when a linear temperature gradient is assumed.

These effective volumes are then added to the volume of the gas handling system outside of the liquid helium trap to determine the total volumes experienced by the input gas. The Ideal Gas Law is then used to calculate the incremental change in pressure expected due to the continual input of ^{3}He gas. The rate of gas introduction used for these calculations is 3.3×10^{-12} mol/s, based on the 8.1×10^{-8} cc/s calibrated leak rate.

Variations in the measured ^{3}He partial pressure in the continuous flow mode were consistent with variations in the effective LHe trap volume. Measured ^{3}He partial pressures near the end of the approximately 10 day lifetime of the 30 l liquid helium dewar used

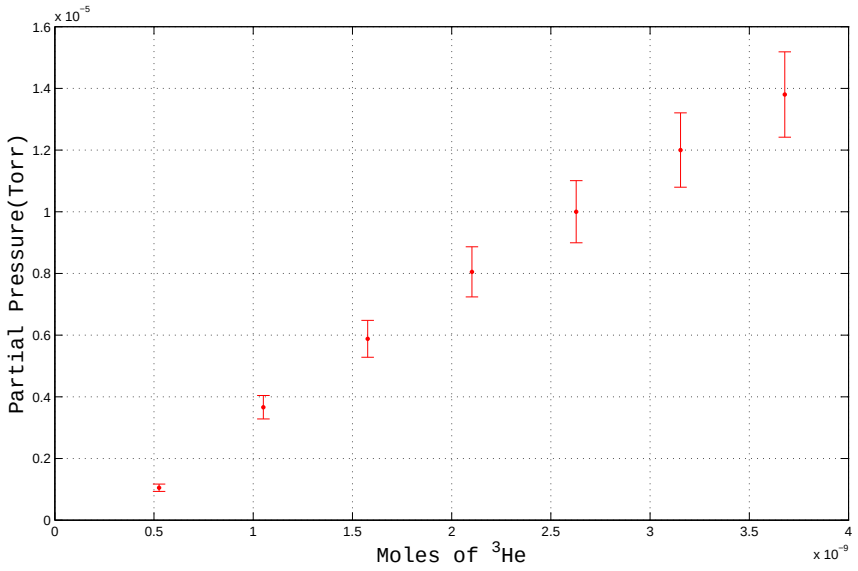

Figure 4.22: Partial pressure of ^{3}He, measured using a Stanford Research Systems residual gas analyzer. The number of moles is estimated from the $\sim 10^{-8}$ cc/s calibrated ^{3}He input rate. The difference in measured partial pressures across data sets is attributed to changes in the temperature, and thus, the effective volume, of the liquid helium trap.

to cool the trap can be as much as 5 times higher than with a full dewar. The degree of variation is shown quantitatively in Figure 4.22.

Subject to the limits of non-linearity and variable trap volume, we have confirmed a ^{3}He/^{4}He resolution of $\approx 10^{-3}$. This resolution has been confirmed for the current system, with negligible peak–to–peak interference.

4.5 Setup of the cryostat for the testing of evaporative purification

In order to test the evaporative purifier scheme, we have refurbished and configured a dilution refrigerator to house the purifier tests. Discussed here are the details of dilution refrigeration and the first operations of the evaporative purification cryostat.

Originally proposed in 1962 by London, Clarke, and Mendoza, the dilution refrigerator uses the latent heat of mixing of ^{3}He and ^{4}He for cooling [80]. These devices

have been used to reach and maintain temperatures of 25 mK in the earliest models, and commonly operate down to 4 mK today [115]. The cooling power of a ^{3}He–^{4}He dilution refrigerator comes from the mixing of a solution of these two isotopes at low temperature. Above 0.8 K, liquid mixtures of ^{3}He and ^{4}He exist in a single phase. Below this temperature, the isotopes spontaneously separate, forming two layers. Because of its lower density, the ^{3}He atoms form a nearly pure layer that floats on top of the ^{4}He rich phase. After separation, the ^{3}He concentration in the ^{4}He−rich phase remains constant at about 6.4 %. The ^{3}He–^{4}He boundary can be viewed as a phase separation between the "liquid" ^{3}He rich phase and dilute "vapor" phase. When ^{3}He atoms move downward across the phase boundary, the temperature decreases because energy is needed to overcome the interatomic forces. Because the ^{3}He concentration in the dilute phase remains constant at 6.4 %, continuous cooling is achieved by cycling ^{3}He through the system.

The DRI–430 dilution refrigerator is outlined in Figure 4.5. The phase separation occurs in the mixing chamber. ^{3}He circulation starts here, with a tube that begins in the dilute phase and extends to a part of the refrigerator known as the still. As atoms exit the dilute phase in the mixing chamber, they are forced by osmotic pressure into the still and are then pumped away. The still temperature is kept higher than that of the mixing chamber, usually between 0.6 – 0.7 K. Within this range, the vapor pressure of ^{3}He is much greater than that of ^{4}He, as shown in equations 4.4 and 4.8. Thus, by heating the still, ^{3}He can be preferentially removed.

Once ^{3}He atoms leave the dilute phase, atoms from the concentrated phase cross the phase boundary. Like evaporation, this phase transition results in a net increase in the entropy of the system. Accompanying this net increase in entropy must be a removal of heat from the mixing chamber and all thermally connected systems.

The cooling power of a dilution refrigerator is determined primarily by the rate of removal of ^{3}He atoms. Continuous operation requires a return of ^{3}He to the mixing chamber. After leaving the dilution refrigerator via a closed loop, circulating atoms go through several precooling steps before returning to the concentrated phase. The first is through tubing located in a bath of liquid ^{4}He at 4.2 K, external to the vacuum surrounding the dilution refrigerator. The atoms are then recondensed at $\sim$1.5 K in the part of the refrigerator known as the cold plate. A flow impedance beneath the cold plate causes a pressure buildup, increasing the rate of liquefaction. To decrease the heat load that would

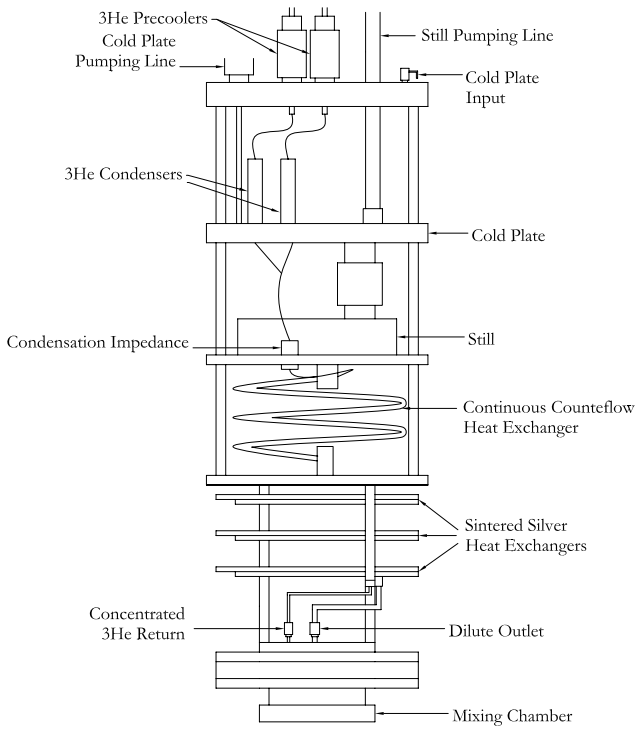

Figure 4.23: Schematic of the SHE DRI–430 ^{3}He–^{4}He dilution refrigerator used for the evaporative purifier. The refigerator consists of a cold plate, still, mixing chamber, a continuous heat exchanger, and three sintered silver heat exchangers. The cold plate and still operated at roughly 1.5 K and 0.7 K respectively. With a molar flow rate of $\sim$400 μmol/s, the mixing chamber produced a cooling power of 1 mW at 350 mK.

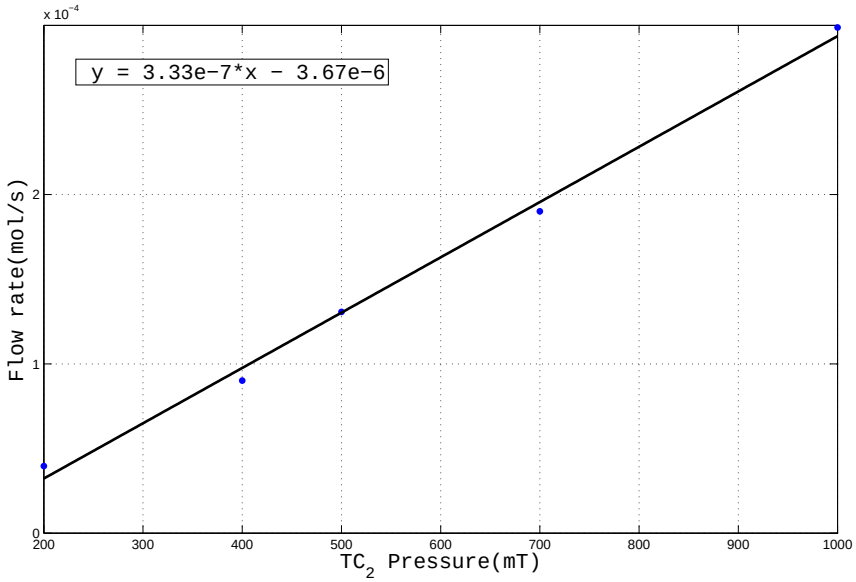

Figure 4.24: ^{3}He molar flow rate as a function of temperature for an Alcatel model 2033H rotary vane pump attached to both the cold plate and ^{3}He circulation lines, with a listed pumping speed of 35 m^3/hr. Pressure is measured near the pump inlet.

occur from introducing 1 K liquid into a mixing chamber at sub–1 K temperatures, returning atoms go through a series of heat exchangers with the outgoing ^{3}He. These heat exchangers cool the returning atoms in steps, using first the still and subsequently, liquid leaving the mixing chamber.

A layout of the dilution refrigerator gas handling system is shown in Figure 4.25. The cold plate is cooled by pumping on a volume of liquid ^{4}He, that is continuously replenished through a capillary of fixed impedance connected to the surrounding helium bath. The cold plate pump, an Alcatel Model 2033H, is also used to evacuate the liquid helium space during initial cooldown. We circulate ^{3}He using an Edwards 9B3 diffusion pump, backed by an Alcatel Model 2033H mechanical pump. The molar flow rate can be determined by correlating the pumping speed with the pressure at the pump inlet, measured using a thermocouple gauge.

The pressure dependent molar flow rates are shown in Figure 4.24 for the Alcatel 2033H mechanical pump. ^{3}He exhausts from this pump and is fed through a liquid nitrogen cooled molecular sieve trap to remove any oil or gaseous impurities before returning to the

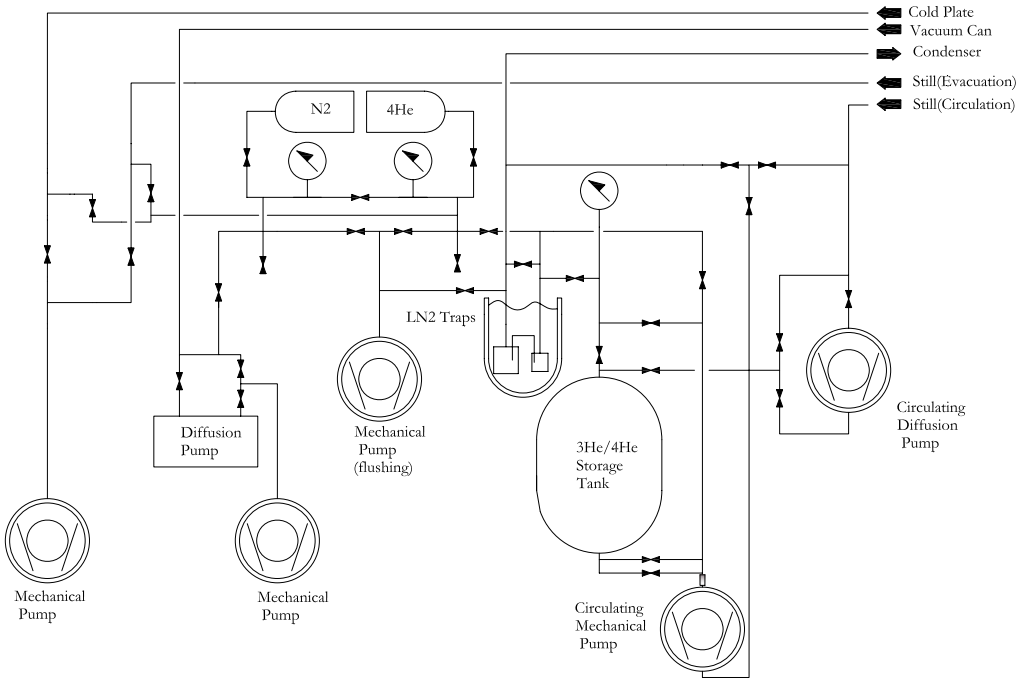

Figure 4.25: Gas handling system for the SHE Model DRI–430 dilution refrigerator. The cold plate and ^{3}He circulating pumps are both Alcatel Model 2033H rotary vane mechanical pumps. A CVC VMF-20 diffusion pump, backed by a Welch mechanical pump, is used to evacuate the inner vacuum chamber. The flushing pump is also a Welch mechanical pump. The system produced a molar flow rate of ~380 μmol/s. Previous experiments, using a 9B3 circulating diffusion pump, backed by an Alcatel model 2063 mechanical pump, had molar flow rates ~600 μmol/s.

refrigerator.

With no external heating, this pump has achieved a cooling power of 1.5 mW at 300 mK, with a molar flow rate of 400 μmol/s. We measured this by first applying a known current to a heater attached to the mixing chamber and measuring the corresponding voltage. The product of these two values gives the applied power. Using the mixing chamber heater causes some fluctuation in temperature. We record the temperature of the mixing chamber once it has stabilized, thereby establishing the refrigerator cooling power at the measured temperature. In previous experiments using the diffusion pump, this refrigerator has been used in continous operation at 10 mK, with a cooling power of 1.48 μW [116]. The cooling power curve for the current setup is shown in Figure 4.26.

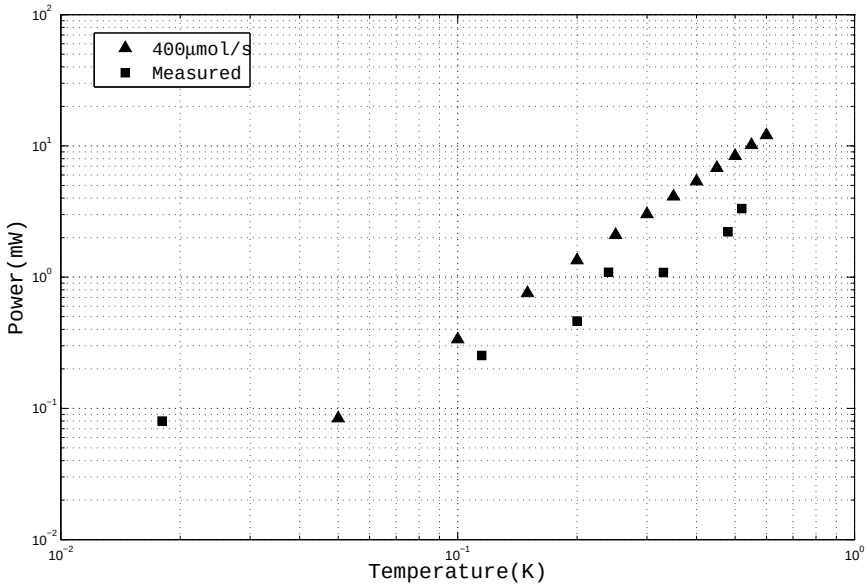

Figure 4.26: Expected and measured cooling power curves for the SHE Model DRI–430 dilution refrigerator. The expected cooling power is calculated using a ^{3}He molar flow rate of 400 μmol/s. The measured molar flow rate was roughly 380 μmol/s.

The gas handling system schematic also shows a set of secondary pumps, used for system preparation and maintenance. These are two Welch mechanical pumps and a CVC VMF-20 diffusion pump. The diffusion pump, backed by a Welch mechanical pump, can be used to evacuate portions of the gas handling system, but primarily serves to evacuate the inner vacuum chamber (IVC) surrounding the dilution refrigerator.

Because the liquid nitrogen traps filter the circulating ^{3}He gas by capturing impurities, from time to time it is necessary to clean the traps. This is done by heating the traps while pumping on them with the second Welch pump. During circulation, it is also important to monitor the pressure before and after the liquid nitrogen traps for indications of blockage. We ran into blockages several times during the early refrigerator runs. Clearing the lines was done in one of two ways. In the case of blockage in the condenser line, we first closed the condenser inlet valve, allowing a warm gas pressure build up, before re-opening the valve, thus flushing the line. For a blockage in the liquid nitrogen trap, the gas is first removed from circulation before heating and pumping out the trap.

Cooling the system proceeds slowly and in stages. This process reduces the likelihood of opening up leaks due to differential thermal contraction, and uses liquid helium efficiently. After pumping out the inner vacuum chamber (IVC), there are two primary areas to check for leaks: from the inner dewar to the IVC and from the IVC to the various refrigerator components. These checks were performed at both room temperature and 77 K using a Leybold L200 leak detector.

Once leak tightness was assured, a typical cooldown proceeded as follows:

- Cool with liquid nitrogen until about 2 - 3 cm of liquid pools in the liquid helium(LHe) fill space.
- Add 1/5 atm H_2 exchange gas to the IVC and monitor the dilution refrigerator temperature.
- When the dilution refrigerator reaches liquid nitrogen temperature, pressurize the LHe fill space to remove liquid nitrogen and pump out the IVC.
- Leak check the refrigerator and IVC.
- Fill the outer dewar liquid nitrogen jacket.

- Begin a fill of the LHe fill space with liquid helium, monitoring temperatures and liquid levels.
- Add 0.1 atm He gas to the IVC and monitor the dilution refrigerator temperature. When the refrigerator is at 4.2 K, pump out the IVC.
- Once the liquid level in the LHe fill space is sufficient for operation, turn on the cold plate pump.
- When the cold plate reaches its normal operating temperature, start to circulate the ^{3}He/^{4}He mixture.

The liquid helium fill was monitored with two 35 cm superconducting level detectors, located midway up the the IVC and approximately 15 cm above the top flange of vacuum can. We typically begin refrigerator operation once the liquid level has reached the top of the second level detector. After this point, the operable refrigerator time depends upon the liquid helium boiloff rate, which is measured by correlating the declining liquid level with the gas outflow rate as measured by a Gilmont airflow gauge. With the measured boiloff rate (see Figure 4.27), we are able to operate several days before transferring more liquid helium.

Once in operation, optimum cooling requires a bakeout of the cold plate, still, and mixing chamber. The cold plate heater is used only during the bakeout procedure, to remove any adsorbed gas. While the still heater is initially used during the bakeout, as mentioned earlier, operation of a dilution refrigerator depends upon maintaining a still temperature of about 0.7 K. A third heater is located on the mixing chamber for the initial bakeout, temperature adjustment and thermometer calibration.

We measured temperature during cooldown and refrigerator operation using a system of resistance thermometers. For the cooldown to 77 K, we use two 1 kΩ platinum resistors, located at the bottom of the LHe fill space, and thermally connected using Apiezon M to the IVC top flange. A third platinum resistor is connected to the dilution refrigerator using Apeizon M. These resistors have a linear temperature response [115], measuring nominally 1.105 kΩ at room temperature and 0.217 kΩ at roughly 77 K (see Figure 4.28). For temperature measurements down to $\sim$ 4.2 K, we have a set of carbon resistors, which are located 1) at the bottom of the LHe space, 2) halfway up the IVC side, 3) on the IVC top flange, 4) 15 cm above the IVC top flange, and 5) 30 cm above the IVC top flange.

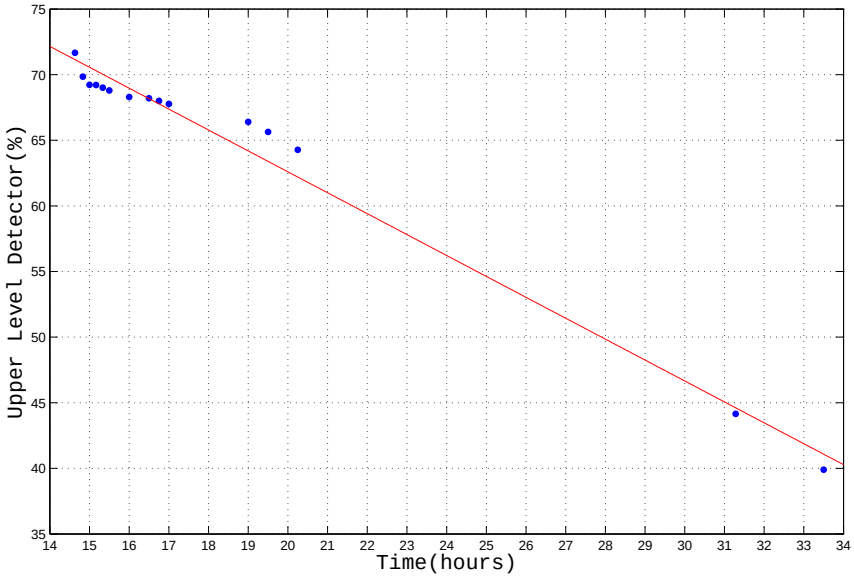

Figure 4.27: Boiloff rate of helium from the liquid helium fill space. The rate is measured independently using a liquid helium level detector mounted in the liquid helium fill space, and a Gilmont gas flow gas, external to the refrigerator.

The most accurate thermometry is required on the dilution refrigerator during operation. We measure the mixing chamber temperature using a Lakeshore GR-200A-30 model 16557 germanium resistance thermometer and a GE RC model 7441 germanium resistance thermometer, read using a SHE Model PCB potentiometric conductance bridge. The manufacturer's calibration curves for the two germanium thermometers are shown in Figure 4.29 and Figure 4.30. We also calibrated two Dale 1 K RuO_2 thermometers, mounted on the mixing chamber, against the model 7441 germanium thermometer. Calibration curves for the two Dale thermometers are shown in Figure 4.31. For a RuO_2 resistor, the data can be fit using

$$R = R_0 \exp\left(\frac{T_0}{T}\right)^{\frac{1}{4}} \tag{4.26}$$

where R_0 and T_0 depend upon composition [80].

The dilution refrigerator also has resistance thermometers mounted on each of its cooling stages. Table 4.5 lists the specifics of these thermometers.

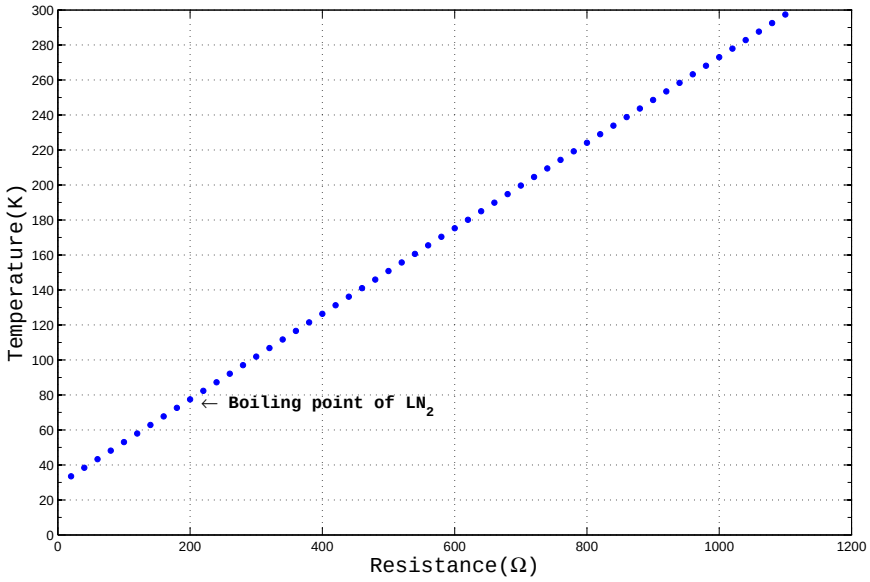

Figure 4.28: Temperature calibration curve for the two platinum resistors used to measure cooling of the dilution refrigerator down to 77 K. At 77 K, the two platinum resistors read 217 Ω.

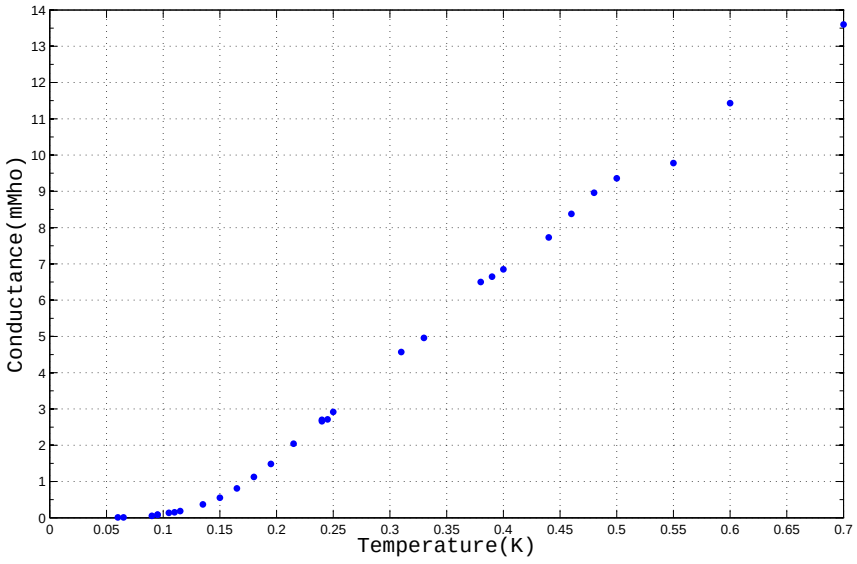

Figure 4.29: Resistance curve for the Lakeshore GR-200A-30 model 16557 thermometer mounted on the mixing chamber

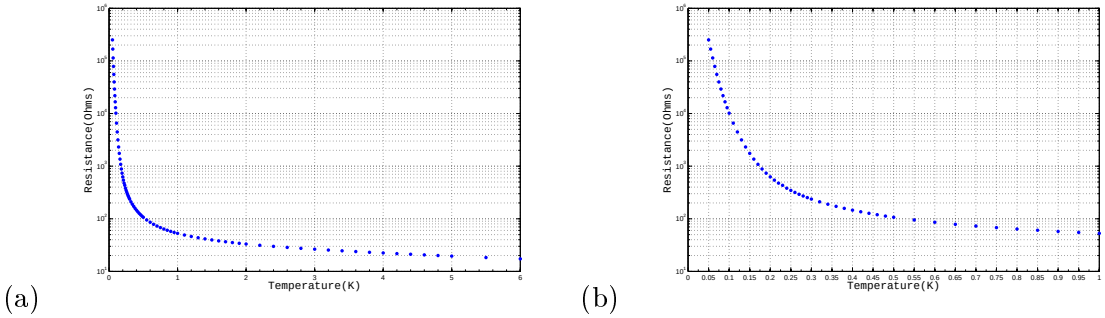

(a) (b)

Figure 4.30: Resistance curve for the GE RC model 7441 thermometer mounted on the mixing chamber a)T $<$ 6 K, b) T $<$ 1 K

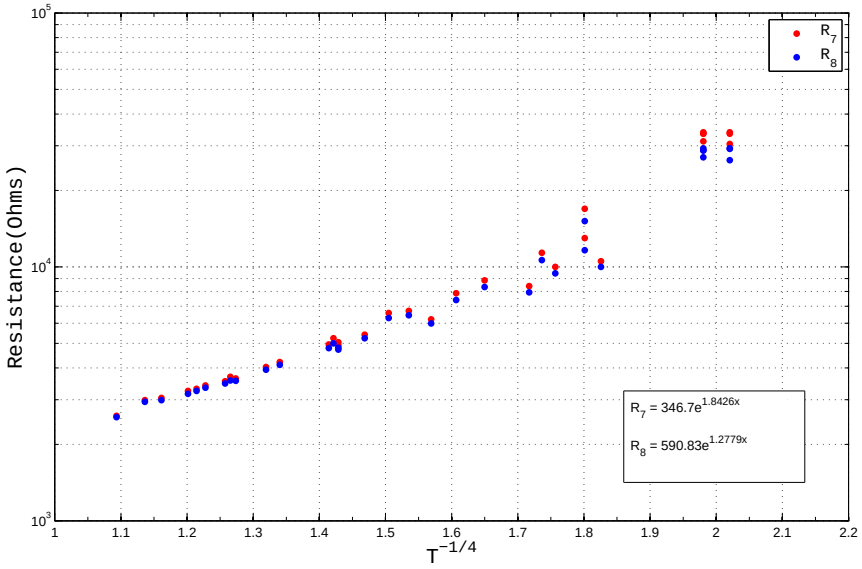

Figure 4.31: Temperature curves for the two Dale resistance thermometers, calibrated against a Lakeshore GR-200A-30 germanium resistance thermometer

Location	Type	300 K value
Cold Plate	Speer 470 Ω	1.879 mmho
Still	Speer 470 Ω	1.840 mmho
Continuous H.E.	Speer 100 Ω	5.375 mmho
Lowest H.E.	Speer 100 Ω	4.874 mmho
Mixing chamber	Speer 100 Ω	4.480 mmho

Table 4.5: Room temperature conductance for each carbon resistance thermometer mounted on the SHE DRI-430 dilution refrigerator.

4.6 Gas Handling System

The gas handling system used to introduce gas into the evaporator volume is shown in Figure 4.6. As an initial control on gas composition, ^{4}He and ^{3}He can be introduced independently or simultaneously. To introduce ^{3}He and ^{4}He separately, the 30 gallon tank is filled to 1 atm with isotopically pure helium. This helium gas has an expected ^{3}He concentration of at least 10^{-12}, and may be as low as 10^{-14}. Two analog gauges, with ranges of 0-100 torr and 0-760 torr respectively, register the tank pressure. To prevent rapid heating of the cold system, gas is introduced through a 0.16 cm O.D. stainless steel line. ^{3}He can be introduced independently from a second volume.

After completing a ^{4}He evaporative purification run or runs, we assess the composition of the remaining liquid by analyzing the composition of the gas that has been removed. The desorbing gas is removed through a 1.27 cm stainless steel line by pumping with a SD451 mechanical pump, while monitoring pressure with a thermocouple gauge. A portion of this gas is siphoned off through a 0.4 cm I.D. stainless steel line, where it enters the gas handling system shown in Figure 4.19 for analysis.

The pressure response of the gas handling system was tested using a ^{3}He calibrated leak, with a leak rate of 8×10^{-9} cc/s. Using this input rate, we were able to measure a partial pressure with the residual gas analyzer within 10 seconds of opening the leak. Gas input at this rate and lower can be reproduced using a leak valve.

The flux to the analysis chamber will be affected by the mechanical pump used to evacuate the evaporator. We will therefore conduct a series of gas flow tests, at room temperature, to determine the optimum leak valve settings for real time gas analysis.

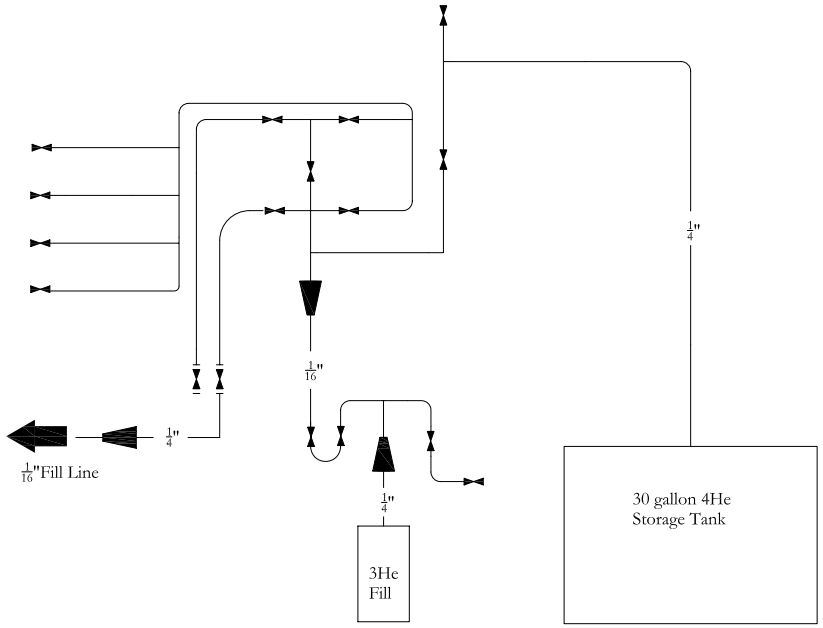

Figure 4.32: Gas handling system for the evaporator fill. The system contains separate inputs for ^{3}He and ^{4}He, allowing mixing of known gas ratios. ^{4}He gas can be stored and introduced from a 30 gallon storage tank. Trace amounts of ^{3}He can be added via a calibrated ^{3}He leak. Gas is introduced to the evaporator buffer volume through a 0.16 cm stainless steel tube.

4.7 Heat Loads

The limited cooling power of a dilution refrigerator demands tight control on any heat production from the evaporator. Conduction and radiation are the primary sources of heat during operation.

To minimize radiative heating from the 300 K outside world, the dilution refrigeration system employs a series of low temperature shields. On the vertical axis, this shield is the liquid nitrogen jacket, which is insulated from 300 K by vacuum, and also contains several layer of superinsulation. The second layer is the liquid helium fill space. In addition to maintaining an IVC temperature of 4.2 K, the evaporating helium cools the three radiation shields, mounted in series, parallel to the IVC top flange. These cooled shields prevent direct line of sight from the room temperature mounting plate down to the liquid surface.

Because the IVC sits in a bath of liquid helium, a portion of the system is always heat sunk at 4.2 K. The top plate of the IVC also provides structural support for the evaporator and its related components (see Figure 4.33). The system is therefore subject to a continual heat load from conduction down the experiment supports. A second source of heating to the refrigerator is radiation from the 4.2 K shield surrounding the experimental apparatus, and the adsorber plate, at either 1.5 K or 4.2 K. Adsorber regeneration raises the temperature of this central heat source to 20 K, as well as introducing gas into the evaporator volume. Each of these loads is addressed separately.

A good estimate of the radiative heating due to the 4.2 K shield can be made by assuming the IVC to be a perfect cylinder of emissivity 0.2 and the brass and copper evaporator body to have an emissivity of 0.06. The radiation from each surface can be defined using the Stefan-Boltzmann expression

$$\dot{Q} = \epsilon \sigma A T^4 F_{1\rightarrow 2} \tag{4.27}$$

where $\dot{Q}$ is the radiated energy, ϵ is the emissivity, $\sigma = 5.67 \times 10^{-8} \mathrm{W/m^2 \cdot K^4}$ is the Stefan-Boltzmann constant, A and T are the area and temperature of the radiating surface, and $F_{1\rightarrow 2}$ is the view factor. For this cylindrical geometry, the view factor is nearly unity [117]. Using these dimensions, the heat load due to radiation at 4 K remains minimal.

For the adsorber plate, most of the radiation impinges on the parallel top and

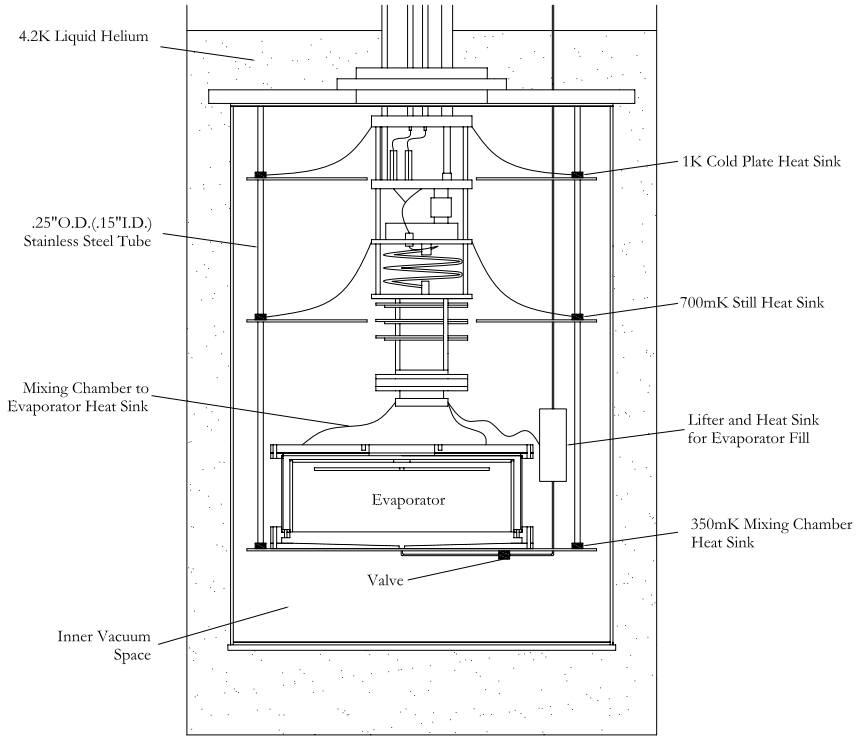

Figure 4.33: Diagram of the evaporator supports. To minimize heating from the evaporator supports, which mount to the 4.2 K IVC, the stainless steel supports are thermally connected to 1.5 K, 0.7 K, and 0.4 K sections of the dilution refrigerator using copper braids. The same is done for the lifter and valve control line (not shown) which also connect thermally to 4.2 K.

bottom surfaces of the evaporator. For two parallel circular plates, the view factor is

$$F_{1\to 2} = \frac{1}{2}\left\{T - \left[T^2 - 4\left(\frac{r_1}{r_2}\right)^2\right]^{\frac{1}{2}}\right\} \tag{4.28}$$

where r_1 and r_2 are the adsorber and evaporator inner diameter respectively and $T = 1 + \frac{1+(r_1/D)^2}{(r_2/D)^2}$, with D the surface separation. The relevant dimensions are 20 cm for the adsorber diameter, 28 cm for the evaporator inner diameter, and 9 cm separating the two. This gives radiation at 4.2 K and 20 K of 2.97×10^{-7} W and 1.85×10^{-4} W respectively. Both of these heat loads are well within the 1.5 mW cooling power limits of the dilution refrigerator at 350 mK.

In order to cool the evaporator vessel to 300 mK, it is necessary to heat sink the successive stages of the evaporator setup at 1.5 K, 700 mK, and 300 mK. These heat sinks are connected to the cold plate, still, and mixing chamber respectively, and are placed along a 0.635 cm O.D. stainless steel tube with a wall thickness of 0.127 cm. The topmost section of this line is connected to the top flange of the IVC, held at 4.2 K by the surrounding liquid helium bath. This bath, as well as each heat sink, produces heating along the stainless steel tube, as well as the heat sink lines, made up of copper braids.

As the system is currently setup, the spacings for the 1.5 K, 700 mK, and 300 mK heat sinks are 8.6 cm, 16.5 cm, and 26.4 cm respectively. This spacing requires copper braid lengths of approximately 16.5 cm, 23.5 cm, and 30.5 cm. Using these lengths, along with the thermal conductivities of copper and stainless steel, and the cross section of each conductor, the heating due to each temperature gradient can be calculated using:

$$Q = \frac{T_i - T_f}{\sum_n R_n} = \frac{T_i - T_1}{R_1} = \frac{T_i - T_2}{R_1 + R_2} = \dots$$

where $R_n = L_n/k_n A_n$. The temperature dependent thermal conductivity for pure copper can be defined as $k = -.069T + 421.429$. The thermal conductivity for commercially pure copper is $k = -.03T + 327.196$[118]. Figure 4.34a, c, and e show the number of copper braids necessary to effectively cool each stage. These values assume ideal thermal contact with both the dilution refrigerator and stainless steel. In this ideal case, a single copper braid is sufficient at each stage of cooling.

To account for less than ideal behavior, each heat sink line is made up of multiple (5) copper braids. Each refrigerator-braid connection is made up of copper braids silver

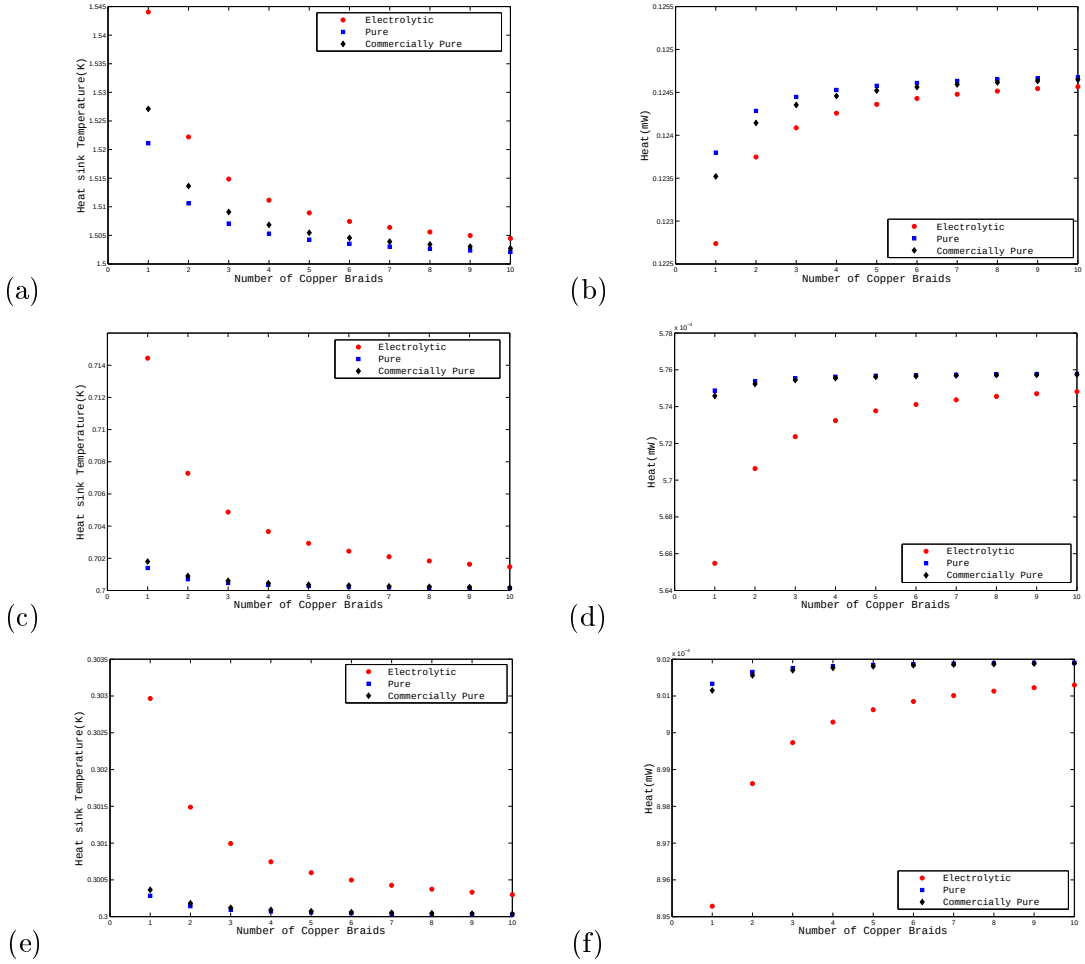

Figure 4.34: Number of copper braids necessary to effectively heat sink the evaporator supports and corresponding heat load to the mixing chamber from the heat sinks at (a,b) 1.5 K, (c,d) 700 mK, and (e,f) 300 mK. A minimum of 5 braids is used at each cooling stage.

soldered to a rectangular copper tab which is then bolted directly to the cold plate, still, or mixing chamber, with Apiezon grease between the tabs and the refrigerator. The other ends of the heat sink leads are soldered directly to the stainless steel tubing using 40 % Sn solder.

Each successive stage of cooling carries a corresponding heat load, which must be carried away by either the mixing chamber, still, or cold plate. Cooling power curves estimate the cooling power of the mixing chamber to be roughly 1 mW at 300 mK. This cooling power is the limiting factor on heat load, since the still and cold plate have significantly higher cooling powers. Given in Figure 4.34b, d, and f are the heat loads from each cooling stage as a function of the number of copper braids.

Because each stage is tethered to three stainless steel lines, the heat values must be multiplied by three to give the expected load.

The heating between the 1.5 K to 700 mK and 700 mK to 300 mK heat sinks was minimal in the current configuration averaging 10^{-2} mW and 10^{-3} mW respectively. The largest heat load is at the 4.2 K–1.5 K transition. Heat from this gradient, in the current configuration, averaged 4 mW. In the worst case, the load to the mixing chamber is estimated to be 100 μW. This is assuming no intermediate heat sinks at 1.5 K and 700 mK. Ideally, with these sinks in place, the total heat load on the mixing chamber should not exceed 0.05 mW. This leaves between 900 μW and 950 μW of cooling power available for the evaporator.

In controlling the superfluid film flow, we incur a heat load from the film burner. To suppress film flow, the rate of evaporation caused by operation of the film burner should equal this molar flow rate. The thermal energy required to desorb a layer of adsorbed gas is proportional to the latent heat of vaporization. From Figure 4.3, the latent heat of vaporization at 400 mK is 68.14 J/mol. Therefore, the heat applied during evaporation operation is approximately 0.7 mW. This is in good agreement with the results of Pratt, who measured a heating of approximately 1 mW to suppress a molar flow rate of 1×10^{-5} mol/s [106].

The bulk of the evaporator setup is located in the purifier volume, which is made up primarily of copper and brass. Cooling of this volume can be modeled as a function of the heat capacities of copper and brass, as well as that of liquid helium. Generally, $Q = C_V \delta T/\delta t$, with Q assumed to be 900 μW.

The heat capacities of copper and brass, written as

$$C = C_{ph} + C_e \tag{4.29}$$

contain both phonon and electron contributions. The phonon contribution can be calculated using the Debye elastic continuum model for solids

$$\frac{C_{ph}}{nN_A k_B} = 9\left(\frac{T}{T_D}\right)^3 \int_0^\infty \frac{x^4 e^x}{(e^x-1)^2} dx$$

where T_D is the Debye temperature [119, 120, 121, 122]. For copper and brass, $T_D = 310$ K and 290 K respectively [123]. In the low temperature limit($T \ll T_D/10$), this expression reduces to

$$C_{ph} = \frac{12}{5}\pi^4 n N_A k_B \left(\frac{T}{T_D}\right)^3 \tag{4.30}$$

where n is the number of atoms in the molecule [124]. From equation 4.30, the phonon contribution to heat capacity at 350 mK is $\sim 3\times10^{-6}$ J/mol·K. At low temperatures, the electron contribution to the heat capacity of metals is linear, defined as

$$C_e = \gamma T \tag{4.31}$$

where $\gamma = 0.691$ mJ/mol·K^2 is the Sommerfeld constant of copper [125, 126]. Because copper is the major component of the evaporator, we use γ_{Cu} to calculate the evaporator heat capacity of .24 J/mol·K at 350 mK. The heat capacity of the evaporator is used to calculate the heat load on the refrigerator during charcoal regeneration.

The evaporator is pumped down to less than 10^{-4} torr before cooldown. Cooling down to sub–1 K temperatures further lowers the pressure to well below the resolution of our pressure gauges. Because there is no convective medium in the evaporator volume, we assume no convective heat exchange between the central adsorber at 4.2 K and the 400 mK walls when the evaporator is empty. The evaporator pressure after adding the ^{3}He-^{4}He solution depends upon the vapor pressures of the two liquids. The ^{3}He and ^{4}He vapor pressures are sufficiently low to give a negligible contribution to convective heating. The activated charcoal should maintain this low pressure condition.

After saturation, it will be necessary to thermally regenerate the charcoal. The planned regeneration temperature is 15 K – 20 K. During the regeneration, the evaporator and surrounding area will be at 350 mK – 600 mK. Because the plate, anchored to the dilution refrigerator mixing chamber, is physically isolated from the evaporator volume, there

should be no heat conducted through any of the surrounding metal due to heating of the plate. Any immediate heating should be a consequence of radiation, again modelled using the Stefan–Boltzmann expression. In the case of activated carbon, we can assume simple blackbody radiation, i.e. $\epsilon \rightarrow 1$. The larger heat load is due to heat convection through the desorbing gas. To minimize this effect, it is necessary to optimize pumping, meaning the rate of removal must be kept higher than the desorption rate. The necessary pumping rate is determined by the desorption kinetics of the charcoal under heating conditions. Upon heating, the gas desorbs very quickly.

As the gas desorbs, it will be removed through a 1.27 cm diameter stainless steel tube, that is approximately 2.75 m in length. If the entire 0.2 mol charcoal capacity was desorbed into the evaporator volume with no evacuation, the resulting pressure would be 5866 Pa. The rate at which this gas can be removed is determined by the conductance of the line, which itself depends on the flow regime, i.e. viscous or molecular. The flow regime is determined by the mean free path

$$\lambda = \frac{1}{\pi n d^2 \sqrt{2}} \tag{4.32}$$

where n is the number of atoms (molecules) per unit length and d is the equivalent hard sphere diameter of the atom (molecule) [127]. For ^{4}He, $d = 0.22$ nm [124].

For a circular tube of radius r, viscous flow is defined by $\lambda/r < 10^{-2}$; $\lambda/r > 1$ defines molecular flow [124]. For the maximum pressure in the evaporator of 5866 Pa, the mean free path is $\sim 10^{-11}$. The conductance can therefore be calculated for molecular flow.

The maximum conductance of a tube is defined by

$$C = 3.81 \times \left(\frac{T}{M}\right)^{\frac{1}{2}} \cdot \frac{D^3}{L} \tag{4.33}$$

which, for ^{4}He at 1 K is 0.4 L/s [128]. At this rate, the entire 0.2 mol of desorbed gas could be removed in a few seconds. In practice, the pumping speed should be considerably slower, due to bends in the gas removal plumbing and the density of the low temperature gas in the 1.27 cm pumping line.

The heat load from conduction by the 15–20 K desorbing gas depends upon the pressure in the evaporator volume. This load is defined by

$$\dot{Q} = 2.1 a_0 P \Delta T \tag{4.34}$$

where a_0 is a function of the ratio of the surface areas, and is roughly 0.09 for the current system. The copper evaporator has a specific heat of 0.24 J/mol·K and an estimated mass of 16.5 kg. The metal would therefore require $\sim$ 60 J to raise the temperature 1 K. Minimization of the heat load due to the desorbing gas to between 10 mW and 100 mW could be attained by keeping the pressure no higher than 0.03 Pa. This assumes total heat transfer from the 20 K helium atoms to the copper volume and no external cooling.

4.8 Discussion

The purification system that we have developed is equipped to remove ^{3}He impurities from superfluid ^{4}He down to a concentration of $x_3 < 10^{-12}$, using differential evaporation. In the process, we expect to stem the flow superfluid film and minimize ^{4}He loss. Eliminating film flow through the use of a film burner will place a small heat load upon the system that is within the limits of the dilution refrigerator cooling power. The extent of heating during charcoal regeneration can be limited by continuous control and monitoring of the desorption rate and evaporator pressure. We have developed a system to assess the effectiveness of differential evaporation as a low temperature purification method by analyzing the ^{3}He and ^{4}He concentrations in the desorbed gas. This system is designed to perform real time analysis during the desorption process. Model predictions indicate that the analysis setup, using residual gas analyzer (RGA), will be able to determine if, and to what degree, the concentration of ^{3}He in the dilute solution has been lowered. Testing of this system, which employs a series of filters for input gas samples, has lowered mass 3 contamination below the resolution of the RGA, and confirmed a ^{3}He/^{4}He resolution of $< 10^{-3}$.

Chapter 5

Summary of Results

This thesis has described the progress of two components of the research and development for the neutron Electric Dipole Moment experiment, to be housed at the Spallation Neutron Source at Oak Ridge National Laboratory. These two components were the development of a method to distinguish neutron capture on ^{3}He from backgrounds and the removal of depolarized ^{3}He from ^{4}He through differential evaporation. The methods and apparatus described herein have direct application in the nEDM experiment.

5.1 Particle Identification

The first component concerned the detection of neutrons through capture on ^{3}He. In an experiment conducted at the Hahn–Meitner Institute, a beam of neutrons was passed through an acrylic cylinder containing a dilute solution of ^{3}He in ^{4}He. The decay products of neutron capture on ^{3}He ionize the ^{4}He atoms, resulting in the production of scintillation light pulses, with nanosecond, microsecond, and second timescales. The pulses, termed singlet and triplet pulses, were detected using photomultiplier tubes and analyzed offline.

The data was taken at temperatures between 90 mK and 1.9 K, and at two ^{3}He/^{4}He concentrations. Backgrounds were determined with the cell containing natural helium. The backgrounds were subtracted from data taken at a ^{3}He/^{4}He concentration of 10^{-5} in order to isolate the neutron capture peak. It was shown that the height of the neutron capture peak scales with beam current. By analyzing the nanosecond timescale events, it was demonstrated that energy of the neutron capture peak is independent of the temperature

of the surrounding ^{4}He.

A comparison was then made relating the energy deposition by ionizing radiation to the intensity of the triplet decay pulses. This data was then used to create contour plots, correlating singlet pulse area with the subsequent number of triplet pulses. It has been shown that the number of triplet pulses following a neutron capture singlet pulse is constant at temperatures below 500 mK. The triplet pulse intensity at temperatures greater than 1500 mK was shown to be roughly 30% higher. For scintillations induced by lighter ions, no temperature dependence was observed. This is consistent with previous experimental results [58]. It has been demonstrated that singlet/triplet pulse decay can be used to distinguish neutron capture from backgrounds at temperatures below 500 mK.

5.2 Evaporative Purification

This thesis also dealt with the development of a prototype apparatus to remove depolarized ^{3}He from ^{4}He during the nEDM run cycle. The development of this apparatus included:

- Mathematical modeling of evaporative purification efficiency, over a range of temperatures
- Refurbishing a dilution refrigerator and determining its feasibility as an apparatus to test differential evaporation
- Design and testing of an apparatus to measure the ^{3}He/^{4}He composition of gas desorbed from the evaporator
- Design and construction of a gas handling system to add and remove gas from the evaporator system

In the time required to lower the ^{3}He concentration in ^{4}He from 10^{-8} to 10^{-10}, the total gas removed will have a ^{3}He/^{4}He concentration of 10^{-2}. This gas will be adsorbed on a charcoal adsorber, and later desorbed for analysis. We have therefore explored two options to analyze the desorbed gas and have concluded that a residual gas analyzer can be used for real time gas analysis. It has been demonstrated that the residual gas analyzer can

be used to resolve a ^{3}He/^{4}He concentration of 10^{-3} needed to characterize the operation of the prototype evaporator.

It has been demonstrated that the existing dilution refrigerator would be suitable for testing of the prototype evaporator. The calculations performed proved a detailed model of the operational parameters of the evaporator, in particular the heat flows and evaporation times.

Bibliography

[1] The nEDM Collaboration. A new search for the neutron electric dipole moment, funding pre-proposal submitted to the department of energy. 2002.

[2] R. Golub and S. K. Lamoreaux. *Phys. Rep.*, 1:237, 1994.

[3] I. B. Khriplovich and S.K. Lamoreaux. *CP Violation without Strangeness.* Springer Verlag, 1997.

[4] C. Burgess and G. Moore. *The Standard Model: A Primer.* Cambridge University Press, 1987.

[5] C.S. Wu, E. Ambler, R.W. Hayward, D.D. Hoppes, and R.P. Hudson. *Phys. Rev.*, 105:1413, 1956.

[6] J. H. Christenson, J. W. Cronin, V. L. Fitch, and R. Turlay. *Phys. Rev. Lett.*, 13:138, 1964.

[7] V. Baluni. *Phys. Rev. D*, 19:2227, 1979.

[8] M. Kobayashi and T. Maskawa. *Prog. Theor. Phys.*, 49:652, 1973.

[9] F. Halzen and A. Martin. *Quarks and Leptons: An Introductory Course in Modern Particle Physics.* John Wiley & Sons, Inc., 1984.

[10] P. Checchia, E. Piotto, and F. Simonetto. *Europhy. Lett.*, 47:656, 1999.

[11] C. G. Callan *et al. Phys. Lett. B*, 63:334, 1976.

[12] Luis Lavoura Gustavo Castelo Branco and Joao Paulo Silva. *CP Violation.* Oxford University Press, 1999.

[13] S. Weinberg. *The Quantum Theory of Fields.* Cambridge University Press, 2000.

[14] J. Schwinger. *Phys. Rev.*, 82:914, 1951.

[15] J. Schwinger. *Phys. Rev.*, 91:713, 1953.

[16] R.J. Crewther et al. *Phys. Rev. Lett.*, 88B:123, 1979.

[17] M. Pospelov and A. Ritz. *Phys. Rev. Lett.*, 83(13):2526, 1999.

[18] The nEDM Collaboration. *Conceptual Design Report for the Neutron Electric Dipole Moment Project (nEDM).* 2007.

[19] S. Weinberg. *Gravitation and Cosmology.* J Wiley & Sons, Inc., 1972.

[20] E. Kolb and M. Turner. *The Early Universe.* Addison- Wesley Publishing Company, 1990.

[21] A. D. Sakharov. *JETP Letters*, 5:24, 1967.

[22] M. E. Shaposhnikov. *Nuc. Phys. B*, 287:757, 1987.

[23] M. B. Gavela et al. *Nuc. Phys. B*, 430:382, 1994.

[24] J.H. Smith, E.M. Purcell, and N.F. Ramsey. *Phys. Rev.*, 108:120, 1957.

[25] N.F. Ramsey. *Physica Scripta*, T22:140, 1988.

[26] T.D. Lee and C.N. Yang. *Phys. Rev.*, 104:254, 1956.

[27] L. Landau. *Nuc. Phy.*, 3:127, 1957.

[28] N.F. Ramsey. *Annual Review of Nuclear and Particle Science*, 32:211, 1982.

[29] W. Dress, P. Miller, J. Pendelbury, P. Perrin, and N. Ramsey. *Phys. Rev. D*, 15:9, 1977.

[30] N.F. Ramsey. *Phys. Rev.*, 78:695, 1950.

[31] N.F. Ramsey. *Rev. Sci. Inst.*, 28:57, 1957.

[32] Y.A.B. Zel'dovich. *Zh. Eksp. Teor*, 36, 1959.

[33] Y.A.B. Zel'dovich. *JETP*, 9:1389, 1959.

[34] F.L. Shapiro. *Usp. Fiz. Nauk.*, 95:145, 1968.

[35] F.L. Shapiro. *Sov. Phys. Usp.*, 11:345, 1968.

[36] *et al.* J. Altarev. *Nuc. Phys.*, A341:269, 1980.

[37] J. Pendlebury, K. Smith, R. Golub, J. Byrne, T. McComb, T. Sumner, M. Burnettand A. Taylor, B. Heckel, N. Ramsey, K. Green, J. Morse, A. Kilvington, C. Baker, and A. Clark. *Physics Letters*, 136B:327, 1984.

[38] A. Steyerl, H. Nagel, F. Schreiber, K. Steinhauser, W. Glaser, P. Ageron, J. Astruc, W. Drexel, R. Gervais, and W. Mampe. *Condensed Matter*, 50:281, 1983.

[39] C.A. Baker, D.D. Doyle, P. Geltenbort, K. Green, M.G.D. van der Grintem, P.G. Harris, P. Iaydjiev, S.N. Ivanov, D.J.R. May, J.M. Pendlebury, J.D. Richardson, D. Shiers, and K.F. Smith. *Phys. Rev. Lett*, 97:131801, 2006.

[40] J.M. Pendlebury, W. Heil, Y. Sobolev, P.G. Harris, J. Richardson, R. Baskin, D. Doyle, P. Geltenbort, K. Green, M. van der Grinten, P. Iaydjiev, S. Ivanov, D. May, and K. Smith. *Physical Review A*, 70, 2004.

[41] R. Golub and S. K. Lamoreaux. *Physical Review A*, 71:237, 2005.

[42] S. Lamoreaux. *Europhysics Letters*, 58:718, 2002.

[43] S. Dzhosyuk, C. Mattoni, D. Mckinsey, A. Thompson, L. Yang, J. Doyle, and P.Huffman. *Nuc. Inst. and Methods B*, 2003.

[44] http://neutrons.ornl.gov/aboutsns/aboutsns.shtml.

[45] R. Golub, D. Richardson, and S.K. Lamoreaux. *Ultra-Cold Neutrons.* IOP Publishing Ltd., Bristol, England, 1991.

[46] R. Golub and J. Pendlebury. *Physics Letters A*, 53:133, 1975.

[47] R.A. Cowley and A.D.B. Woods. *Canadian Journal of Physics*, 49:177, 1971.

[48] H.J. Maris. *Review of Modern Physics*, 49:341, 1977.

[49] P. Ageron, W. Mampe, R. Golub, and J.M. Pendlebury. *Phys. Lett.*, 66A:469, 1978.

[50] R. Golub *et al. Z. Phys.*, B51:187, 1983.

[51] E. Gustsmiedl, R. Golub, and J. Butterworth. *Physica*, B169:503, 1991.

[52] H. Yoshiki *et al. Phys. Rev. Lett.*, 68:1323, 1992.

[53] P.R. Huffman *et al. Nature*, 403:62, 2000.

[54] C.R. Brome *et al. Phys. Rev.*, C63:055502, 2001.

[55] P.C. Hendry and P.V.E. McClintock. *Cryogenics*, 27:131, 1987.

[56] R. Donnelly and C. F. Barenghi. *J.Phys. Chem. Ref. Data*, 27:1217, 1998.

[57] Robert Golub. Internal report: Flush it away. 2008.

[58] E. Aprile, A.Bolotnikov, A. Bolozdynya, and T. Doke. *Noble Gas Detectors.* Wiley-VCH, 2006.

[59] M. Hayden, R. Golub, and S. Lamoreaux. *Proc. LT24, Am. Inst. Phys.*, 147:CP850, 2006.

[60] Als-Nielsen and R. Dietrich. *Phys. Rev*, 133:B925, 1964.

[61] Passel and Schirmer. *Phys. Rev*, 150:146, 1966.

[62] H. A. Roberts and F. L. Hereford. *Phys. Rev. A*, 7:284, 1973.

[63] F. Moss and F. Hereford. *Phys. Rev. Lett.*, 12:415, 1964.

[64] D. Mckinsey, C. Brome, J. Butterworth, S. Dzhosyuk, R. Golub, K. Habicht, P. Huffman, , C. Mattoni, C. Mattoni, L. Yang, and J. Doyle. *Nuc. Inst. and Methods A*, 516:475, 2004.

[65] M. Ovchinnikov, B.L. Grigorenko, K.C. Janda, and V.A. Apkarian. *J. Chem. Phys.*, 108(22):9351, 1998.

[66] J.P. Hernandez and M. Silver. *Physical Review A*, 5(2):372, 1970.

[67] A.V. Benderskii, R. Zadoyan, N. Schwentner, and V.A. Apkarian. *J. Chem. Phys.*, 110(3):1542, 1999.

[68] D. Mckinsey, C. Brome, S. Dzhosyuk, R. Golub, K. Habicht, P. Huffman, E. Korobkina, S. Lamoreaux, C. Mattoni, A. Thompson, L. Yang, and J. Doyle. *Phys. Rev. A*, 67:1, 2003.

[69] F.L. Hereford and F.E. Moss. *Phys. Rev.*, 141:204, 1966.

[70] D.N. McKinsey. *Detection of Magnetically Trapped Neutrons: Liquid Helium as a Scintillator.* Harvard University, PhD Thesis, 2002.

[71] K. Habicht. *Szintillationen in flussigem Helium - ein Detektor Fur ultrakalte Neutronen.* Technischen Universitat Berlin, PhD Thesis, 1998.

[72] M. Stockton, J.W. Keto, and W.A. Fitzsimmons. *Phys. Rev. A*, 5:372, 1972.

[73] J.W. Keto, F.J. Soley, M. Stockton, and W.A. Fitzsimmons. *Phys. Rev. A*, 10:887, 1974.

[74] A. V. Konovalov and G. V. Shlyapnikov. *Soviet Physics JETP*, 73:286, 1991.

[75] C.F. Chabalowski, J.O. Olsen, D.R. Yarkony, and B.H. Lengsfield. *J. Chem. Phys*, 90:2504, 1989.

[76] M. Adib and M. Kilany. *Rad. Phys. and Chem.*, 66:81, 2003.

[77] B. Porter, P. Auchincloss, P. De Barbaro, A. Bodek, and H. Budd. *Am. J. Phys.*, 67(10), 1999.

[78] Q. Ye, D. Dutta, H. Gao, K. Kramer, X. Qian, X. Zong, L. Hannelius, R. D. McKeown, B. Heyburn, S. Singer, R. Golub, and E. Korobkina. *Phys. Rev. A*, 77(053408), 2008.

[79] Q. Ye. *^{3}He Relaxation Time Measurements at Low Temperatures for the Neutron Electric Dipole Moment (nEDM) Experiment.* PhD Thesis, Duke University, 2008.

[80] F. Pobell. *Matter and Methods at Low Temperatures 3^{rd} Ed.* Springer–Verlag Berlin Heidelberg, New York, 2007.

[81] G. Baym and C. Pethick. *Landau Fermi-Liquid Theory.* John Wiley and Sons, Inc., 1991.

[82] V.R. Pandharipande and N. Itoh. *Phys. Rev. A*, 8:2564, 1973.

[83] R. Radebaugh. *National Bureau of Standards Technical Note*, 362, 1967.

[84] A. Anderson, W. Roach, R. Sarwinski, and J. Wheatley. *Phys. Rev. Lett.*, 16:263, 1966.

[85] A. Anderson, D. Edwards, W. Roach, R. Sarwinski, and J.C. Wheatley. *Phys. Rev. Lett.*, 17:367, 1987.

[86] J.C. Wheatley, R.E. Rapp, and R.T. Johnson. *J. Low Temp. Phys.*, 4:1, 1971.

[87] M. Zemansky and R.H. Dittman. *Heat and Thermodynamics.* McGraw-Hill, Inc., 1981.

[88] I. Dana and K.H. Onnes. *Proc. R. Acad. Sci. Amsterdam*, 29:1051, 1926.

[89] R. Berman and J. Poulter. *Philos. Mag.*, 43:1047, 1952.

[90] H. Van Dijk and M. Durieux. *Prog. in Low Temp. Phys.*, 2:431, 1957.

[91] H. Ter Hamsel, H. Van Dijk, and M. Durieux. *Physica*, 36:620, 1967.

[92] D.A. McQuarrie and J.D. Simon. *Physical Chemistry: A Molecular Approach.* University Science Books, 1997.

[93] J. Wheatley, O. Vilches, and W. Abel. *Physics*, 4(1), 1968.

[94] R.H. Salmelin, J. Kyynarainen, M. Berglund, and J. Pekola. *J. Low. Temp. Phys.*, 76(83), 1989.

[95] I. Langmuir. *J. Am. Chem. Soc.*, 38:2221, 1916.

[96] G. Frossati, H. Godfrin, B. Herbal, G. Schumacher, and D. Tholouze. *Proceedings of the ULT Hokane Symposium*, page 205, 1977.

[97] S. Breon, M. Dipirro, D. Glaister, J. Hull, P. Kittel, V. Pecharsky, R. Radebaugh, J. Theilaker, S. Van Sciver, J.I. Weisend, and A. Zeller(editors). *Proceedings of the Cryogenic Engineering Conference*, 47, 1997.

[98] A. Bijl, J. De Boer, and A. Michels. *Physica*, 8:655, 1941.

[99] A.C. Biswas and T.K. Pathria. *J. Low Temp. Phys.*, 28:151, 1977.

[100] E. Ambler and N. Kurti. *Philos. Mag*, 43:260, 1952.

[101] L. Lesensky and H.A. Boorse. *Phys. Rev.*, 87:1135, 1952.

[102] R.K. Waring. *Phys. Rev.*, 99:1704, 1955.

[103] G.R. Herbert, K.L. Chopra, and J.B. Brown. *Phys. Rev.*, 106:391, 1957.

[104] D.B. Crum, D.O. Edwards, and R.E. Sarwinski. *Phys. Rev. A*, 9:1312, 1974.

[105] K. Mendelssohn and G.K. White. *Proc. Phys. Soc. Lond. A*, 63:1328, 1950.

[106] W.P. Pratt. *Rev. Sci. Inst.*, 46:1587, 1975.

[107] K.S.W. Sing. *Proceedings of the International Symposium on Surface Area Determination*, page 25, 1970.

[108] D.F. Brewer, A. Evenson, and A.L. Thomson. *J. Low. Temp. Phys.*, 3:603, 1970.

[109] I. Ozdemir and D. Perinic. *J. Vac. Sci. Tech*, 16:2524, 1998.

[110] E. Hoffman and V. Stroobant. *Mass Spectrometry Principles and Applications 3rd Ed.* Wiley, 2007.

[111] P. Danielson. *Desorbing Water in a Vacuum System.*

[112] Y.Sano, H. Wakita, K. Wakino, M. Murata, H. Yamamoto, and H. Matsuda. *International Journal of Mass Spectrometry and Ion Processes*, 91(1):69, 1989.

[113] S. Burton and D. Cornelius. *US Bureau of Mines Report*, 1989.

[114] http://cryogenics.nist.gov/mpropsmay/material%20properties.htm.

[115] G.K. White. *Experimental Techniques in Low Temperature Physics, 3^{rd} Ed.* Clarendon Press, Oxford, 1979.

[116] Chris Keith. *Dissertation: Total Cross Section Measurements for the Scattering of Polarized Neutrons from Polarized ^{3}He.* 1994.

[117] F. Incropera, D. DeWitt, T. Bergman, and A. Lavine. *Fundamentals of Heat and Mass Transfer 6^{th} Ed.* Wiley, 2006.

[118] R.W. Powell, C.Y. Ho, and P.E. Liley. *National Bureau of Standards*, 8, 1966.

[119] N.W. Ashcroft and N.D. Mermin. *Solid State Physics.* Holt Rinehart and Winston, New York, 1976.

[120] T.H.K. Barron and G.K. White. *Heat Capacity and Thermal Expansion at Low Temperatures.* Plenum Press, New York, 1999.

[121] E.S.R. Gopal. *Specific Heats at Low Temperatures.* Plenum Press, New York, 1966.

[122] J.M. Ziman. *Electrons and Phonons.* Clarendon Press, Oxford, 1972.

[123] D.R. Chipman. *J. App. Phys.*, 31(11):2012, 1960.

[124] G. Ventura and L. Risegari. *The Art of Cryogenics: Low Temperature Experimental Techniques.* Elsevier Publications, Oxford, 2008.

[125] J. Bevk. *Philos. Mag.*, 28:1379, 1973.

[126] D.S. Greywall. *Phys. Rev. B*, 18:2127, 1978.

[127] E.H. Kennard. *Kinetic Theory of Gases.* McGraw Hill, New York, 1938.

[128] S. Dushman. *Scientific Foundations of Vacuum Techniques.* Wiley, New York, 1962.